THE UNIVERSITY OF CHICAGO

DECIPHERING GALACTIC CHEMICAL EVOLUTION: IRON AND NICKEL ISOTOPES AND COSMIC RAY EXPOSURE AGES OF PRESOLAR SILICON CARBIDE GRAINS

A DISSERTATION SUBMITTED TO
THE FACULTY OF THE DIVISION OF THE PHYSICAL SCIENCES
IN CANDIDACY FOR THE DEGREE OF
DOCTOR OF PHILOSOPHY

DEPARTMENT OF THE GEOPHYSICAL SCIENCES

BY
RETO GEORG TRAPPITSCH

CHICAGO, ILLINOIS
AUGUST 2016

To my parents for always supporting me and my crazy ideas.

Here goes nothing...

TABLE OF CONTENTS

LIST OF FIGURES

LIST OF TABLES

ACKNOWLEDGMENTS

I would like to thank my advisor Andy Davis, who always let me choose my own path and gave me the freedom to work on many different projects. At the same time, he always supported me with very interesting discussions and helped me develop new ideas. Thank you to Mike Savina, who taught me how to use CHARISMA at Argonne National Lab, gave me the freedom to run my own experiments, and helped me fix things that I broke on the way of doing so. We spent many days in the lab, often until very late, and slowly but surely, I learned how to build lasers and run the instrument by myself. Also a big thank you to Thomas Stephan. He built CHILI and gave me a lot of freedom and possibilities to help building the instrument and to influence the design. While doing so, he taught me about various aspects of CHILI itself and about mass spectrometry in general. I would also like to thank the rest of my committee for many fruitful discussions. These members are Nicolas Dauphas, Mike Pellin, and Frank Richter.

Thanks to the whole CHILI group in all variations over the years: Manavi Jadhav, Chris Kelly, Ashley King, Levke Kööp, Nan Liu, and Krysten Villalon. A special thanks goes to Det Rost, with whom I spent a lot of time in the lab, but also outside the lab at various concerts and dinners.

I would like to also thank my collaborators, especially my former advisor at the University of Bern, Ingo Leya, with whom I continued working throughout my time in Chicago. Thanks also to Fred Ciesla for our collaboration, for always having an open ear, and for still inviting me to his group's coffee hour. In addition I would like to thank Dave Willingham for helping me with experiments on CHARISMA, Christoph Burkhardt, Nicolas Greber, and François Tissot for various interesting discussions, and Marco Pignatari and Falk Herwig from the NuGrid collaboration for supporting my endeavors into stellar evolution and nucleosynthesis. Also a big thank you to the administrative staff, especially Brian Lynch, James Eason, David Taylor, Katie Kaftanich, and Barb Hall.

I would like to thank all the DoGS students and friends I met over the years, especially

Steward Edie, Aric Mine, and Michael Kang, the latter also being my long term roommate. The three of us did many trips and bike rides together, which was always very relaxing and helped me getting my mind off science for a bit. Finally, I would like to thank my family, especially my parents Karl and Yvonne Trappitsch for always supporting me, no matter what, as well as Guillermina Ramírez San-Juan.

This work was supported by a NASA Earth and Planetary Science Fellowship through NASA headquarters (grant number NNX12AL85H).

ABSTRACT

The universe we live in originated in the Big Bang, which also produced the most abundant elements that are around today, namely hydrogen and helium. However, looking around on Earth today, many more elements exist around and inside of us. For example, humans are a carbon-based life form surviving by breathing nitrogen and oxygen and eating complex molecules. Elements heavier than lithium were not formed in the Big Bang. Most of them were synthesized in evolved stars, except for lithium, beryllium and boron, which were mostly formed by spallation reactions of cosmic rays with interstellar matter. This means that the composition that we find in the Solar System today represents the galactic chemical evolution of the elements and isotopes as it was 4.567 billion years ago. This composition can be studied by analyzing meteorites, which are rocks from space that regularly fall to Earth. Some of these meteorites have not significantly been altered throughout the history of the Solar System and therefore preserved a record of the original composition of the Solar System. In addition, these meteorites contain tiny, micrometer-sized, dust grains that did not form in the Solar System itself. These dust grains – presolar grains – formed in the outflow of dying stars, therefore allowing us to study how a specific star forms elements.

In this work we are looking at two aspects of presolar grain research. We first describe the newly built Chicago Instrument for Laser Ionization (CHILI) and compare it to the previous generation instruments at Argonne National Laboratory. We used CHILI to study the iron and nickel isotopic composition of presolar silicon carbide grains. While the neutron-rich isotopes ^{58}Fe and ^{64}Ni are mostly influenced by the parent star from which the grains formed, the neutron-poor isotopes are minimally altered and represent the composition of what went into the star in the first place. Therefore, iron and nickel isotopes are valuable in tracing nucleosynthesis in the parent star as well as to study galactic chemical evolution. Our study finds a good agreement with stellar models in terms of isotope anomalies in the neutron-rich isotopes and a good agreement with galactic chemical evolution models in the neutron-poor isotopes. It however remains a puzzle, how and why the galactic chemical

evolution dominated isotopes in presolar silicon carbide grains show such a broad variety in isotopic composition compared to the Solar System.

The second part of this work focuses on the age of presolar silicon carbide grains. While these grains were transported through the interstellar medium, they were irradiated with galactic cosmic rays that induced nuclear reactions and yielded the production of so-called cosmogenic nuclides. These nuclides can be used in order to determine the time a presolar grain was exposed to the galactic cosmic ray flux. Here, we present a new model for cosmogenic production rates and discuss in detail the uncertainties that go into the model. We find that ^{21}Ne is the most reliable cosmogenic nuclide to determine a cosmic ray exposure age of a presolar silicon carbide grain. Most presolar silicon carbide grains have ages between 10 and 200 Ma, with a clear peak in the distribution at around 20 Ma.

Our new iron and nickel isotopic measurements give tighter constraints on current galactic chemical evolution models. These measurements represent some of the first analyses with the Chicago Instrument for Laser Ionization. With this instrument, many more interesting galactic chemical evolution-dominated elements will be measured in the future, e.g., chromium and titanium, since these elements have only minimal contributions from the grain's parent star. In addition, correlated cosmogenic helium, lithium, and neon studies of individual presolar silicon carbide grains are currently in progress. Such studies will help to better understand current limitations of the cosmic-ray-induced production rates and recoil loss models.

CHAPTER 1

INTRODUCTION

Presolar grains, recovered from meteorites, are mineral condensates that formed in the outflow of dying stars. After the condensation of a grain, it travelled through the interstellar medium, where it was irradiated with galactic cosmic rays (GCRs) prior to incorporation into a meteorite parent body in the early Solar System. Some meteorite parent bodies were never heavily processed throughout the history of the Solar System and have thus preserved presolar grains. Thus they represent a unique opportunity to study stellar nucleosynthesis as well as galactic chemical evolution (GCE) in the laboratory. For recent reviews see Davis (2011) and Zinner (2014).

Various types of presolar grains are known, the ones best studied are silicon carbide (SiC) grains. These grains are resistant to dissolution of silicates and organics with harsh acids and can therefore be easily recovered. Furthermore they occur in sizes up to tens of micrometers and tend to contain high abundances of trace elements, allowing the study of a large variety of isotopic systems (Amari et al., 1995). Silicon carbide grains can be further divided into several groups based on their nitrogen, carbon, and silicon isotopic composition (Zinner, 2014). Each group is indicative of the type of parent star the grains came from. While mainstream, Y, and Z grains condensed in the vicinity of asymptotic giant branch (AGB) stars, X and C grains originated in type II supernovae (SNe). The origin of AB grains is ambiguous, and several possibilities including novae were discussed in the literature (e.g., Amari et al., 2001a,c).

1.1 Presolar Grains as Proxies for Galactic Chemical Evolution

After the Big Bang, the universe contained mainly hydrogen and helium. Heavier elements were subsequently formed in stars and returned to the interstellar medium when those stars exploded or through stellar winds. Mainly because of their shorter lifetimes, massive stars

have a higher contribution to enriching the interstellar medium with heavy elements in the early universe than less massive stars. Therefore, type II SNe dominated the GCE early on. Type Ia SNe on the other hand are thought to result from thermonuclear explosions in a binary system, where a white dwarf star accreted matter from a companion star until it exceeded the Chandrasekhar mass. This requires a full stellar evolution of one star with a mass smaller than $9\,M_{\odot}$ to become a white dwarf. Heavier stars will result in a type II SNe and not produce a white dwarf (see, e.g., Herwig, 2013). Type Ia SNe therefore could not have contributed to the interstellar medium right after the Big Bang. The formation of a white dwarf, using the upper mass limit of the initial star, requires at least 40 Ma. The same is true for AGB stars – their low mass results in a longer lifetime and hence in a later return of synthesized material compared to massive stars. For example, a $2\,M_{\odot}$ star lives for $\sim$2 Ga, hence, cannot contribute to GCE for this time. A recent review on GCE can be found by Nomoto et al. (2013).

Presolar grains that originated in AGB stars carry their parent star's isotopic signatures, especially in *s*-process isotopes. Most of the variation in these isotopic patterns can be attributed to different masses, different metallicities, and different mean neutron exposures in their parent AGB stars. However, certain elements like silicon and titanium in presolar grains vary more in isotopic composition than expected from AGB stellar models (e.g., Nittler, 2005). The larger isotopic variation in grains is attributed to GCE (e.g., Alexander and Nittler, 1999). Models of *s*-process nucleosynthesis in AGB stars (e.g., Gallino et al., 1998; Cristallo et al., 2011) predict that most of the iron and nickel isotopes (except for ^{58}Fe and ^{64}Ni) are little affected by AGB star nucleosynthesis, similar to silicon and titanium isotopes, making them suitable proxies to study GCE. Furthermore, iron and nickel are abundant enough in presolar SiC grains that their isotopic composition can be analyzed in individual grains with current instruments.

Previous measurements of iron and nickel isotopes in presolar SiC grains were done by Marhas et al. (2008) using a CAMECA NanoSIMS 50. Abundances for ^{58}Fe could not be

measured and the abundance of ^{58}Ni was corrected for interference with ^{58}Fe by assuming a solar ^{58}Fe/^{56}Fe ratio. Furthermore, NanoSIMS measurements of ^{54}Fe had to be corrected for interferences with ^{54}Cr assuming a solar ^{54}Cr/^{52}Cr ratio. Marhas et al. (2008) did not report data for ^{64}Ni due to interferences with ^{64}Zn. However, ^{58}Fe and ^{64}Ni are the isotopes that are predicted by AGB models to be most strongly enhanced by the *s*-process nucleosynthesis. Understanding the AGB stellar contribution is essential in deciphering the GCE record and therefore requires a technique that avoids contributions from isobars.

CHILI, the Chicago Instrument for Laser Ionization (Stephan et al., 2016), allows us to measure all iron and nickel isotopes simultaneously. This opens the possibility to study the neutron-rich isotopes for their *s*-process contribution and also to study the neutron-poor isotopes as proxies for GCE. In a preliminary study, we measured 13 grains for their iron isotopic composition using CHARISMA at Argonne National Laboratory. These grains were subsequently classified via silicon and carbon isotopic measurements on the CAMECA NanoSIMS 50 at Washington University in St. Louis. During this measurement session, we also analyzed and classified many more presolar SiC grains. Using CHILI, we then analyzed 74 of these presolar SiC grains for their iron and nickel isotopic composition. Such a multi-element study allows us not only to compare our measurements with model predictions for GCE, but also to test the hypothesis that various GCE dominated isotopes in individual presolar grains should show correlated effects.

1.2 Cosmic Ray Exposure Ages of Presolar SiC Grains

Cosmogenic nuclides have long been used to determine the time of exposure of meteorites to GCRs. These nuclides were first discovered by Bauer (1947) who suggested that unreasonably high apparent uranium-helium ages of iron meteorites could be explained by cosmic ray production of ^{4}He. The influence of GCRs on helium isotopes was soon after confirmed by Paneth et al. (1952) and Paneth (1952). Since then, cosmogenic nuclides have become a useful tool to determine the time meteoroids have been exposed to GCRs, which is usually

the time between the meteoroid parent body break-up event and the fall of a meteorite to Earth. Since GCR penetration in meteoritic material is of the order of meters, meteoroids usually have no pre-exposure record from before the break-up event. A review on cosmogenic nuclides was given, e.g., by Wieler (2002).

During the travel from the parent star to the solar nebula, presolar grains were also exposed to GCRs. Galactic cosmic rays mainly consist of high energetic protons and ^{4}He nuclei (α particles). If these particles have enough energy (usually $> 5\,\mathrm{MeV}$), they can induce spallation reactions. For example, a high energetic proton can break up a ^{28}Si nucleus and form ^{21}Ne via the reaction $^{28}\mathrm{Si}(p, X)^{21}\mathrm{Ne}$. Cosmogenic nuclides like ^{21}Ne can be used to determine the time the presolar grain has been exposed to GCRs, i.e., the time the grain was traveling through the interstellar medium prior to incorporation into the early Solar System. To determine the cosmic ray exposure (CRE) age, the production rates of cosmogenic nuclides have to be known. Unfortunately, modeling cosmogenic nuclides in presolar grains contains more uncertainties than modeling these production rates in meteorites. First of all, the GCR spectrum that irradiated presolar grains in the interstellar medium prior to Solar System formation is largely unknown. Today's GCR spectrum in the Solar System itself is modulated by the magnetic field of the Sun, i.e., charged particles with low energies cannot enter the Solar System and are repulsed by the solar magnetic field. In the ISM, however, no magnetic fields are present and therefore, the GCR spectrum looks different. Thanks to the Voyager spacecraft, which crossed the magnetic boundary surrounding the Solar System, today's GCR spectrum in the ISM as well as its composition is well known and understood (Stone et al., 2013). One more parameter needed to determine a true CRE age, however, is the total GCR flux approximately 5 Ga ago. Galactic cosmic ray acceleration in the interstellar medium takes place mostly by shockwaves that are triggered by SNe explosions (Bell, 1978). The number of these shock waves should therefore be correlated to the star formation rate in the solar neighborhood. This star formation rate is somewhat constrained by the initial mass function. Assuming a Kroupa initial mass function (Kroupa, 2008), Kobayashi et al. (2011)

showed that the star formation rate 5 Ga ago was very similar to the star formation rate today. Hence, the assumption that the GCR flux that presolar grains were irradiated with is similar to the current GCR flux in the interstellar medium has some validity. Note that a shift in the total particle flux shifts the ages of the presolar grains linearly. Another difficulty in calculating cosmogenic production rates in presolar grains compared to meteoroids is the size of the grains. The largest presolar SiC grains are usually tens of μm in diameter. The product of a spallation reaction, i.e., the produced cosmogenic nuclide, will have some momentum transferred to it since the total momentum of the reaction has to be conserved. Due to this momentum, the cosmogenic nuclide will travel a short distance. Such distances are, for the nuclides of interest, of the order of a few μm, thus every produced cosmogenic nuclide has a chance to leave the presolar grain. To determine the age of a presolar grain, the measured cosmogenic inventory has to be corrected for this recoil loss depending on the size of the presolar grain. In general, heavier cosmogenic nuclides have shorter stopping distances and are therefore more likely to be retained in a presolar grain. Finally, presolar SiC grains have a rather atypical composition compared to regular meteoritic material. The only two reasonably available target elements for spallation reactions in these grains are silicon and carbon. The products that we are mostly interested here are helium, lithium, and neon isotopes, since these cosmogenic nuclides have been measured. While cross sections for the neon isotope productions from silicon are readily available, for ^{3}He and especially lithium, only few measurements of the nuclear cross sections of interest exist.

In this work, we calculate new production rates for ^{3}He, ^{6,7}Li, and ^{21,22}Ne as well as present a new model to correct presolar grain ages for recoil losses. The new production rates are mostly based on the experimental cross section database described by Ammon et al. (2009), Leya and Masarik (2009), and Trappitsch and Leya (2013). However, certain cross sections needed to be calculated. While nuclear codes such as TALYS-1.2 (Koning et al., 2008) are useful for calculating cross sections relative to one another (Meier et al., 2014), absolute calculations are more difficult. Absolute calculations were, whenever possible, scaled

to experimental data points. The recoil model presented here is an extension of the model we previously used for calculating recoil losses in interplanetary dust particles (Trappitsch and Leya, 2013) and is purely based on nuclear reaction modeling using the TALYS-1.2 code (Koning et al., 2008) as well as the INCL/ABLA4.5/ABLA07 code (Boudard et al., 2002). Here, the nuclear codes are well suited, since all recoil calculations only require relative cross sections.

CHAPTER 2

EXPERIMENTAL METHODS

Analyzing presolar grains for isotopic compositions of their constituent elements allows the study of stellar nucleosynthesis and GCE. However, the small size of the grains makes such measurements difficult, especially for trace elements. Since presolar grains were discovered (Lewis et al., 1987), many instrumental improvements have allowed isotopic analysis of elements present at lower and lower concentrations in smaller and smaller samples. Notable instruments aside from resonance ionization mass spectrometry (RIMS) instruments are secondary ion mass spectrometers, particularly the CAMECA ims-3f, 4f, 5f, 6f, and 7f and the Cameca NanoSIMS 50 and 50L (Stadermann et al., 1999; Hoppe et al., 2013). For this work, we used the Chicago Argonne Resonance Ionization Spectrometer for MicroAnalysis (CHARISMA) at Argonne National Laboratory as well as the Chicago Instrument for Laser Ionization (CHILI) at the University of Chicago to analyze presolar grains.

2.1 Resonance Ionization Mass Spectrometry

The usage of RIMS instruments for the analysis of presolar grains started with the CHARSIMA instrument at Argonne National Laboratory (Ma et al., 1995; Savina et al., 2003b). Subsequent work showed the capabilities of RIMS in analyzing presolar grains for their trace element isotopic composition (Nicolussi et al., 1997a,b, 1998a,b,c; Davis et al., 1999; Pellin et al., 1999, 2000, 2006; Savina et al., 2003a; Barzyk et al., 2006, 2007; Liu et al., 2014, 2015). Building on CHARISMA's success, CHILI was planned, funded, and built at the University of Chicago, based on the same principles as CHARISMA. This work here shows some of the very first measurements performed with CHILI.

Figure 2.1 shows a schematic of the inner workings of a RIMS instrument. Sample material is removed from the surface using a UV desorption laser or an ion gun. Both methods remove only the top layer of material. A small fraction of the desorbed or sputtered

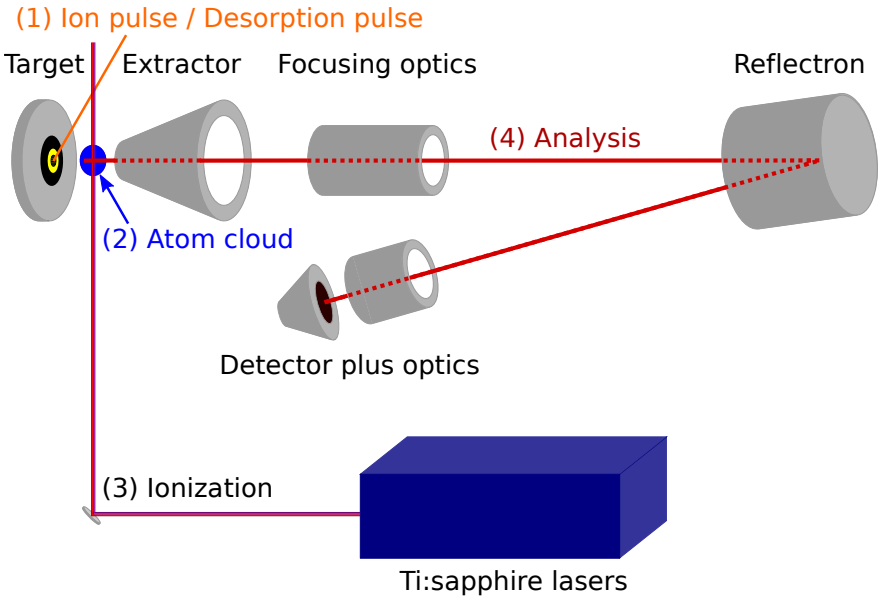

Figure 2.1 Schematic of RIMS. An ion gun or desorption laser pulse (1) creates a cloud of neutral atoms and secondary ions (2) above the sample. Secondary ions are ejected from the system prior to resonance ionization of the neutrals using lasers (3). These photoions are then analyzed in the time-of-flight mass spectrometer and detected (4).

particles are ions. They can be ejected in two ways: by pulsing the extractor voltage such that the ions fly through the reflectron and get neutralized by hitting the back of the reflectron, i.e., giving them an energy such that they do not turn around and reach the detector, or by pushing them back into the target where they get subsequently neutralized. The remaining neutral particles are then ionized resonantly, using tunable Ti:sapphire lasers, and eventually extracted and accelerated into the time-of-flight mass spectrometer. The arrival times of the ions are detected using a microchannel plate detector with a single anode.

Compared to secondary ion mass spectrometry (SIMS), RIMS has the advantage of a high useful yield, which is the number of atoms of interest detected divided by the total number of those atoms removed from the sample surface. After sputtering or desorbing atoms from the sample surface, the vast majority of secondary particles are neutral. By ionizing these neutrals resonantly using lasers, the vast majority of the removed sample atoms can be analyzed. To ionize all the neutral particles, the ionization laser must have enough power to saturate the transition as well as illuminate the whole cloud of neutral

atoms. In addition, the neutrals must be in the electronic state that the ionization lasers are tuned for, which is usually the ground state. The mass separation in the carefully designed time-of-flight mass spectrometer further allows for >90% transmission (Stephan et al., 2016). The beam shaping elements are electrostatic fields and lenses, hence, almost all photoions reach the detector. Resonance ionization is orders of magnitude more efficient than nonresonant multiphoton ionization. An additional advantage of RIMS is the high elemental selectivity. Other elements in the cloud of neutral particles are largely transparent to the laser light and hence hardly ionize at all (Hurst et al., 1979). One major problem in SIMS is that ionization efficiency is strongly dependent on the sample matrix and on the chemical reactivity of the incident ions. Photoionization of the majority of the removed sample atoms in RIMS is much less dependent on the sample matrix (Pellin et al., 1984). Specific details on the ionization scheme for iron and nickel isotopes and the characteristics of these schemes are given below in Section 2.2.

2.1.1 Sample removal – desorption laser

To remove material from presolar grains for subsequent analysis, we use a frequency-tripled Nd:YLF desorption laser with 351 nm wavelength from Photonics Industries (model DC150-351) with a maximum output power of 1.5 W. The desorption laser is run in pulsed mode with a repetition rate of 1 kHz. The desorption laser beam is brought into the instrument through a window and then focused onto the sample via a built-in Schwarzschild optical microscope. This allows focussing the beam to a diameter of roughly 1 μm on the sample.

To determine the spot-size of CHILI's desorption laser, we slowly desorbed material from a polished stainless steel disk for several hours creating a measurable crater. In addition, we counted all nickel ions during the experiment in order to determine a useful yield of the instrument (see Section 2.1.5). After the ion measurement, the crater was then imaged in a scanning electron microscope under various angles. From a pair of stereo images, we determined the crater volume using the MeX software from Alicona. Figure 2.2 shows a

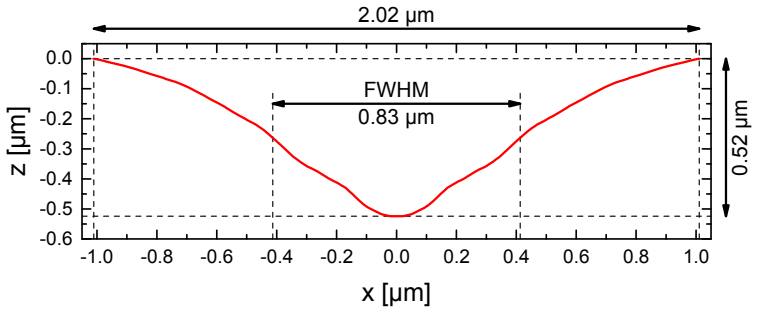

Figure 2.2 Crater produced in stainless steel by slowly desorbing material from the surface using the laser.

profile of the reconstructed crater. The crater has a full-width at half-maximum (FWHM) of 0.83 μm, is 0.52 μm deep, and has a base diameter of 2.02 μm. The crater profile is not perfectly Gaussian. The crater profile is not a direct representation of the incoming laser beam profile, since the actual shape of the crater is the result of a combination of beam profile and desorption properties of the material we are desorbing from. In addition, the desorption laser beam is susceptible to vibration as well as air flow through the laboratory, increasing the size of the crater.

2.1.2 Ionization – Ti:sapphire laser design

The design of the tunable Ti:sapphire lasers is based on a design by Photonics Industries that was subsequently adopted and optimized by Savina et al. (2003b). Figure 2.3 shows a color coded schematic of one individual laser cavity.

Pump beam: The pump beam, shown in green, is a second harmonic Nd:YLF laser beam with 527 nm wavelength run at a repetition rate of 1 kHz. For the CHARISMA instrument, one Photonics Industries 60 W YLF laser (model DM-60) is used to pump three individual laser cavities. CHILI uses in total three Photonics 40 W YLF lasers (model DM-40), each of which pumps two Ti:sapphire cavities. At the current specifications, the pump lasers produce a pulse with a length of approximately 190 ns (FWHM) at a repetition rate of

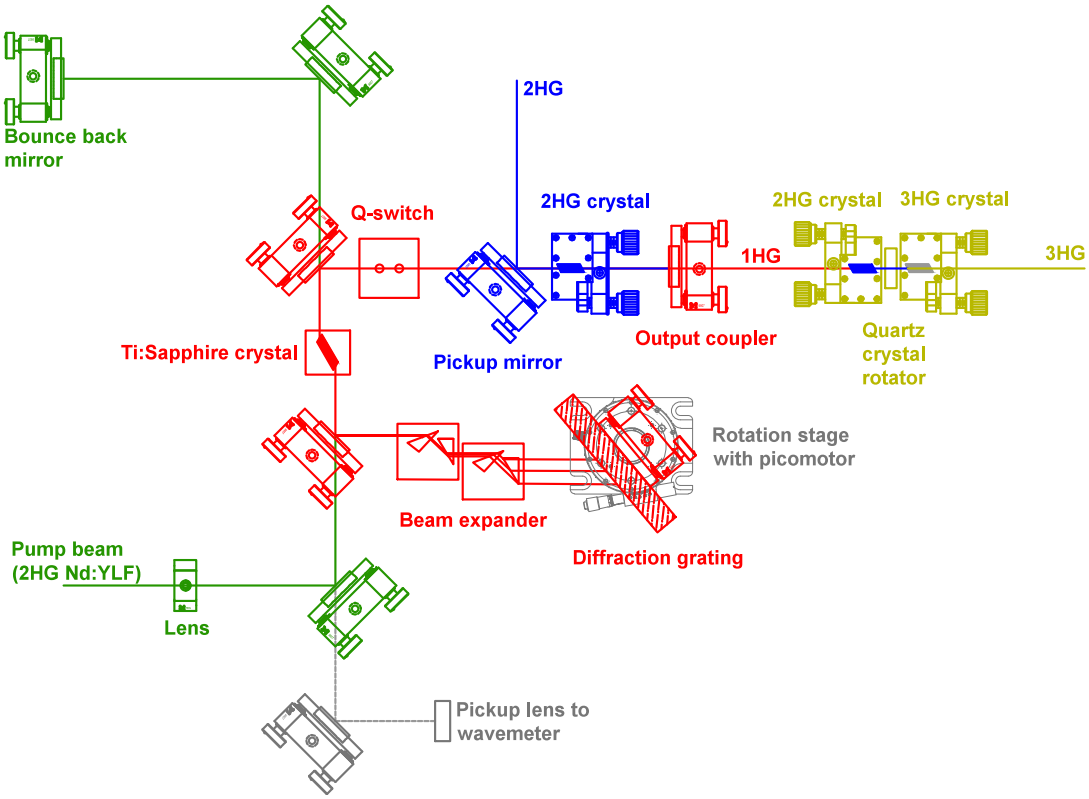

Figure 2.3 Schematic of a tunable Ti:sapphire laser cavity. The pump beam is shown in green. Red components and lines show the parts responsible for the fundamental beam. The second harmonic generation (2HG) setup is inserted into the schematic in blue and the third harmonic generation (3HG) setup in yellow. Gray components depict the active feedback control for keeping the laser wavelength stable.

1 kHz. Each pump laser beam is split up into two branches by using half-wave plates and a polarizing cube. First the pump beam goes through a half-wave plate, giving the beam a mixed s- and p-polarization. The polarizing cube then lets the p-polarized beam pass straight through while the s-polarized part is reflected and exits the beam cube orthogonally to the input beam. The p-polarized beam can be focused directly onto a Ti:sapphire crystal and pump it. The s-polarized beam has to be rotated to p-polarization before pumping another Ti:sapphire crystal, since our cavities are built for p-polarized laser light. Using a lens, the pump beam for each cavity is focused into the Ti:sapphire crystal, for which the

ends are cut at Brewster's angle allowing for minimum loss due to reflection.

The laser cavity: The laser cavities are arranged in a "J" configuration as shown in Figure 2.3. Mirror holders colored in red hold optics that are reflective for the wavelength of choice and do not reflect the 527 nm pump beam. The pump beam therefore cannot reach the grating or the output coupler and thus cannot damage these components. The pump beam excites the Ti:sapphire crystal, which then emits light between 700 and 1000 nm. The Ti:sapphire light is then passed through a beam expander and hits a first-order holographic diffraction grating. By turning the diffraction grating, the wavelength of choice of the first order is fed back into the Ti:sapphire crystal. This light is then passed through a Q-switch and is finally reflected by the output coupler back into the Ti:sapphire crystal. When the cavity is in perfect alignment, the cavity starts lasing at the wavelength defined by the angle of the diffraction grating. This beam with the fundamental wavelength is shown in Figure 2.3 in red. If the resonance ionization scheme uses the fundamental beam, an output coupler that lets 40% of the light pass is put into the respective mirror holder. Fundamental Ti:sapphire beams are feasible in the wavelength range of around 700–1000 nm.

Since the Ti:sapphire crystal does not absorb every photon from the pump beam, some part of the pump beam leaves the cavity after passing the Ti:sapphire crystal and would be lost. By introducing a focusing bounce-back mirror, the lost beam can be reflected and refocused onto the crystal. This usually results in about 10-20% more energy in the fundamental beam.

Since the turning mirrors reflecting the fundamental beam are not perfect, a small part of this beam leaks out of the cavity. This fraction is focused into a glass fiber which is connected to a HighFinesse/Ångstrom WS6-200 multichannel interferometric wavelength meter. This allows constant monitoring of the wavelength. Furthermore, the diffraction grating sits on a rotation stage, which can be turned by using a New Focus Picomotor linear actuator. An active feedback system is implemented such that wavelength drifts measured

in the wavelength meter are actively compensated by turning the rotation stage using the piezoelectric motor.

To create a second harmonic beam, intracavity doubling can be implemented in these cavities. This doubling setup is shown by blue components and beams in Figure 2.3. A lithium triborate (LBO) crystal is brought into the fundamental beam line. If the crystal axis is tilted at the correct angle with respect to the fundamental beam, two fundamental photons are combined and produce a frequency-doubled photon, i.e., a photon that has half the wavelength of the fundamental photon. Instead of a partially transparent output coupler, the cavity itself is closed by a broadband total reflection mirror that reflects the fundamental beam as well as the second harmonic. To decouple the second harmonic beam from the fundamental, a pickup mirror is brought into the cavity that is reflective for the s-polarized second harmonic and transparent to the fundamental beam. Intracavity doubling allows for higher output power of the second harmonic beam compared to extracavity doubling (see below), since the fundamental beam has much more power inside the cavity than outside and has a smaller diameter. In addition, the beam passes the LBO crystal twice, therefore creating more frequency-doubled photons than in a single pass. Doubled beams are feasible in the wavelength range between 350 and 500 nm.

Tripling the fundamental beam frequency is achieved outside the cavity and the necessary setup is shown in yellow in Figure 2.3. An LBO crystal is mounted, again at the correct angle, right behind a 40% output coupler. This doubles part of the fundamental beam in frequency (extracavity doubling). For subsequent tripling, a β-barium borate (BBO) crystal is used to combine a fundamental and a doubled photon resulting in tripling the fundamental frequency. Tripling however can only take place if the fundamental and the doubled photon have the same polarization. Since the frequency-doubled beam is s-polarized, a quartz crystal rotator is installed between the LBO and BBO crystal. This quartz crystal rotator rotates the s-polarized doubled beam into a p-polarized beam and rotates the fundamental beam fully, such that it stays p-polarized. Since the doubled beam comes out at a slight angle compared

to the fundamental beam (walkoff angle), the LBO and BBO crystals must be mounted as close as possible to each other to achieve the largest overlap and thus the highest irradiance and efficiency. The tripled beam comes out along the axis of the fundamental beam at a slight walkoff angle and is s-polarized. Tripled beams are feasible in the wavelength range of 233-333 nm.

Quadrupling of the fundamental laser wavelength can be achieved in similar ways by combining two doubled photons and double their frequency. Quadrupling can be done either extracavity, or in a mixture of intra- and extracavity. While wavelengths between 175 and 250 nm are theoretically possible by quadrupling the fundamental frequency range of the Ti:sapphire crystal, BBO crystals are limited at low wavelengths and only beams between 205 and 250 nm can practically be achieved. Such beams were not used in this study for ionizing iron and nickel isotopes.

Note that by multiplying the fundamental beam frequency, laser power is lost due to the efficiency of the process itself. While intracavity doubling can achieve a beam that has up to 50% of the fundamental beam energy, extracavity tripling only results in a beam that has about 10% of the fundamental beam energy. In addition, tripled and quadrupled beams should be avoided wherever possible, because such photons have high energies and can potentially nonresonantly ionize mass-interfering atoms or molecules in a two-photon process. This is elaborated in more detail for iron and nickel ionization in Section 2.2.

Laser timings: The timings of the Ti:sapphire cavities are controlled by Q-switches. A Q-switch (or Pockels cell) consists of an electro-optical crystal through which light can propagate. By applying a voltage to the crystal, its phase delay can be modulated. In our case, we switch between two modes. When the voltage on the Q-switch is turned on, the crystal rotates the light away from the p-polarization required for lasing and when the voltage is turned off, the polarization remains unaltered. Our Ti:sapphire cavity is built for p-polarized light, hence, only works when no voltage is applied to the Q-switch. By setting the volt-

age drop timing of the Q-switch, the timing of the laser pulse can be controlled within a certain range. For one laser pulse, the system behaves as follows: the pump laser fires at a defined time and excites the Ti:sapphire crystal. Since the Q-switch is at voltage at this time, the Ti:sapphire cavity cannot fire. As soon as the voltage in the Q-switch is dropped, the Ti:sapphire laser is unblocked, builds up energy, and fires. By shifting the timing of this voltage drop, timings of all laser cavities can be set individually such that they overlap. It is worth noting that not only does this allow us to precisely control the timing of the lasers, but also provides us with 10 to 20% more power by fully exciting the Ti:sapphire crystal before firing.

Beam telescopes: The laser beams exiting the cavities are divergent and therefore need to be focused to a size of approximately 1.5 mm FWHM diameter above the sample, which is several meters away from the laser. Laser beams and their propagation are properly described by a beam waist, i.e., the diameter of the beam in focus. The beams diverge under ideal conditions as a Gaussian beam with a set divergence that can be measured. The beam quality, i.e., how closely a laser beam has a Gaussian profile is described by the so called M^2 factor. This factor is defined as follows:

$$\theta = M^2 \frac{\lambda}{\pi \omega_0} \tag{2.1}$$

Here, θ is the half-angle beam divergence, λ the wavelength, and ω_0 the beam waist. In the ideal case, M^2 is equal to one which means that the laser beam is diffraction-limited. Our laser beams are very close to this limit, M^2 measurements of the CHILI cavities show values of around 1.2, 2.1, and 3.2 for the fundamental, second harmonic, and third harmonic beams, respectively. Since the sample is several meters away from the cavity output itself, the laser divergence can be simplified and described by a constant angle divergence. In CHARISMA, we used single lenses, each of which having a focal length > 1 m, to focus the beam to the correct spot size, in CHILI we implemented Galilean beam telescopes. A schematic of such a

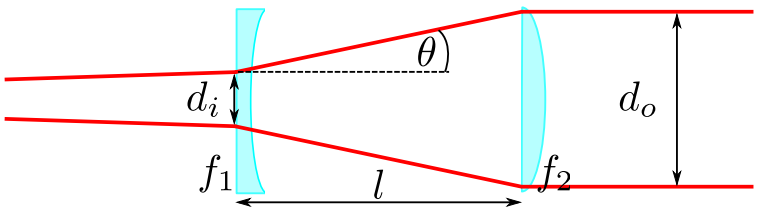

Figure 2.4 Schematic of a Galilean beam telescope.

telescope is shown in Figure 2.4. The magnification m of such a telescope can be calculated by:

$$m = -\frac{f_2}{f_1} = \frac{d_o}{d_i} \tag{2.2}$$

The distance l between the two lenses is furthermore given by $l = f_1 + f_2$, which is the condition such that the outgoing beam is parallel. Note that for the Galilean telescope, the first lens has a negative focal length and disperses the incoming beam. This allows us to build shorter telescopes compared to a Keplerian telescope, for which both lenses would have positive focal lengths. Galilean telescopes further avoid focusing the laser beam in between the lenses.

Beam combiner: Before the Ti:sapphire beams go through the vacuum chamber and ionize neutral atoms, they have to be aligned such that they overlap. To achieve collinear beams, CHARISMA uses a periscope setup several meters away from the chamber. Each laser beam is reflected off an individual mirror, all of which are close to each other. This allows the beams to pass through the neutral atom cloud and be overlapped in the center. However, there is a slight angle between the beams separating them from each other again after they passed the sample cloud. This small shift however is negligible for single or double passing of the sample cloud, i.e., when a bounce back mirror is installed.

In CHILI, three prisms are used to colinearize the six incoming laser beams. Figure 2.5 shows an image of the prism setup used. The red arrow indicates one of the incoming beams. All six beams pass through the three prisms, which combine them onto a single line. All

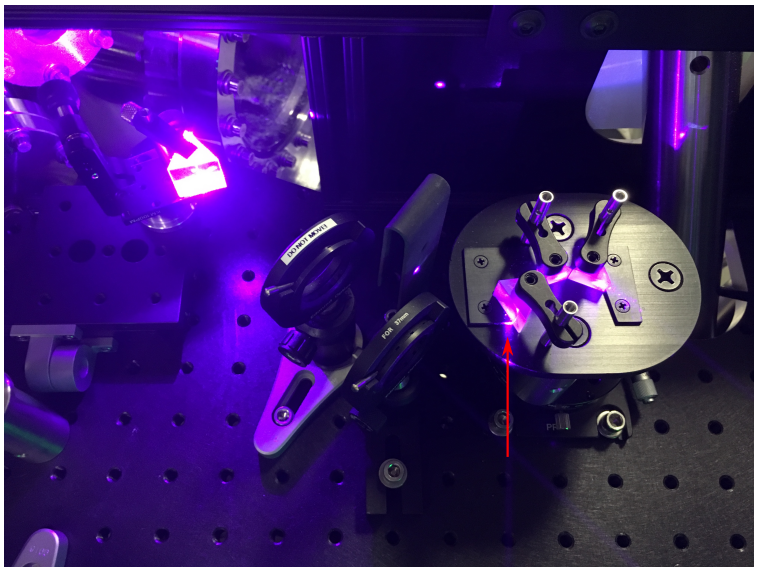

Figure 2.5 Beam combiner used in CHILI to make the six incoming laser beams collinear.

prism surfaces are aligned to the beams close to Brewster's angle, minimizing losses due to reflections. However, this Brewster's angle setup requires the incoming beams to be p-polarized. Since doubled and tripled laser beams leave our cavities s-polarized as described above, tunable half-wave plates are used to turn the polarization back to p-polarization before entering the beam combiner. In addition, the laser beams must be precisely aligned relative to the beam combiner. This alignment is achieved by using mirrors mounted on translation stages. This way, the correct line of the laser beam can be set using only one mirror. Two mirrors after the beam combiner then allow bringing the beams onto the perfect path through the chamber. The left side of Figure 2.5 shows a prism which acts as a low reflectance thick optic, which picks up a fraction of the combined beam and guides it into a beam profiler. The profiler is at the same distance from the pickoff point as the center of the sample. The profiler allows correcting of the beam position and tuning of the telescope focus. The same system with a pickoff prism and a beam profiler setup is available for beam guidance and quality control on CHARISMA.

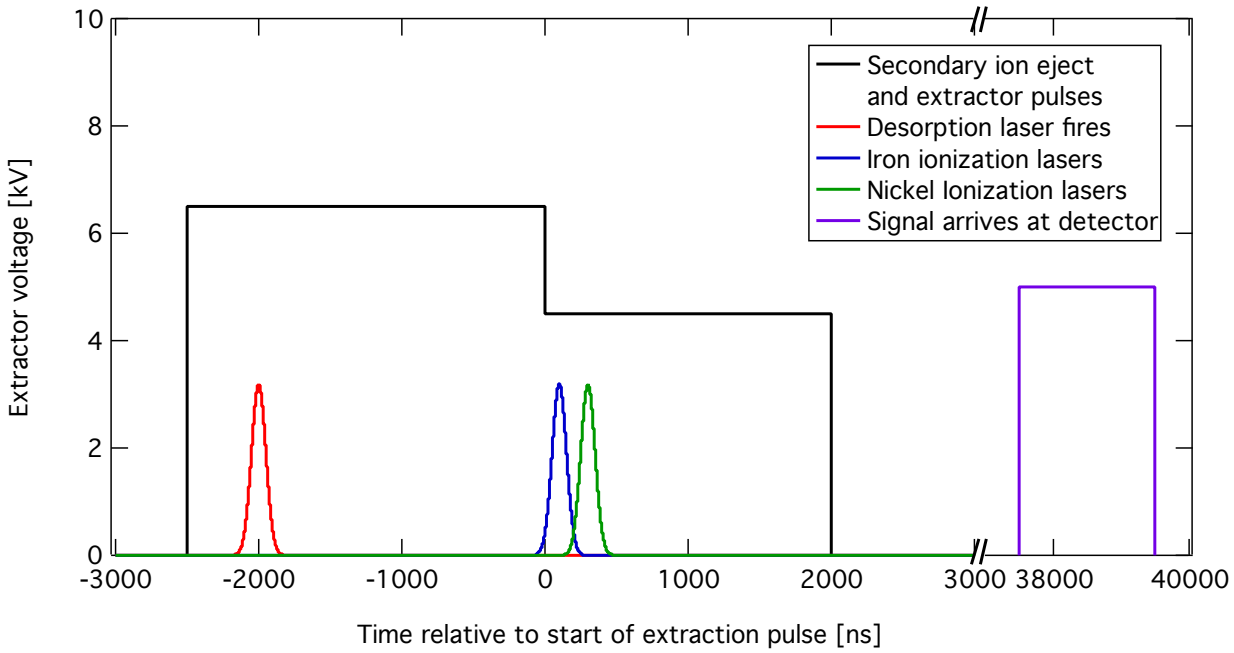

Figure 2.6 Schematic of the CHILI RIMS pulsing scheme for the ionization of iron and nickel isotopes.

2.1.3 Mass separator

Ions are separated by their mass-to-charge ratio in a time-of-flight mass analyzer, which is schematically shown in Figure 2.1. Laser ionization is selective for one atomic state, hence doubly charged ions are not formed effectively by the lasers. Ions are electrostatically injected into a flight tube by the extraction optics. This injection event marks the start time of the total flight time. The injection event can be either achieved by pulsing the voltage on the extraction optics after photoions were created, or by creating photoions after the extraction optics is already at voltage. At the end of the flight tube, the ions enter the reflectron, an ion optical mirror designed to softly turn the ions around and send them towards the detector. Hitting the detector marks the end of an ion's flight time. This process is repeated at 1 kHz, and, over time, an intensity versus time-of-flight spectrum is generated. The time-of-flight can be then translated into a mass-to-charge ratio.

The actual pulsing of the electrostatic voltages is shown in Figure 2.6. While the desorption laser hits, secondary ions that are created are ejected from the system in a secondary ion

ejection event. At time zero, the voltage is set such that ions present or thereafter created above the sample can pass through the mass spectrometer. In CHARISMA, the secondary ion ejection pulse is turned off approximately 100 ns before the extraction voltage is turned on. The Ti:sapphire laser beams are brought into the chamber around 50 ns before the extraction is brought up to voltage. Pulsing the voltage on the extraction optics then defines the start time. The CHILI instrument follows a slightly different scheme (see Figure 2.6). Here the secondary ion ejection pulse pulse is left on as long as possible and then the voltage is dropped to the level at which ions can pass the mass spectrometer and reach the detector. The Ti:sapphire lasers are subsequently brought into the analysis volume and create the photoions. Here, the ionization lasers mark the start time of the photoions. This procedure is essential for separating iron and nickel ions from each other (see Section 2.2).

At the time the photoions are created, they fill a volume that corresponds to the intersection of the neutral particle cloud and the ionization laser volume. There is a gradient of voltage potentials in the extraction field, yielding slightly different initial energies of the photoions when they are introduced into the time of flight mass spectrometer. In addition, the photoions have various energies from the desorption event. These energy differences are small compared to the extraction voltage of 2 kV on CHARISMA and 4.5 kV on CHILI. However, the energy spread – if not corrected – would still yield peak-broadening such that individual masses cannot be properly separated. To correct for the initial energy distribution and achieve energy focusing, we use a two-stage reflectron as described by Mamyrin et al. (1973). In the first stage, the ions are simply decelerated. The second stage is defined by a linear slope in voltage that is tuned to minimize the spread in the time-of-flight of ions of the same mass when arriving at the detector. An ion with a high initial energy penetrates deeper into the reflectron before turning around than an ion a with low initial energy. If tuned properly, the flight time difference of the two ions will cancel out at the detector, i.e., the ion with a high initial energy though faster, travels slightly further than the ion with low initial velocity, therefore arriving at the same time at the detector.

Various lenses in the system (see Figure 2.1) prevent the ion beam from spreading too much and therefore guide its way through the reflectron to the detector. Right before the ions hit the detector, a grid, which is usually kept at 0 V, could be used as a high-pass filter as well as being pulsed to reject a certain window of the mass spectrum. However, this feature has not been used for this study.

2.1.4 Detector

CHARISMA and CHILI are each equipped with a Photonis Gen2 UltraFast microchannel plate detector with a pulse width of < 200 ps FWHM and a single anode. The detector signal is fed into a P7889 multiple-event time digitizer from FAST ComTec GmbH with 100 ps time resolution. The dead time on the detection system has been measured with CHILI and is 600 ps (Stephan et al., 2016), i.e., when an ion arrives, no more ions can be measured within the next five time bins. If a reasonable count rate is set, dead time effects can be corrected for (Stephan et al., 1994).

All the data measured with CHILI were recorded as single-shot spectra, i.e., the arrival time of every individual ion was recorded. This allows us to study the measurement in detail and to see how steady the count rate was over time. On CHARISMA, we did not have this capability, and we bundled 25000 shots together into one spectrum. Data evaluation is described in Sections 2.4 and 2.5.

2.1.5 Differences between CHILI and CHARISMA

CHILI, in its current status (Stephan et al., 2016), is very similar to CHARISMA. The main differences are that six instead of three Ti:sapphire lasers are available for resonance ionization and that the software is capable of recording single-shot data, i.e., the stop time of every individual ion is recorded. In addition, many technical improvements have been implemented in CHILI. The 2.5 times higher extraction voltage in CHILI results in a higher useful yield. The useful yield could be measured with CHILI to be around $\sim$1% for iron and

$\sim$ 0.78% for nickel (Stephan et al., 2016). We did not determine the useful yields on the CHARISMA instrument and therefore cannot directly compare the two instruments. The best indicator that CHILI does have a higher useful yield than CHARISMA however is the actual iron measurements from presolar SiC grains. Assuming that the grains measured with CHARISMA did not have lower iron concentrations than the presolar SiC grains measured with CHILI, measurements with CHILI allowed us to count many more ions than with CHARISMA in individual grains of similar size. Hence the statistical errors are generally smaller with CHILI (see Figure 3.4). Further technical improvement are the sub-μm reproducibility sample stage from Alio Industries as well as the built-in field emission scanning electron microscope (e^-CLIPSE Plus field emission electron gun as well as an Everhart-Thornley secondary electron detector, both from Orsay Physics). This built-in electron microscope allows measurements of presolar grains that are close together since the desorption laser crater can actually be seen and thus be precisely positioned. Mechanical improvements of the Ti:sapphire laser cavities helped to faster replace components like Ti:sapphire crystals, which occasionally "burn" (in which their mirror-polished surfaces are damaged) due to software and operator errors.

2.2 Resonance ionization of neutral iron and nickel atoms

Figure 2.7 shows the resonance ionization schemes that was developed for iron (left) and nickel (right). Both ionization schemes were adapted from Moore (1971). The key to a successful ionization scheme is high and stable laser power and wavelength as well as broad bandwidth. All of these quantities inevitably fluctuate from one laser pulse to the next. The ideal ionization scheme yields isotope ratios that are robust against these fluctuations. The iron and nickel ionization schemes terminate on excited states above the ionization potential. We used wavelength scans of excited states by Worden et al. (1984) for iron and by Page and Gudeman (1990) for nickel to find the best transitions for resonance ionization. Once the atom is excited above the ionization potential, the respective electron is ejected

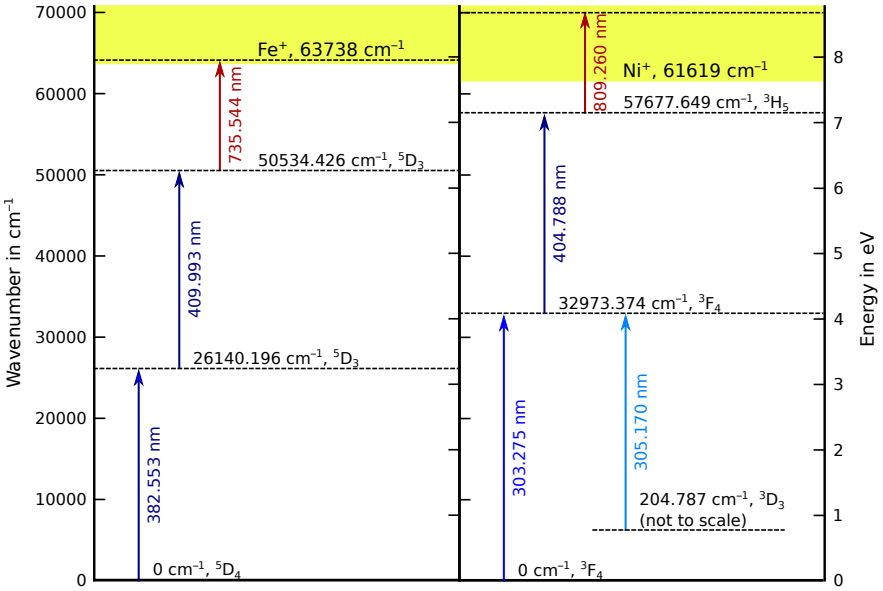

Figure 2.7 Iron and nickel ionization scheme.

and the atom becomes ionized. To determine the optimal wavelength, we performed scans around the literature values and settled on these states that provide both high ion signal and high isotopic precision. We made similar scans for the other transitions and measured the isotopic precision and accuracy to assure our selected ionization scheme is sensitive, precise, and robust.

Saturation curves (ion signal vs. laser power) were obtained to show that all transitions were saturated. Figure 2.8 shows the saturation curves for all of the scanned transitions of the iron and nickel scheme. All curves linearly increase in the beginning and then tilt and start leveling off. This means that saturation for a given transition is reached. The slow increase when increasing the power beyond saturation results from the laser volume increase – the tails of the laser beam get more intense and saturation is achieved in areas off center where the transitions are now closer to saturation due to the higher absolute intensity of the tails. Bouncing the laser beams back and forth multiple times, as is intended for CHILI in the future, will increase the volume and therefore result in a higher ion signal. The iron ionization laser step is the only transition that is barely saturated, i.e., the curve starts

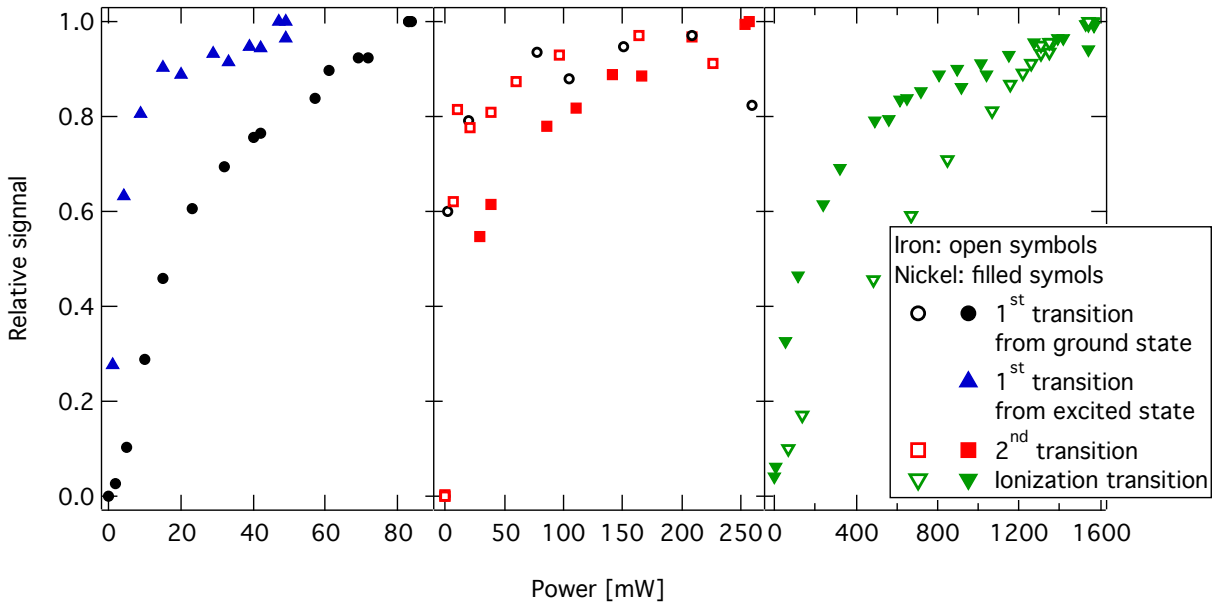

Figure 2.8 Saturation curves for all iron (open symbols) and nickel lasers (filled symbols).

tilting over but has not reached the full plateau yet. However, the normal isotopic ratios measured on terrestrial SiC standards show that the isotope ratios are not sensitive to the laser power and the transition must therefore be close to saturation.

Isotope shifts are small in the case of iron and nickel (generally less than 1 GHz or 2.4 pm at 850 nm wavelength), and are significantly smaller than the bandwidths of the Ti:sapphire lasers (∼10 GHz or 24 pm at 850 nm wavelength). Thus fractionation due to shifts among the various isotopes is negligible. However, mass-independent fractionation in iron and nickel occurs due to the odd-even effect, which leads to different sensitivities for isotopes with odd mass numbers versus isotopes with even mass numbers (Fairbank et al., 1989; Wunderlich et al., 1992). It is therefore crucial to measure appropriate standards to normalize the sample to. Nickel has a low-lying excited state at 204.787 cm^{-1}, i.e., just above the ground state. Using four lasers initially, we determined first if the ground or the excited state is more populated with neutral atoms. Figure 2.9 shows an example of the population study using ion sputtering on stainless steel. Nickel isotopes were measured repetitively between the different states. The decrease in total signal is minimal compared

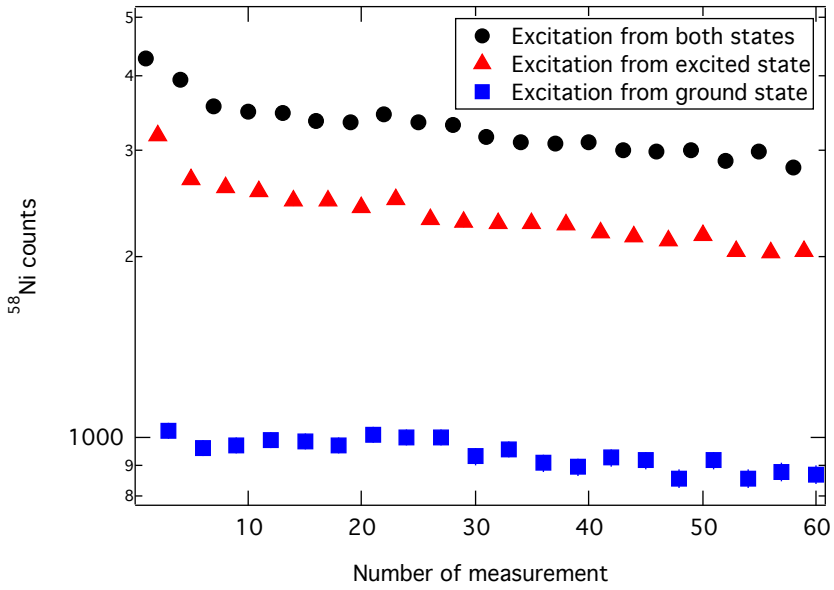

Figure 2.9 Population study of the nickel ground and excited state using ion sputtering on stainless steel.

to the total signal. Figure 2.9 shows that 71.1% are in the excited state and 28.2% of the sputtered neutrals are in the ground state. Pump over from one state into the other is less than 1%, since the total measured signal from both states sums up to 99.3%. This means that atoms that are excited from the ground state to the first excited state do not decay into the low-lying excited state efficiently, and vice versa. We also tested ion sputtering on a terrestrial SiC wafer with some iron and nickel content and found the same distribution between the ground and excited states. In the case of ion desorption using the 351 nm laser, the states are differently populated. Testing the different populations in this case is very difficult, since stable count rates cannot be achieved easily, and therefore, results between the different states vary more from measurement to measurement than they vary between the states. However, while watching the ion signal on an oscilloscope and flipping between ionization from the ground state and ionization from the excited state, we estimate that more than 50% of the desorbed neutrals are in the excited state. Since CHILI only has six tunable Ti:sapphire lasers, and three of these are used for the iron ionization scheme, we decided to ionize the neutral nickel atoms from the low-lying excited state. This however

means that slightly less than half the desorbed nickel neutrals cannot be measured, lowering our useful yield for nickel by roughly a factor of two compared to a four-laser scheme.

Since resonance ionization is orders of magnitude more efficient than nonresonant multiphoton ionization, other elements in the cloud of neutral atoms are largely transparent to the laser light and hence hardly ionized at all (Hurst et al., 1979). To show the elemental suppression factors, we measured iron and nickel isotopes in stainless steel samples. The discrimination of one element versus the other is measured by acquiring long mass spectra using the ionization lasers of only one element, e.g., measuring only the nickel isotopes and looking for a nonresonant iron signal. Using the iron scheme, we acquired a long-term mass spectrum of a stainless steel sample with an atom ratio of iron to nickel of 9.0. We did not detect any nickel isotopes in this measurement. This gives us a lower limit for the nickel elemental discrimination value of $> 5.2 \times 10^4$ in the iron scheme. Assuming an elemental ratio of one, the interference on ^{58}Fe from ^{58}Ni can be estimated as $< 4.7\,‰$. The elemental discrimination of iron by the nickel ionization scheme, measured in a different stainless steel sample with an iron to nickel atomic ratio of 9.5, is 3.6×10^5. Assuming an elemental ratio of one, ^{58}Ni gets a contribution from ^{58}Fe of 11.4 ppb. Since we want to measure the iron and nickel isotopic composition in a given sample simultaneously, the minor isotope ^{58}Fe would be dominated by the ^{58}Ni peak if the two elements are not separated from each other in the mass spectrum.

2.3 Mass separation of iron and nickel isotopes

In order to separate ^{58}Fe from ^{58}Ni, a mass spectrometer with a mass resolution $\frac{m}{\Delta m}$ of 28000 is necessary. The CHILI instrument has currently a resolution of around 1000 in the iron and nickel mass range and therefore cannot resolve these two peaks from each other. Laser ionization however allows us to solve the problem of isobaric interference. The start time of the iron and nickel ions is defined by their respective ionization times, i.e., the time when the Ti:sapphire lasers ionize the cloud of neutrals. Using the Q-switches, we delay the

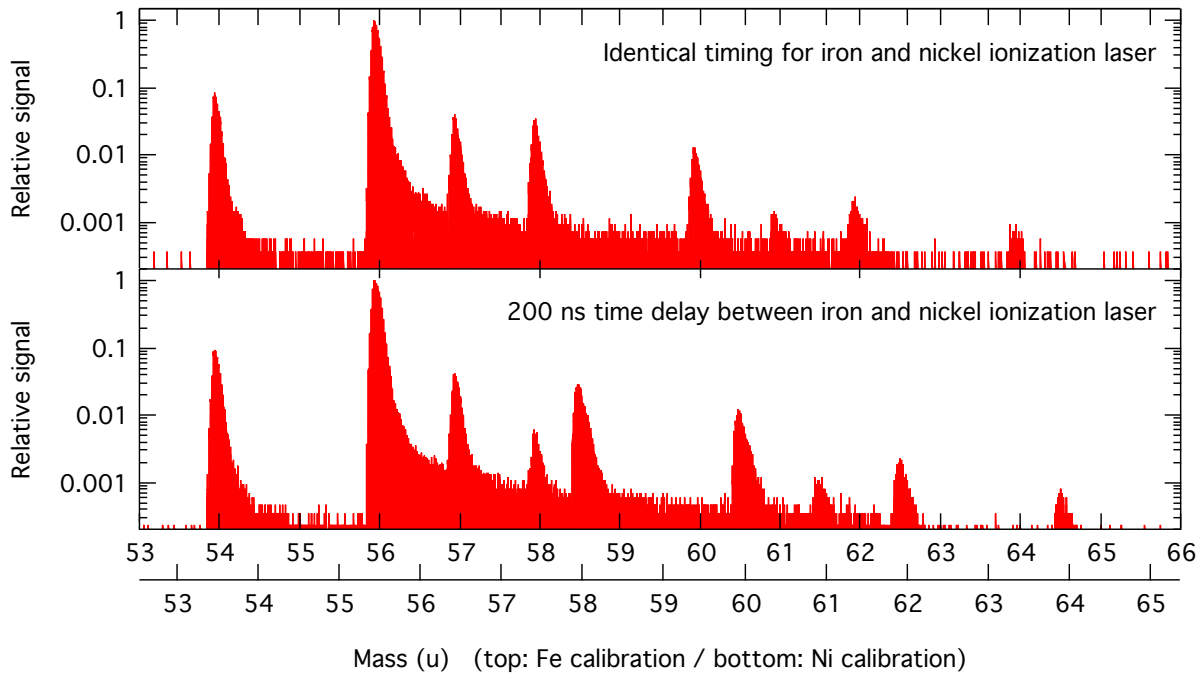

Figure 2.10 Iron and nickel resonance ionization without a time delay between the respective Ti:sapphire lasers (top) and with a 200 ns time delay (bottom). In the bottom part, it is clearly shown that the 200 ns time delay allows simultaneous measurement of ^{58}Fe and ^{58}Ni without isobaric overlap.

nickel ionization lasers by 200 ns with respect to the iron ionization lasers. This difference in start time results in an apparent mass difference in our system of around 0.5 u. Therefore, a mass resolution of around 120 would already suffice to separate the peaks, which allows us to measure ^{58}Fe and ^{58}Ni simultaneously with CHILI. Figure 2.10 depicts this mass separation. The top part of the figure shows the situation with no time delay between the ionization events, the bottom figure shows the separated mass spectrum.

2.4 Measurement protocol on CHARISMA

Presolar SiC grains mounted on gold foil were located using the built-in optical microscope. Due to in-vacuum misalignments of the Schwarzschild microscope optics, image distortions like ghosting made it difficult to find presolar grains on the mount. Using landmarks on the gold foil such as grooves and scratches we navigated close to the presolar SiC. By moving

the desorption laser over the mount, we looked for signal until we found the presolar SiC grain. The grain was then subsequently measured by rastering the desorption laser over it using a two-axis scanhead. The power of the desorption laser was adopted using a manually controlled half-wave plate that is followed by a beam-splitting cube. The half-wave plate hereby polarizes the laser light to a mixture of s- and p-polarization. The beam cube then lets the p-polarized light straight through, the s-polarized part is dumped into a beam stop. By turning the half-wave plate, the power that reaches the sample can be adjusted. The ideal power is chosen by looking at the signal and correcting for too high or too low signal.

When choosing the appropriate count rate, two factors have to be considered. First, a low count rate results in a low signal-to-noise ratio. If the count rate is too high, the detector cannot count every event due to dead time, i.e., after an ion hits the detector, it cannot detect a second ion hitting within a given time window. Dead time effects can be corrected for (Stephan et al., 1994). However, every correction adds uncertainty to the actual measurement. Therefore, we tried to keep the count rate at a level such that only 5-10% of the shots contain an ion count. However, the desorption process is not as steady as, e.g., ion sputtering, and sudden rises in the count rate (blasts) can occur. We constantly monitored the count rate during the measurement. While CHARISMA has the same detector and time-to-digital converter as CHILI, the software was not set up to record single-shot data. We therefore grouped the measurements into shots of 25000, which is equal to 25 s of data at a repetition rate of 1 kHz. If signal blasts were observed in one of these groups, the whole group was rejected from the analysis. This method yielded reliable measurements on the standard as well as on presolar grains.

Finally, isotope ratios were calculated from adding signals from all shots that showed no blasts and normalizing the signal ratios to those obtained for the chromium carbide standard, which was assumed to have Solar System isotopic ratios. Matrix effects between chromium carbide and SiC can be neglected as shown in Section 2.6.

Since CHARISMA has only three Ti:sapphire lasers, we only measured iron isotopes in

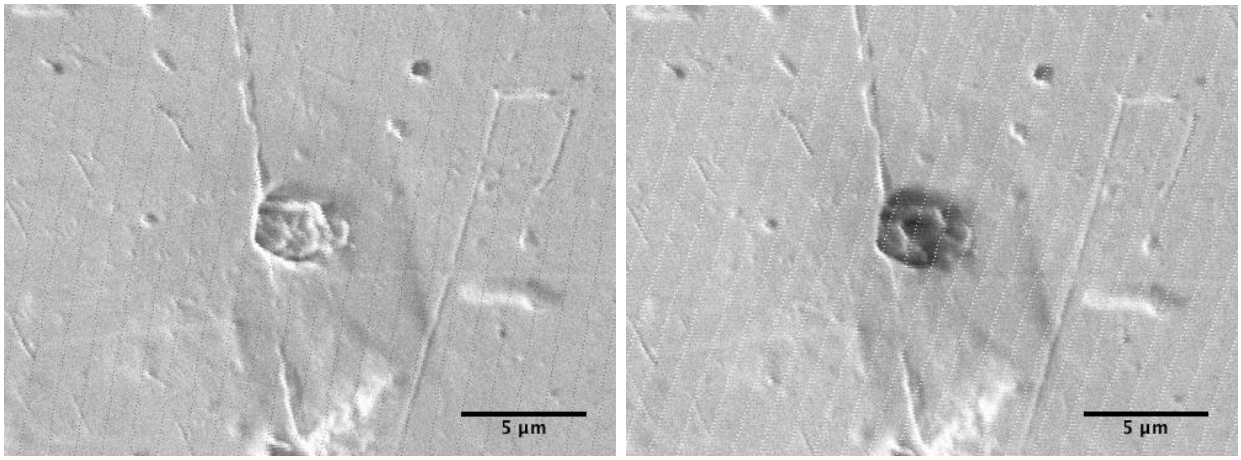

Figure 2.11 Image of grain N82 taken with the scanning electron microscope in CHILI before (left) and during (right) the measurement. The right image clearly shows the crater produced by the desorption laser in the center of the grain.

presolar SiC grains. In addition, most of the development of the nickel ionization scheme was done using CHARISMA.

2.5 Measurement protocol on CHILI

With CHILI, presolar SiC grains as well as standards were located using the scanning electron microscope and were measured using the 351 nm desorption laser without rastering the beam over the sample. By studying the secondary electron image while measuring, we saw that a grain gets desorbed evenly when the desorption beam is well positioned, i.e., the grain starts desorbing from the center, and with increased laser power, more of the sides of the grain get desorbed as well. Rastering the laser beam (as done in CHARISMA) is therefore not necessary, if the laser beam can be positioned precisely. Figure 2.11 shows a presolar grain before the measurement (left) as well as during laser desorption (right) using CHILI's scanning electron microscope. The right image shows clearly the crater from the desorption laser in the middle of the grain, indicating perfect positioning for the measurements. Over time, this crater gets deeper and wider, until the grain is completely gone. With higher laser power, the gold surrounding the grain starts melting and the crater becomes more dominant.

An interesting artifact in the secondary electron images taken in CHILI (Figure 2.11) are the slightly tilted black (left image) and white (right image) lines crossing the images. The black lines show the influence of the pulsed target voltage on the secondary electron detection. The image in these spots seems to be underexposed, resulting in dark lines. The white lines are taken during the RIMS measurements, while the desorption as well as the ionization laser beams are in the chamber, and result from light detected by the photomultiplier in the secondary electron detector. The laser-induced overexposure masks the voltage pulsing image errors since both events occur approximately at the same time.

After material is desorbed from the surface, six Ti:sapphire lasers are used to resonantly ionize iron and nickel as well as separate the two overlapping peaks at mass 58 (see Section 2.3). After a flight path of 3.65 m, the ions hit the detector where they are registered. CHILI's control software then stores every single ion arrival time into a file. Single shot recording also allows the computer to control the signal in real time. A recently implemented routine allows controlling the half-wave plate of the desorption laser and automatically adjusting its power, such that the count rate is held at a constant level. This allows for a faster reaction time when a blast occurs. The single-shot data furthermore allows us to analyze the data afterwards for blasts and cut those regions out of the measurement if adjusting the power did not occur fast enough.

The data evaluation of CHILI spectra is done using two software packages developed by Thomas Stephan. The package *CHILISpec* is first used to read and export the part of interest of the spectrum. The exported spectrum can then be read and looked at with the software package *TSTSpec*. Here, the integral parameters for the peak areas as well as the areas for the background subtraction are defined. Once the integration parameters and background areas are defined, these limits are read back into *CHILISpec*, which subsequently corrects the data for dead time effects and looks for laser blasts. Dead time effects are corrected according to Stephan et al. (1994) assuming a detector dead time of 600 ps (Stephan et al., 2016). Laser blasts are detected and rejected in two different ways. First, if 1000 shots contain more

than 2500 counts, we assume that a laser blast happened in this area and the 1000 shots are rejected from further analysis. In addition, if an individual shot contains more then 10 counts, this shot is rejected as well. These rejection parameters were found experimentally by measuring a stainless steel standard at different count rates. At low count rates, laser blasts usually do not occur, however, they get more frequent at higher count rates. By comparing the results of these measurements to each other, we determined the best rejection parameters such that the standard measurements at different count rates always result in the same isotope ratios. Note that only a few percent of the total number of shots are usually rejected in any given measurements. Finally, measurements of presolar SiC are at the end normalized to the measured standard material, and we assume that the isotopic composition of the standard is solar (Lodders et al., 2009).

2.6 Standard measurements

To test the iron and nickel resonance ionization schemes, several different standards were tested. Even though RIMS has much lower matrix effects than conventional SIMS methods, we found some slight isotopic fractionations depending on the standard. Figure 2.12 shows the isotopic composition averaged over all of our standard measurements (see also Table 2.1 for the plotted values). Isotope ratios are given throughout this work as δ-values, which describe the permil deviation of the measured sample from a measured standard. The isotope used for normalization is always the most abundant one, unless otherwise noted. For example, the δ^{54}Fe is defined as:

$$\delta\left(\frac{^{54}\mathrm{Fe}}{^{56}\mathrm{Fe}}\right) = \left(\frac{\left(\frac{^{54}\mathrm{Fe}}{^{56}\mathrm{Fe}}\right)_{\mathrm{measured}}}{\left(\frac{^{54}\mathrm{Fe}}{^{56}\mathrm{Fe}}\right)_{\mathrm{standard}}} - 1\right) \times 1000 \qquad (‰) \tag{2.3}$$

The stainless steel measurements were done on our sample holder, in which the atomic iron / nickel ratio is 9.0. The chromium carbide (Cr_2C_3) grains as well as the terrestrial SiC

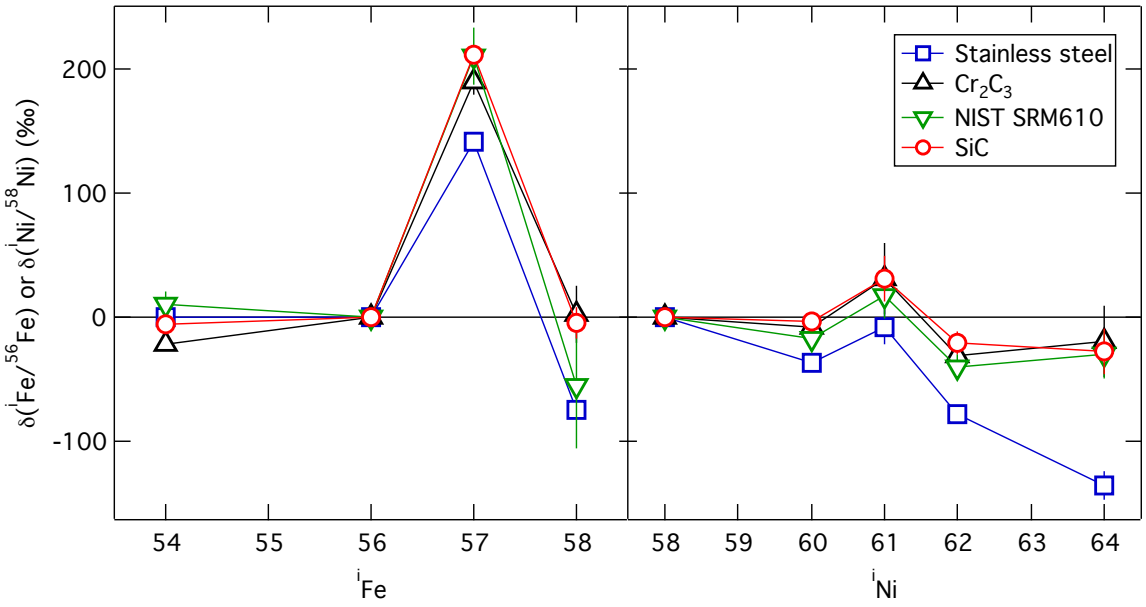

Figure 2.12 Iron and nickel isotopic compositions averaged over all standard measurements. Error bars show 2σ statistical uncertainties.

grains were located on the same mount as the measured presolar grains, both of them have an unknown iron and nickel concentration. The Cr_2C_3 grains were dispersed between the presolar SiC grains and were used previously to normalize chromium isotopic measurements as described by Levine et al. (2009). The SiC standard consists of submicrometer-sized grains that were mounted at the edge of the gold mount in order to standardize the silicon and carbon isotopic measurements performed with the NanoSIMS. This SiC standard also showed clear iron and nickel signals and could therefore be used for standardizing the presolar grain measurements. Since these SiC grains were industrially produced, we assume that they have solar isotope composition, a fair assumption to normalize the large isotope anomalies found in presolar SiC grains. The NIST SRM 610 standard contains around 500 ppm of iron and nickel and was ground with an agate mortar and pestle to a grain size of a few tens of μm prior to being mounted on a gold surface. Clearly visible in all isotope measurements shown in Figure 2.12 is the odd-even effect. The odd isotopes ^{57}Fe and ^{61}Ni have a higher sensitivity in the resonance ionization process and therefore have positive δ-values. Within uncertainty,

Table 2.1. Averaged isotopic measurements of all standards. Uncertainties are 2σ.

Isotope ratio	Measurement for given standard (‰)			
	Stainless steel	NIST SRM610	Cr_2C_3	SiC
δ^{54}Fe	-0.3 ± 1.5	$+9.7 \pm 11$	-22 ± 4.8	-5.7 ± 2.4
δ^{57}Fe	$+141 \pm 3.5$	$+210 \pm 23$	$+189 \pm 10$	$+211 \pm 4.7$
δ^{58}Fe	-74 ± 7.7	-55 ± 50	$+2.5 \pm 23$	-4.3 ± 413
δ^{60}Ni	-37 ± 2.8	-17 ± 4.3	-8.4 ± 6.4	-4.0 ± 4.2
δ^{61}Ni	-8.5 ± 13	$+17 \pm 19$	$+31 \pm 29$	$+31 \pm 19$
δ^{62}Ni	-78 ± 6.3	-40 ± 10	-31 ± 15	-21 ± 9.5
δ^{64}Ni	-135 ± 12	-30 ± 20	-20 ± 29	-28 ± 19

all standard measurements except for the stainless steel measurement agree with each other. The stainless steel deviates however significantly from the other standards. Aside from the odd-even effect, which is clearly visible in the stainless steel standard measurements, the measurements also seem to be mass-dependently fractionated compared to the measurements of the other standards. One possible explanation for this difference is desorption of material from different matrices. It is well known that sputtering processes fraction isotopes based on their velocities (e.g., Gnaser and Hutcheon, 1987; Gnaser, 1999) since it is essentially a distillation process, which can fractionate isotopes mass-dependently. Laser desorption is basically the same as a distillation process, however, in a different energy regime than ion sputtering. Different materials will have different "distillation temperatures" and can therefore fractionate isotopes. This could explain the effects that are seen in the stainless steel compared to the other standards. In general, this shows the importance of measuring standards that are close in their matrix to the sample of interest in order to normalize the samples.

All CHILI measurements were normalized to the SiC standard material, all CHARISMA measurements were normalized using the Cr_2C_3 standard. Since both standards agree well with each other and SiC obviously matches the presolar grain matrix, we do not expect any shifts in our measurements due to matrix effects.

CHAPTER 3

SIMULTANEOUS ANALYSIS OF IRON AND NICKEL ISOTOPES IN PRESOLAR SIC GRAINS

3.1 Introduction

Most presolar SiC grains originated in AGB stars and therefore carry their isotopic signatures, especially in *s*-process isotopes. The majority of the variations in *s*-process isotopes can be attributed to different masses, metallicities, and different mean neutron exposures in the presolar grain's parent AGB stars. However, certain elements like silicon and titanium in presolar grains vary in isotopic composition in ways different from what is expected for AGB stars (e.g., Nittler, 2005).

Using CHARISMA at Argonne National Laboratory, we measured 13 presolar SiC grains for their iron isotopic composition. These grains were subsequently measured for their carbon and silicon isotopic composition with the CAMECA NanoSIMS 50 at Washington University in St. Louis. Carbon and silicon are good indicators for the type of parent star from which the individual grain formed. In the same NanoSIMS measurement session, we classified many more presolar grains that were later measured for their iron and nickel isotopic composition with CHILI at the University of Chicago. Details on these RIMS instruments are given in Chapter 2, experimental procedures discussed here thus solely describe non-RIMS related methods.

3.2 Analytical methods

3.2.1 Sample Preparation

Presolar grains analyzed in this study are from the RWB6 separation from the Murchison CM meteorite (Levine et al., 2009) and are mostly in the size range of 2 to 4 μm. The grains were acid-cleaned prior to mounting on a high purity gold foil, as described by Levine et al. (2009).

On the same mount, we deposited terrestrial Cr_2C_3 that contained unknown trace amounts of iron and nickel. The Cr_2C_3 grains were used to normalize the iron isotopic compositions measured with CHARISMA. In preparation for NanoSIMS analysis after the CHARISMA measurements, we deposited fine-grained terrestrial SiC on the edge of the same mount. This terrestrial SiC was used to normalize the NanoSIMS data. It also contained trace amounts of iron and nickel and could therefore be used to normalize all subsequent isotopic analyses measured on the CHILI instrument. Aside from the SiC standard measurements, we continuously monitored the iron and nickel isotopic and elemental composition of stainless steel with an elemental iron-to-nickel ratio of 9.0 as well as a NIST SRM610 standard glass that was mounted separately.

3.2.2 Mount Contamination

As described in Section 3.2.1 and by Levine et al. (2009), great care was taken to ensure that the presolar grains were clean of residual material from the host meteorite and that they were not contaminated with iron and nickel during the separation process. However, even after cleaning the surface of the gold foil using a Ga^+ ion beam, we found residues of iron and nickel in the gold. This contamination therefore was not solely on the surface but also in the bulk material. We performed multiple blank measurements on the gold surface and learned that (1) small surface contamination is found at the beginning of a measurement and (2) further contamination is found when the desorption laser exceeds a certain threshold value. This threshold value is coincidental with a visible crater appearing on the gold mount, i.e., a lot of material is removed. When measuring presolar grains, the surface contamination could simply be removed by excluding the first several thousand shots from the evaluation, i.e., by starting the measurement a few seconds after the desorption laser started desorbing material. To avoid further contamination, we ensured that measurements on the presolar grain were always done at desorption laser powers that are below the "cratering" threshold. Using the same procedure on a blank gold spot as we used for measuring presolar grains, we

determined that the maximum contamination in a given presolar SiC grain from the gold is 3.4% and 6.4% of the total iron and nickel, respectively, measured in the sample.

3.2.3 Scanning Electron Microscopy of Presolar SiC Grains

The SiC grain mount was imaged and mapped using scanning electron microscopy. We also performed energy dispersive X-ray spectroscopy (EDS) to confirm that the grains on the mount were SiC grains prior to performing RIMS measurements. After RIMS analysis, we imaged the grains again to check for residual material. Three out of the 13 grains from the preliminary study did not have enough residual material left to be classified by NanoSIMS. One of the grains analyzed with CHILI was missed during prior NanoSIMS classification. All of these grains are subsequently treated as unclassified. About 93% of all presolar SiC grains are mainstream grains, about 1% Y and about 1% Z grains (Zinner, 2014). These three types are in agreement with an origin in AGB stars. The chance that all four unclassified grains come from AGB stars is therefore 86%; in addition, their isotopic compositions agree with the other AGB star grains that we measured. We therefore include these unclassified grains in our discussion on AGB stars and GCE.

3.2.4 Classification of Presolar SiC Grains

A Cs^+ beam was used for sputtering and negative secondary ions of ^{12}C, ^{13}C, ^{28}Si, ^{29}Si, and ^{30}Si were detected simultaneously. A fine-grained synthetic SiC standard was used for normalization of the NanoSIMS isotopic results. The standard grains were placed outside the area containing the presolar grains and did not interfere with grain analyses. We used a low ($< 0.5\,pA$) Cs^+ primary ion beam current to classify all presolar grains with residual material. The low current allowed a high enough precision to classify the presolar grains while leaving enough sample material for subsequent RIMS analysis.

3.3 Models

3.3.1 AGB Star Nucleosynthesis Models

We compare our results for iron and nickel isotopic compositions to two different sets of nucleosynthesis models. The Torino models are described by Gallino et al. (1998), subsequent updates were published by Bisterzo et al. (2010) and Käppeler et al. (2011). The FRUITY models are described by Cristallo et al. (2009, 2011).

The Torino models use the FRANEC code (Straniero et al., 1997, 2000, 2003, 2006) to calculate the stellar evolution of stars between 1.5 and 3 $M_{\odot}$. Only a limited number of isotopes are considered for stellar evolution, i.e., only the ones that release a significant amount of energy in the nuclear reactions such that they influence the evolution of the star. Nucleosynthesis is subsequently calculated in a post-processing step using a full set of isotopes. The FRUITY models on the other hand use a full nuclear network that is coupled to the FRANEC stellar evolution code. This method allows the nucleosynthesis calculation to be done along with the stellar evolution, but is more computationally intensive. In-depth descriptions can be found in the above references.

The FRUITY models that we compare with our data are the currently available ones[1]. We especially compare our data to the ones of 1.5 $M_{\odot}$ and 2 $M_{\odot}$ with solar metallicity ($Z_{\odot}$) and 0.7 $Z_{\odot}$. We compare our data as well with the equivalent Torino models, however, in these models we looked at three more parameters. These parameters are the ^{22}Ne(α,n)^{25}Mg reaction rate, the total mass of the ^{13}C-pocket while keeping the hydrogen distribution in the pocket constant, and the mass fraction of ^{13}C while keeping the mass of the pocket fixed. To better understand these parameters, the stellar nucleosynthesis region surrounding the ^{13}C-pocket is shown in Figure 3.1 using a schematic Kippenhahn diagram. Recent reviews are given by Straniero et al. (2008, 2009). In Figure 3.1, time goes schematically from left to right. The vertical axis depicts a small zone inside an AGB star. The bottom of this zone

1. `http://fruity.oa-teramo.inaf.it`

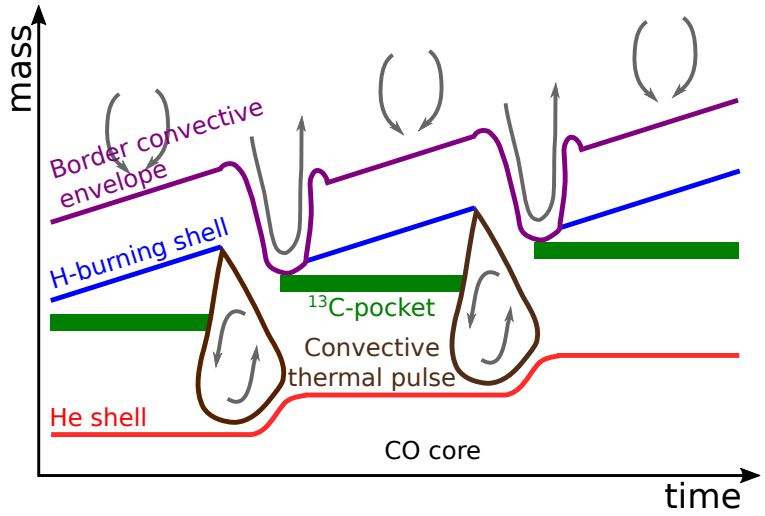

Figure 3.1 Schematic view of the nucleosynthesis region around the ^{13}C-pocket is located in inside a star.

shown as the red line is the helium shell, which borders to the carbon and oxygen rich core. At the top of this mass zone, the purple curve depicts the border to the convective envelope. In between, there is the hydrogen burning shell (blue), the convective thermal pulses (brown) and the ^{13}C-pocket (green). Over time, hydrogen fuses to helium in the intershell, i.e., the shell between the helium shell and the hydrogen burning shell. This raises the pressure and therefore the temperature at the bottom of the intershell. At a given pressure and temperature, a thermonuclear runaway or helium flash ignites the helium shell for a short period of time (a few years), driving a convective thermal pulse. The thermal pulse leads to mixing of the intershell and also drives a mixing event of the top of the intershell with the convective envelope. During this thermal pulse, the temperature in the intershell rises and activates the triple-α process, synthesizing ^{12}C from three ^{4}He nuclei. At the bottom of the convective thermal pulse, the temperature is around $T_8 = 3.5\,\mathrm{K}$ ($T_x = y$ is defined as the temperature $y \times 10^x\,\mathrm{K}$). This is high enough to marginally activate the ^{22}Ne(α,n)^{25}Mg reaction rate, which acts as a neutron source for the s-process. After the thermal pulse, a ^{12}C-rich zone is left behind in the intershell. Mixing of hydrogen from the convective envelope into the intershell results in proton captures of ^{12}C, forming a pocket of ^{13}C. At a temperature

of $T_7 \approx 9$, the ^{13}C(α,n)^{16}O reaction takes place, acting as a neutron source for thousands of years. The two neutron sources differ in neutron density and duration. The ^{13}C(α,n)^{16}O reaction operates at a neutron density of $< 10^7\,\mathrm{n\,cm^{-3}}$, while the ^{22}Ne($\alpha$,n)^{25}Mg reaction operates at a neutron density of around $5 \times 10^9\,\mathrm{n\,cm^{-3}}$. If too many neutrons are present, the ^{13}C-pocket effectively forms ^{14}N, which has a high neutron capture cross section and therefore acts as a neutron poison, effectively limiting the maximum size of the pocket. In addition, hydrogen burning results in leftover ^{14}N on the top of the intershell. If this ^{14}N is mixed into the ^{13}C-pocket, i.e., by stellar rotation, it poisons the neutron source as well. In addition, the ^{22}Ne(α,n)^{25}Mg reaction rate is uncertain at stellar temperatures and is highly dependent on temperature. The standard ^{22}Ne(α,n)^{25}Mg reaction rate is taken from Käppeler et al. (1994). However theoretical constraints (Jaeger et al., 2001; Longland et al., 2012) as well as evidence from presolar SiC measurements (Liu et al., 2014, 2015) indicate, that this standard ^{22}Ne(α,n)^{25}Mg reaction rate can be lower by up to a factor of two. We therefore also consider models with half the standard ^{22}Ne(α,n)^{25}Mg reaction rate. These models are in the following abbreviated as *ne22d2*, where *d2* indicates the division by two. Studies of $\delta(^{138}\mathrm{Ba}/^{136}\mathrm{Ba})$ (Liu et al., 2014) and correlated $\delta(^{88}\mathrm{Sr}/^{86}\mathrm{Sr})$ and $\delta(^{138}\mathrm{Ba}/^{136}\mathrm{Ba})$ (Liu et al., 2015) anomalies in mainstream presolar SiC grains showed that various scenarios for the ^{13}C mass fraction as well as the total mass of the ^{13}C-pocket need to be taken into consideration. Furthermore, a subset of grains from Liu et al. (2014) with $\delta(^{138}\mathrm{Ba}/^{136}\mathrm{Ba}) < -400‰$ could only be explained by changing the shape of the ^{13}C-pocket, i.e., by diluting the pocket and therefore partially poisoning the neutron capture process. However, Liu et al. (2015) concluded that presolar grains requiring these special shapes for the ^{13}C-pocket are rather rare. Here, we compare our measurements with models in which the total mass of the ^{13}C-pocket has been doubled by a factor of two while leaving the hydrogen distribution in the pocket constant. These models are denoted as *pocketx2*, where *x2* stands for the multiplication by a factor of two. For varying the mass fractions of ^{13}C in the pocket, we use the abbreviations *D12*, *D6*, *D3*, *D2*, *D1.5*, and *st*. The *st*

case is the standard case and represents the scenario in which a mixture of 1.5 $M_\odot$ to 3 $M_\odot$ AGB models with half-solar metallicity best reproduce the Solar System *s*-process isotopes (Gallino et al., 1998). The cases denoted by *D* represent cases where the mass fraction of ^{13}C is divided by the given number compared to the standard case (*st*). For example, the case *D2* refers to a ^{13}C abundance in the pocket that is the *st* case abundance divided by two. A detailed description can also be found in Liu et al. (2014, 2015).

While the iron isotopic composition is mainly influenced by the ^{22}Ne(α,n)^{25}Mg reaction rate, some nickel isotopies show large effects depending on the chosen ^{13}C mass fraction. Therefore, this study allows us to roughly test the conclusions of Liu et al. (2014) and Liu et al. (2015), however, neither iron nor nickel isotopes are ideal to draw firm conclusions for AGB star nucleosynthesis. Modeled AGB star anomalies for iron and nickel are small and span a wide range in the carbon-rich pulses. The modeled anomalies for, e.g., strontium and barium on the other side have large anomalies that span a small range. Furthermore, the iron and nickel isotopic signature expected to be significantly influenced by GCE.

3.3.2 Galactic Chemical Evolution Models

Isotopes that are only slightly influenced by the AGB star can be used as proxies for GCE. The best isotope ratios to use are ^{29}Si/^{28}Si, ^{54}Fe/^{56}Fe, and ^{60}Ni/^{58}Ni. For example, in the standard Torino model for a star with 2 $M_\odot$ and solar metallicity, the deviations for the AGB star compared to the Solar System are expected to be +3‰, −5‰, and +18‰ for δ^{29}Si/, δ^{54}Fe, and δ^{60}Ni, respectively. This shows that these isotopes are minimally influenced by the AGB star, hence their composition should represent what went into the star at its birth. A large spread in the silicon isotopic composition has been observed in presolar SiC grains from AGB stars, spanning a total range in δ^{29}Si from approximately −100‰ to +300‰ and in δ^{30}Si from approximately −100‰ to +160‰ (Hynes and Gyngard, 2009). It has been argued (e.g., Alexander and Nittler, 1999; Lugaro et al., 1999; Zinner et al., 2006) that the variability in silicon isotopic composition is due to the GCE in the region where the

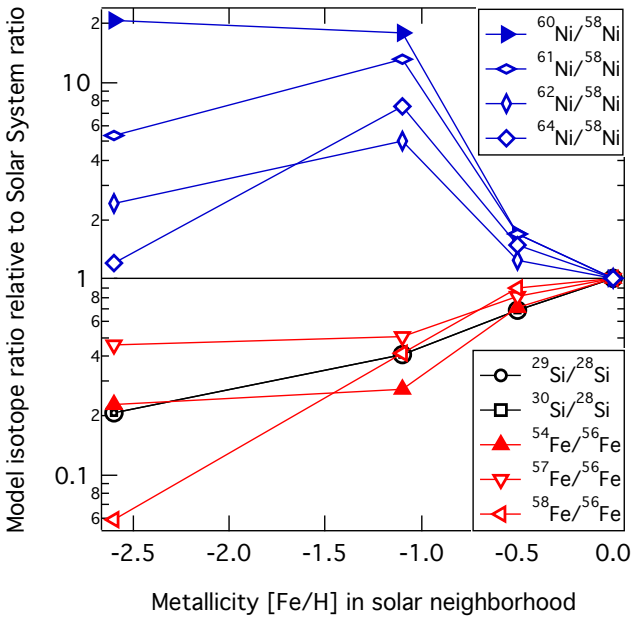

Figure 3.2 Expected GCE spread in the relevant silicon, iron, and nickel isotopes according to the model by Kobayashi et al. (2011). Metallicity [Fe/H] represents logarithmic (base 10) deviations from the solar metallicity and all values are normalized such that the isotope ratios in comparison to the Solar System are unity at [Fe/H]=0.

parent stars of the measured presolar grains have formed – other explanation scenarios were elaborated in the introduction. If this argument is correct, a similar isotopic variation is expected for δ^{54}Fe and an even larger spread is expected for δ^{60}Ni. Figure 3.2 shows the expected isotopic compositions for metallicities between [Fe/H] = −2.5 and solar ([Fe/H]=0) for the GCE predictions of Kobayashi et al. (2011), which are based on their previous models (Kobayashi et al., 2006). The metallicity notation [Fe/H] describes logarithmic (base 10) deviation from the solar metallicity, with iron serving as a proxy for all heavy elements. Note that the isotope ratios at solar metallicity are normalized to the Solar System composition as proposed by Clayton and Timmes (1997). Such a normalization is necessary due to the uncertainties of absolute abundance predictions in the GCE models. The comparison shows that the spread that is seen in δ^{29}Si – if due to GCE – should be positively correlated to δ^{54}Fe and of similar magnitude, as well as negatively correlated to δ^{60}Ni and of even higher magnitude.

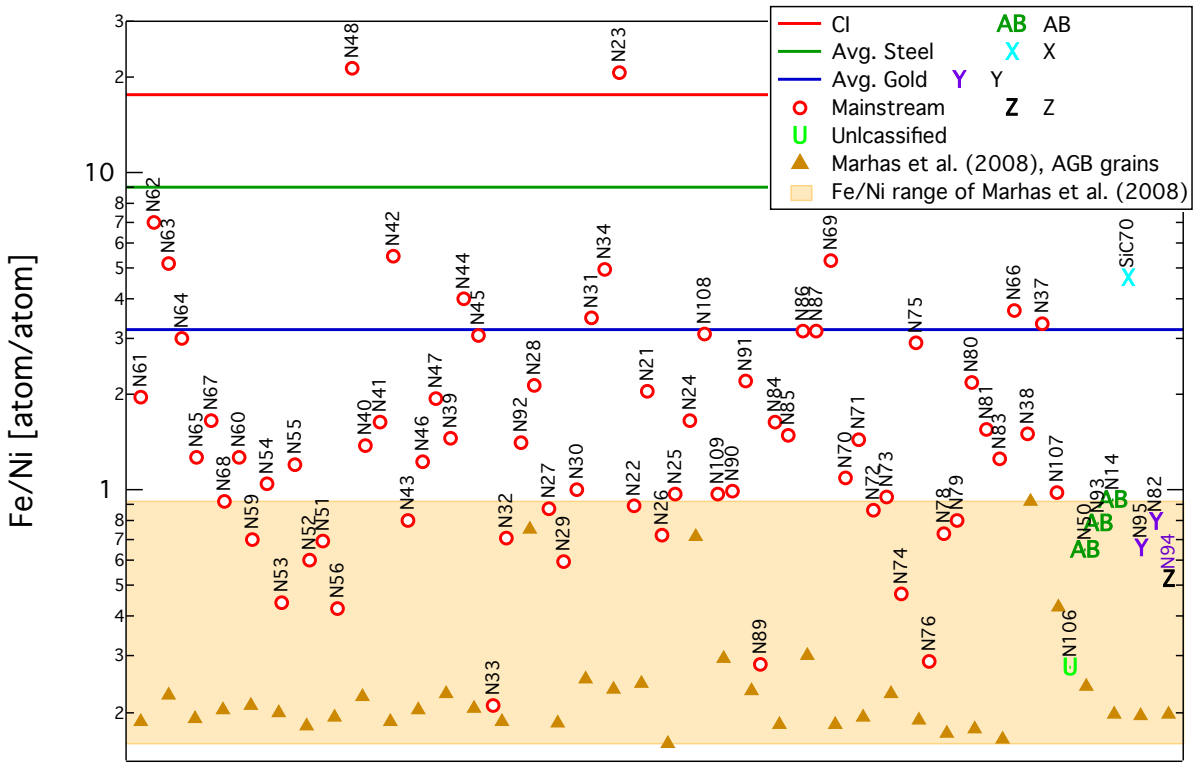

Figure 3.3 Iron-to-nickel atom element ratios in all the measured samples in comparison with the stainless steel used to normalize the elemental ratios, the gold the grains were mounted on, solar composition, as well as literature values by Marhas et al. (2008). The grains are ordered by type.

3.4 Results

3.4.1 Elemental ratios

Figure 3.3 shows the atomic elemental ratios that we measured in all of our presolar grains. The iron-to-nickel ratios span more than two orders of magnitude and are on average higher than the measurements reported by Marhas et al. (2008). One possibility that requires discussion is potential contamination of our presolar SiC grains with material from the host meteorite. This is discussed in Section 3.5.1.

Using the iron and nickel useful yield factors for CHILI determined by Stephan et al. (2016), we determined absolute iron and nickel concentrations for presolar grains with a

recorded size. We assumed an ellipsoidal shape of the grain where two axes were measured using scanning electron microscopy. The third axis was inferred as being identical to the smaller axis. Table 3.1 shows the concentration for each grain. Unfortunately, not all grain sizes were recorded, hence, concentrations could not be calculated for all grains. The concentration calculation assumes that all the iron and nickel isotopes in a given presolar grains have been desorbed in the CHILI measurements, which is not necessarily the case. These concentrations therefore represent lower limits, thus we do not report any uncertainties. Note that all concentrations are given in parts per million by weight (ppmw) in the sample. Iron concentrations range from 1.4 to 306 ppmw with an average of 42 ppmw and a median of 17 ppmw. Nickel concentrations range from 1.5 to 236 ppmw with an average of 7 ppmw and a median of 15 ppmw. The iron concentration seems to be in general slightly higher than the nickel concentration. Concentration values reported by Kashiv (2004) for iron range between 44 and 756 ppmw, the values for nickel between 18 and 774 ppmw. While the upper limit of these concentrations is in very good agreement with our measurements, our results show many lower values for iron and nickel than the ones reported by Kashiv (2004). These results are reasonable since our measurements represent lower limits. In comparison, the iron and nickel concentrations in CI chondrites are much higher, 18.5% wt iron and 1.08% wt nickel (Lodders et al., 2009).

3.4.2 Carbon, silicon, iron, and nickel isotopic measurements

Table 3.1 shows all results of our isotopic measurements including 2σ statistical uncertainties. In Figure 3.4 we compare our results for δ^{57}Fe versus δ^{54}Fe (left) and δ^{62}Ni versus δ^{61}Ni (right) with literature values by Marhas et al. (2008) for SiC grains and with iron isotopic measurements in presolar silicates by Ong and Floss (2015). The uncertainties of the iron measurement with CHILI are about a factor of two smaller than for previous measurements with the CHARISMA instrument and, for iron and nickel, about a factor of four smaller than for the measurements by Marhas et al. (2008) and Ong and Floss (2015). In general, the

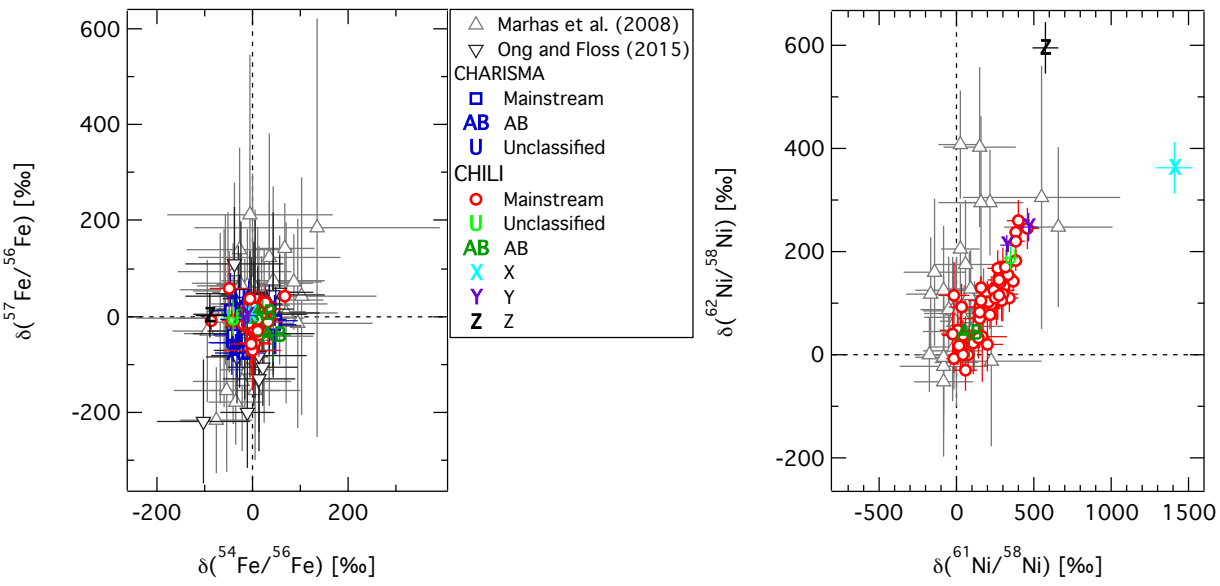

Figure 3.4 Comparison of our results from iron (left) and nickel (right) isotopic measurements with literature values by Marhas et al. (2008). Data measured with CHILI are shown as red circles, data obtained with CHARISMA as blue squares, and data for mainstream SiC grains by Marhas et al. (2008) as gray triangles. Error bars show statistical 2σ uncertainties.

data agree well with each other, however, our study also determined the minor abundances of ^{58}Fe and ^{64}Ni that Marhas et al. (2008) could not measure due to isobaric interferences or low concentrations. Of all the grains analyzed in CHILI, twelve presolar SiC grains showed molecular interference around the ^{64}Ni peak area. This interference most likely originated from TiO and/or other molecular species that were nonresonantly ionized. This interference was detected by the occurrence of small but distinct peaks in between the nickel peaks that were probably nonresonantly ionized by the iron resonance ionization lasers as well as peaks at the respective TiO masses ionized by the nickel lasers. For all mass spectra in which interferences at masses 62 and 64 u were detected, we reject and do not report the measurements of ^{62}Ni and ^{64}Ni. No other interferences were detected that could potentially affect the iron and nickel measurements.

Figure 3.5 shows the silicon isotopic measurements of all presolar SiC grains. Out of the 13 grains that were analyzed with CHARISMA, we found nine mainstream grains, one AB grains, and three grains that did not have enough material left for NanoSIMS analyses, but

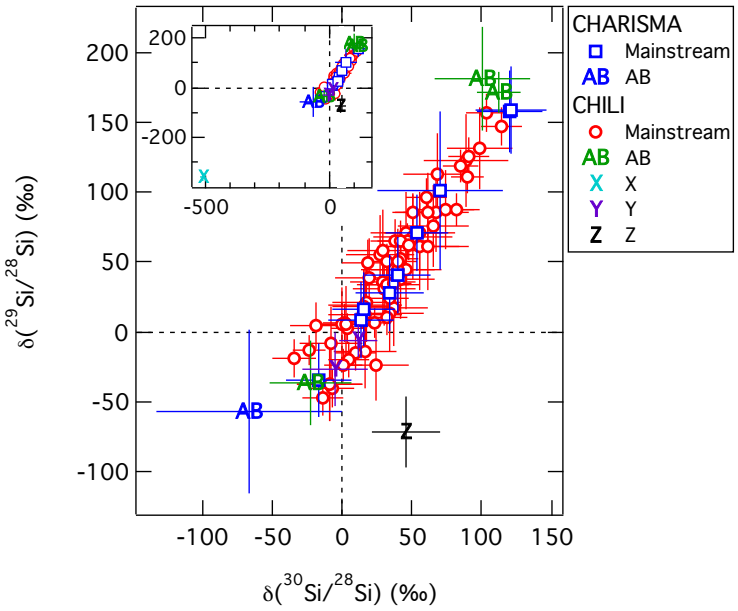

Figure 3.5 Silicon isotopic measurements. The inset figure shows an overview, including the X grain. The measured mainstream grains lie on a perfect SiC mainstream correlation line with a slope of 1.44 ± 0.09.

are most likely mainstream grains. Out of the 74 grains measured on CHILI, we found 67 mainstream grains, one X grain, two Y grains, one Z grain, two AB grains, as well as one grain for which we do not have NanoSIMS data. This grain is subsequently treated as a mainstream grain.

Table 3.1: Carbon, silicon, iron, and nickel isotopic measurements for all presolar SiC grains. Uncertainties are 2σ. Grain numbers starting with the letter A were measured on CHARISMA at Argonne National Laboratory, grain labels starting with N on the CHILI instrument. SiC70 is the X grain. Grains were classified into the usual group, MS for mainstream, X, Y, Z, and AB. Grains that had not enough material left for classification are treated as unclassified (?). Iron and nickel concentrations are given in atom number parts per million normalized to the number of silicon isotopes, whenever presolar grain sizes were recorded.

Grain	Type	$^{12}C/^{13}C$	$\delta^{29}Si$	$\delta^{30}Si$	$\delta^{54}Fe$	$\delta^{57}Fe$	$\delta^{58}Fe$	$\delta^{60}Ni$	$\delta^{61}Ni$	$\delta^{62}Ni$	$\delta^{64}Ni$	Fe/Ni	Fe (ppm)	Ni (ppm)
A8	?				−28±14	40±24	−38±63							
A55	?				−26±22	−60±43	66±93							
A56	MS	17.6±0.3	41±14	40±11	−25±18	−11±27	136±88							
A60	?				−43±24	−40±36	3±170							
A63	MS	55.7±0.8	8±14	13±12	−11±18	−61±30	67±84							
A64	MS	68.7±1.1	−34±13	−17±12	−44±19	13±44	−7±87							
A65	MS	49±0.7	16±13	15±11	−5±16	32±26	−51±70							
A66	MS	64.8±1	28±14	35±12	47±17	−14±32	−30±73							
A68	MS	59±0.9	71±14	54±11	46±18	−17±31	−111±74							
A69	MS	41.6±0.6	158±15	120±12	36±24	−7±43	51±144							
A70	MS	42.6±1.6	159±16	121±13	−39±17	−39±29	37±73							
A73	MS	42.9±1.2	101±28	71±23	0±16	−9±22	29±85							
A75	AB	2.9±0.1	−57±29	−66±28	−77±25	−28±37	−105±116							
N14	AB	3.6±0.1	−36±30	−22±29	−14±18	−1±27	76±87	90±12	309±56			0.929±0.006	7	6
N21	MS	56.3±1.8	58±29	29±26	66±8	43±16	421±47	−25±7	260±38	126±19	817±49	2.059±0.007	220	101
N22	MS	48.1±1.4	30±27	30±22	−87±9	−10±19	280±61	134±8	382±39	237±20	1185±54	0.898±0.003	49	52
N23	MS	47±1.7	61±31	61±29	0±10	−24±15	−25±48	−34±26	4±117	48±67	109±140	20.7±0.3	54	2
N24	MS	101.4±3.4	14±27	34±24	−8±16	5±26	102±81	66±14	270±65	166±35	959±86	1.653±0.011	19	11
N25	MS	49.9±1.6	76±29	66±26	26±15	−7±25	−26±79	−14±10	14±42	13±24	255±50	0.974±0.005	11	10
N26	MS	78.2±2.4	18±27	16±22	5±25	−2±40	69±124	51±14	296±67	170±36	1208±94	0.721±0.006	8	10
N27	MS	81.4±2.6	18±27	37±24	5±10	−9±18	14±53	59±8	277±36	150±19	983±50	0.873±0.003	14	15
N28	MS	81.6±2.8	21±28	18±25	7±10	−20±15	−12±52	69±10	302±48			2.143±0.010	51	21

Table 3.1, continued

Grain	Type	$^{12}C/^{13}C$	$\delta^{29}Si$	$\delta^{30}Si$	$\delta^{54}Fe$	$\delta^{57}Fe$	$\delta^{58}Fe$	$\delta^{60}Ni$	$\delta^{61}Ni$	$\delta^{62}Ni$	$\delta^{64}Ni$	Fe/Ni	Fe (ppm)	Ni (ppm)
N29	MS	64.1±2.3	45±29	40±26	13±28	−5±42	97±137	16±14	219±66			0.594±0.005	14	21
N30	MS	11±0.3	5±27	3±24	−7±23	10±35	93±110	71±16	248±73	130±39	564±86	1.006±0.009	69	65
N31	MS	67.8±2.1	−9±26	−8±23	−19±14	−18±22	33±67	40±18	32±81	93±44	383±92	3.505±0.029	33	9
N32	MS	55.2±1.9	68±31	50±28	13±30	10±47	54±159	−17±16	202±78	103±41	640±96	0.704±0.007		
N33	MS	51.6±1.6	87±29	74±24	35±23	16±35	339±173	−8±8	366±40	144±20	1067±55	0.21±0.001	5	21
N34	MS	41.3±1.3	39±28	19±24	−1±9	−10±14	41±49	−4±13	40±58	38±31	266±65	4.957±0.031	145	28
N37	MS	40.4±1.2	−24±26	25±23	−8±12	−14±20	−44±64	51±15	67±65			3.341±0.023	33	9
N38	MS	93.7±3.1	−37±26	−9±24	10±10	−5±16	−5±63	−4±9	17±45	17±20	197±41	1.502±0.006	15	9
N39	MS	93.7±3.1	−37±26	−9±24	8±11	−11±20	−5±55	−11±9	75±41	−1±22	202±45	1.455±0.007	4	2
N40	MS	88.6±2.6	6±26	0±21	−6±23	8±34	12±103	−7±17	58±76	−29±40	105±78	1.382±0.013	9	6
N41	MS	52.9±1.6	113±29	69±24	−2±12	−5±19	3±63	−26±10	229±48	98±26	599±59	1.632±0.009	17	10
N42	MS	42.8±1.4	123±33	89±30	14±11	5±19	−50±58	−10±16	55±74	35±39	272±81	5.435±0.041	22	4
N43	MS	73.2±2.3	37±28	42±24	−1±17	−6±27	−39±94	52±11	196±47	117±26	749±62	0.801±0.005	136	161
N44	MS	68.2±2.1	36±27	29±23	11±15	−18±23	−54±74	−3±19	−34±78			4.026±0.037	185	41
N45	MS	102.3±3.3	−14±26	16±23	−2±8	−17±14	−21±39	23±10	31±41	18±23	291±48	3.065±0.014	80	25
N46	MS	56.8±1.8	45±29	46±25	−9±10	−2±17	17±57	3±8	44±35			1.227±0.005	3	2
N47	MS	45.3±1.3	85±28	67±23	10±13	−31±20	−47±62	−5±12	−18±51	−9±28	93±55	1.942±0.012	29	14
N48	MS	65±1.9	12±29	17±26	4±10	−12±15	17±48	4±30	180±143			21.3±0.3	108	5
N50	AB	8±0.2	171±14	113±16	41±39	−40±55	−142±172	−96±18	79±83	42±47	259±96	0.65±0.008	12	17
N51	MS	52.4±1.9	61±31	56±29	17±24	18±34	253±120	−10±12	287±59	149±32	798±76	0.689±0.005	7	10
N52	MS	52.8±1.7	71±29	56±25	22±20	−13±30	124±121	16±10	309±50	132±26	903±66	0.6±0.004	3	5
N53	MS	55.3±1.8	71±29	46±25	−15±42	−19±62	161±216	−26±18	260±85	104±45	786±108	0.442±0.006	6	13
N54	MS	61.5±2.1	19±29	17±26	1±34	−8±50	253±172	100±24	264±104	124±56	997±141	1.047±0.013		
N55	MS	46.6±1.4	56±29	27±25	−1±16	−9±24	96±89	13±12	217±54	77±29	649±67	1.205±0.007	2	2
N56	MS	56±1.7	33±27	33±23	13±16	2±25	157±91	19±8	380±40	181±21	946±53	0.425±0.002	9	20
N59	MS	40.7±1.2	131±29	99±24	24±28	−8±42	−92±139	−24±15	273±72	145±38	800±91	0.696±0.006		
N60	MS	52.6±1.2	6±14	2±16	−15±34	−16±52	38±172	−30±24	110±108	23±60	185±120	1.27±0.017		

Table 3.1, continued

Grain	Type	$^{12}C/^{13}C$	$\delta^{29}Si$	$\delta^{30}Si$	$\delta^{54}Fe$	$\delta^{57}Fe$	$\delta^{58}Fe$	$\delta^{60}Ni$	$\delta^{61}Ni$	$\delta^{62}Ni$	$\delta^{64}Ni$	Fe/Ni	Fe (ppm)	Ni (ppm)
N61	MS	17.5±0.3	52±11	42±12	4±33	−55±47	65±152	15±29	24±121	38±69	336±148	1.963±0.029		
N62	MS	49.6±1.1	96±13	60±15	−2±58	−70±84	−18±268	−111±90	−239±336			7.1±0.32		
N63	MS	91.9±2.5	−19±13	−34±15	−45±62	−126±88	−149±273	10±91	−120±571	9±213	310±505	5.18±0.22		
N64	MS	64.1±1.4	3±11	4±12	14±30	−39±45	−73±140	2±33	−8±144			3.016±0.049		
N65	MS	37.8±0.8	156±13	103±14	22±20	17±30	131±101	−55±14	149±69	93±35	457±77	1.268±0.01		
N66	MS	46.4±1.1	−20±13	5±15	10±24	−30±35	73±115	81±31	72±130			3.683±0.051	2	1
N67	MS	63.6±1.6	65±15	38±17	−2±44	−57±63	21±204	−41±35	168±160	35±86	350±188	1.663±0.031		
N68	MS	71.5±1.9	50±16	19±18	16±16	20±25	467±96	−27±10	346±55	109±26	934±67	0.919±0.005	12	12
N69	MS	59.1±1.5	65±15	42±17	1±6	−9±11	−16±30	−2±10	40±48	1±21	95±42	5.300±0.025	30	5
N70	MS	48.6±1.1	125±13	91±14	26±24	30±37	347±136	−4±16	290±77	106±41	611±92	1.09±0.01	63	55
N71	MS	59.9±1.3	50±12	40±14	−2±13	−1±21	51±69	26±11	248±52	109±28	709±66	1.436±0.008	8	5
N72	MS	90.7±1.9	6±11	24±12	−20±18	8±27	117±97	74±12	384±58	219±30	1318±82	0.862±0.006	7	7
N73	MS	55.4±1.3	−48±12	−14±14	−43±22	−9±34	27±169	186±17	460±75	246±39	1208±100	0.949±0.008	9	9
N74	MS	69.5±1.9	4±16	−19±19	−7±11	38±17	290±62	30±6	319±33	169±17	985±45	0.469±0.002	9	18
N75	MS	42.4±0.9	119±12	85±13	−16±23	6±36	34±114	9±25	−14±103	115±64	233±123	2.928±0.037	12	4
N76	MS	42.3±0.9	8±11	16±12	−49±40	57±64	123±239	76±15	399±72	259±39	866±92	0.288±0.003	2	6
N78	MS	65.3±1.4	35±12	37±13	−13±21	−17±32	64±115	14±12	283±57	140±30	858±75	0.727±0.005	4	5
N79	MS	42.1±0.9	147±14	115±15	31±31	−12±46	137±168	−50±17	155±80	105±45	550±100	0.803±0.009	5	6
N80	MS	49.4±1	62±11	48±12	−7±17	−18±26	46±107	3±17	138±74	31±40	348±86	2.176±0.018	6	3
N81	MS	56.8±1.2	87±11	82±12	3±13	−26±19	32±64	37±11	276±52	116±27	892±68	1.551±0.009	11	6
N82	Y	108.5±2.8	−7±12	12±14	−20±12	−6±18	98±60	92±8	324±39	211±21	1244±59	0.794±0.003	35	42
N83	MS	68.6±1.7	11±13	33±15	−10±15	2±23	2±73	33±12	149±51	83±28	428±60	1.251±0.008	30	23
N84	MS	70.4±1.6	24±12	34±14	1±17	−18±26	−42±81	48±15	205±66	103±36	802±88	1.641±0.012	5	3
N85	MS	43.8±0.9	111±11	90±12	22±31	−4±47	123±155	6±24	153±109	69±58	365±124	1.487±0.019	1	1
N86	MS	88.8±2	−13±11	−23±12	8±16	−29±24	41±81	2±18	−25±74	39±43	107±83	3.186±0.028	19	6
N87	MS	59.5±1.3	50±13	33±14	4±19	−13±31	−7±96	−5±22	196±101	19±52	533±121	3.18±0.034	2	1
N89	MS	67.1±1.7	33±14	33±16	4±27	18±41	67±141	46±10	337±49	155±26	1206±69	0.284±0.002	12	40

Table 3.1, continued

Grain	Type	$^{12}C/^{13}C$	$\delta^{29}Si$	$\delta^{30}Si$	$\delta^{54}Fe$	$\delta^{57}Fe$	$\delta^{58}Fe$	$\delta^{60}Ni$	$\delta^{61}Ni$	$\delta^{62}Ni$	$\delta^{64}Ni$	Fe/Ni	Fe (ppm)	Ni (ppm)
N90	MS	52.1±1.2	85±14	51±15	−6±15	−18±24	12±73	5±10	245±48	126±26	713±61	0.994±0.006	21	21
N91	MS	46±1.1	−41±13	−7±16	8±12	−16±21	−36±69	8±12	10±50			2.196±0.013		
N92	MS	53.2±1.6	85±29	62±24	−15±27	−13±41	140±144	19±21	304±100	118±53	749±124	1.413±0.016	3	2
N93	AB	8.3±0.2	181±37	101±34	22±17	6±27	42±94	−108±9	131±43			0.79±0.004	5	6
N94	Z	46.6±1.5	−71±25	46±25	−91±29	2±45	−59±141	1145±28	571±86	595±50	1536±121	0.526±0.005		
N95	Y	117.2±4	−27±26	−5±24	−11±18	2±28	60±107	141±11	468±54	248±29	1447±78	0.656±0.004		
N106	?				−43±24	−5±38	223±125	61±9	349±48	187±24	1245±65	0.277±0.002	8	28
N107	MS	68.1±1.6	−24±12	1±14	−18±10	−2±18	245±57	72±8	276±38	144±19	696±46	0.984±0.004	35	34
N108	MS	96.6±2.5	−15±13	10±15	−10±8	−2±13	0±58	70±10	161±42	131±23	848±57	3.113±0.013	80	24
N109	MS	51.8±1.1	65±12	47±14	20±20	−1±30	59±103	4±13	255±61	112±32	772±76	0.969±0.007	29	28
SiC70	X	923±34.1	−359±17	−513±11	−5±12	5±19	0±70	60±18	1411±120	362±50	1217±120	4.657±0.037	3	1

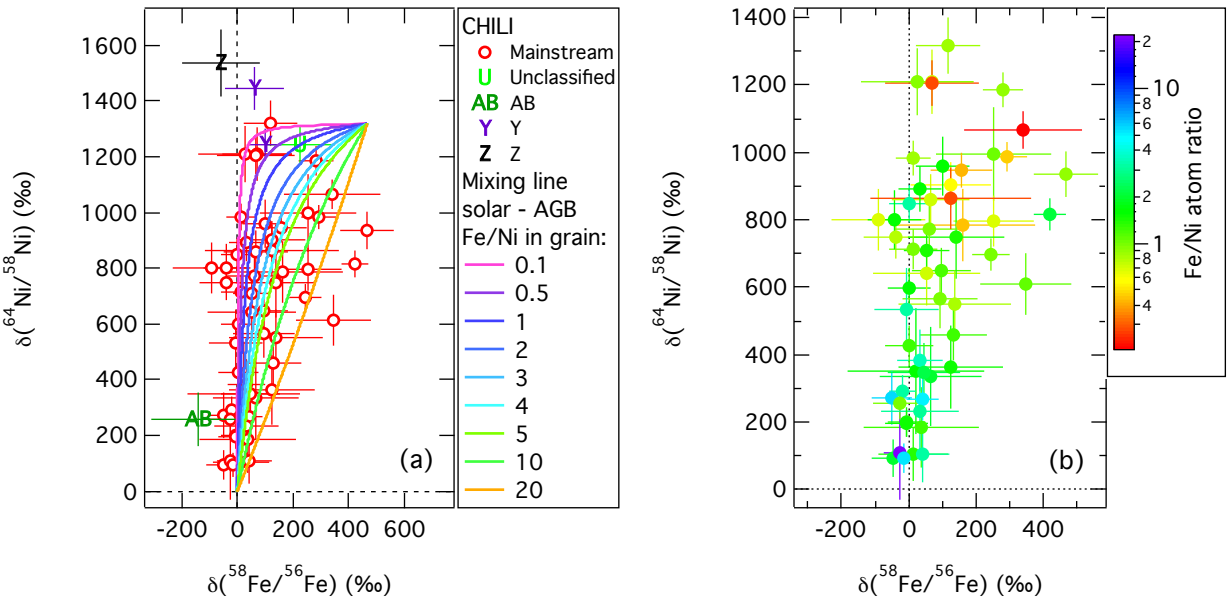

Figure 3.6 (a) Mixing line between a variety of presolar SiC composition and CI. (b) δ^{64}Ni versus δ^{58}Fe isotope anomalies for all measured presolar SiC mainstream grains. The symbol colors are according to the measured iron-to-nickel atom ratio in the grain.

3.5 Discussion

3.5.1 Constraints for presolar SiC grain contamination

The highest isotope anomalies measured in presolar SiC mainstream grains are δ^{58}Fe of 466.5‰ and δ^{64}Ni of 1317.8‰. These measurements are in good agreement with model predictions for AGB stars (see below). However, the isotopic compositions of many grains are closer to the Solar System value, which poses the question if the analyzed grains were significantly contaminated with solar material. We used the CI iron-to-nickel ratio as well as isotopic composition and calculated mixing curves between this solar component and an assumed presolar grain component. For the presolar component, we used the largest values for δ^{58}Fe and δ^{64}Ni measured in presolar SiC mainstream grains. The study by Marhas et al. (2008) showed homogeneous composition in the iron-to-nickel elemental ratio, however, our measurements show a much larger spread in the elemental ratio. Figure 3.6a shows a series of mixing calculations between the Solar System and our assumed presolar grain component.

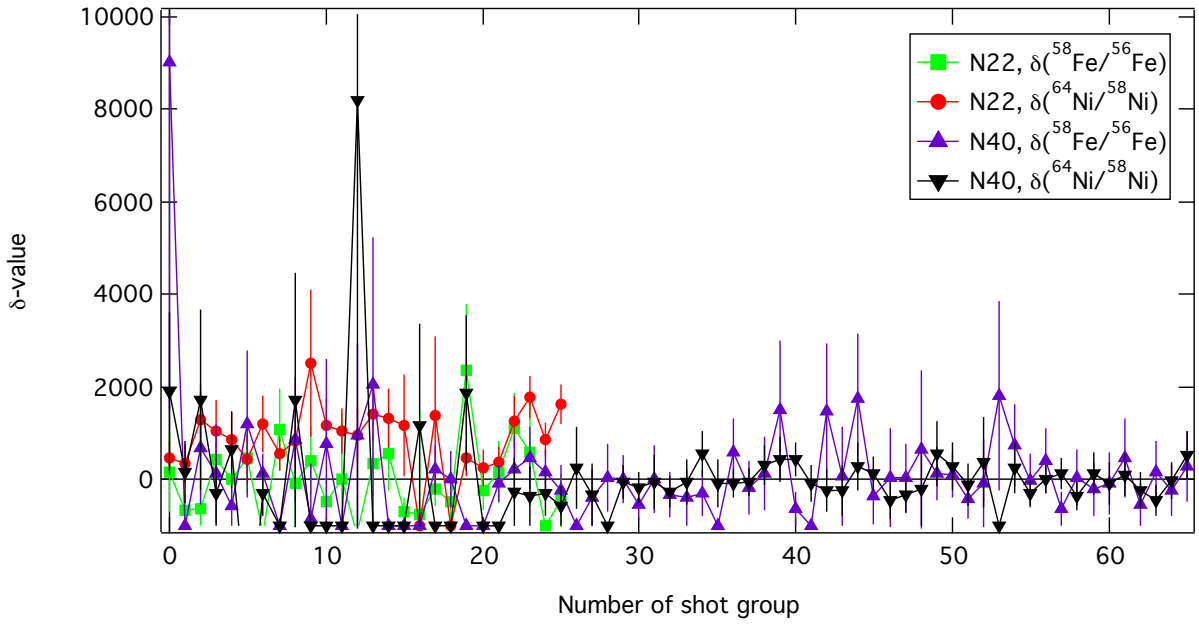

Figure 3.7 Profiles of two presolar SiC grain measurements for δ^{58}Fe and δ^{64}Ni. Grain N22 plots close to the maximum modeled AGB star anomaly while grain N40 plots close to the solar composition.

While AGB star models predict iron-to-nickel ratios that are in the same range as the CI ratio, it is unclear how iron and nickel condense into presolar SiC grains, therefore the initial elemental ratio is not known. We therefore assume various iron and nickel isotopic ratios, from the lowest measured ratios to about the highest measured ratio. Figure 3.6a clearly shows that we cannot exclude contamination of a presolar grain in iron and nickel with Solar System material. Figure 3.6b shows the isotope anomalies in δ^{58}Fe and δ^{64}Ni for the measured SiC mainstream grains color coded according to their measured iron-to-nickel atomic ratio. The figure clearly shows that grains with a higher iron-to-nickel ratio have a tendency to show smaller anomalies in δ^{64}Ni and δ^{58}Fe. This indicates that the presolar grain component as assumed for the mixing line calculation (Figure 3.6a) cannot conclusively exclude contamination with solar material.

Figure 3.7 shows profiles of δ^{58}Fe and δ^{64}Ni for two different presolar SiC grains. Grain N22 shows the isotopic composition that is close to the predicted composition of an AGB star, while grain N40 shows almost solar composition, i.e., no anomalies. The profiles are

bundled into packages of 10000 shots. The figure shows no correlation of package number, which is correlated to time, and isotopic anomaly. Thus we do not see a clear change in the signal from the top to the bottom of the grain.

The isotope anomalies found in this study are compared with literature values by Marhas et al. (2008) in Figure 3.4. While their uncertainties are larger than ours, the isotopic compositions of the measured presolar SiC grains clearly overlap in iron and nickel within error. Our measurements show a slight depletion in δ^{57}Fe for some grains as well as enhancements in δ^{61}Ni and δ^{62}Ni. Both anomalies agree well with Marhas et al. (2008). Contamination therefore cannot be excluded for either data set. Acid cleaning of presolar grains has been shown to remove contamination for barium and strontium (Liu et al., 2014, 2015). For iron and nickel however, acid cleaning does not prevent contamination unambiguously.

3.5.2 Comparison with AGB star models

Origin of the δ^{58}Fe and δ^{64}Ni anomalies. The observed anomalies in δ^{58}Fe and δ^{64}Ni are mostly influenced by the AGB star that formed the presolar grain, i.e., they are dominated by the *s*-process. The *s*-process correlates positively with the number of ^{13}C nuclei within the ^{13}C-pocket and correlates inversely with the abundance of seed nuclei. The abundance of seed nuclei furthermore depends on the metallicity of the AGB star. Lugaro et al. (1999) and Zinner et al. (2006) showed that δ^{29}Si is especially useful as a proxy for the initial metallicity of the AGB star. If the measured isotope anomalies in δ^{58}Fe and δ^{64}Ni depend strongly on the initial metallicity of the AGB star, a strong correlation between these isotope ratios and δ^{29}Si should be found in the data.

Figure 3.8 shows the measured δ^{29}Si isotopic anomalies plotted against the δ^{58}Fe (a) and δ^{64}Ni (b) isotope anomalies that are dominated by the AGB star. The figure clearly shows no correlations, therefore, the AGB star's initial metallicity plays a minor role in explaining the *s*-process dominated elements.

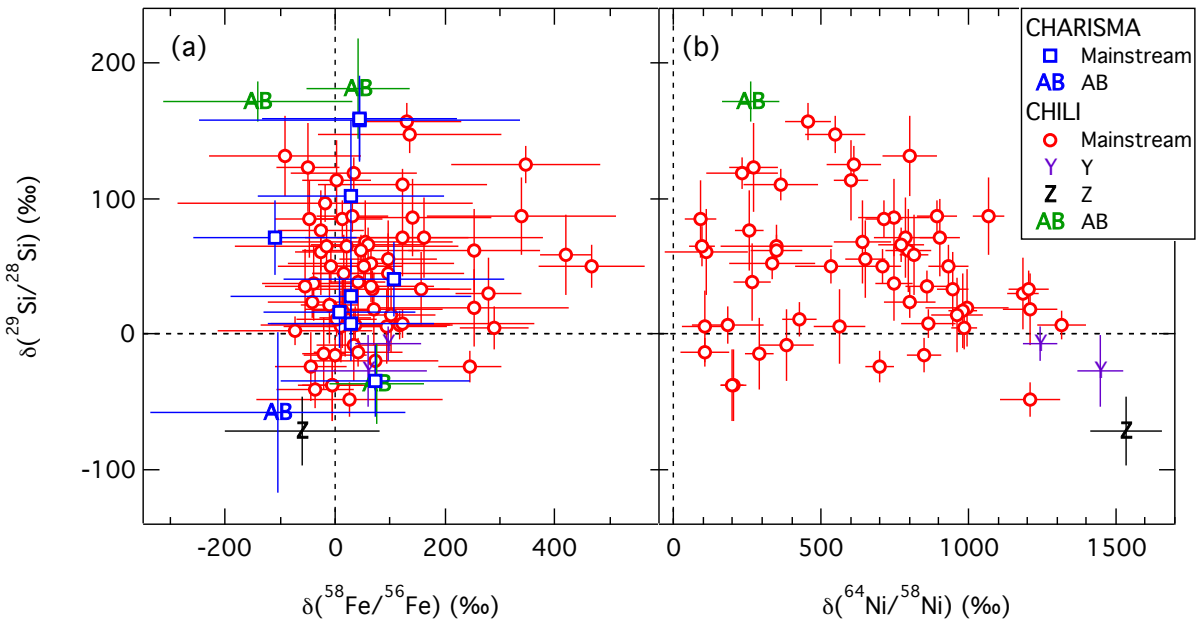

Figure 3.8 Three-isotope plots for δ^{29}Si versus δ^{58}Fe (a) and δ^{64}Ni (b). No correlation between the anomalies in the neutron-rich iron and nickel isotopes with δ^{29}Si can be found, therefore, these anomalies are not the result of varying the initial metallicity of their parent AGB star.

Comparison of measurements with standard Torino and FRUITY models. Figures 3.9 and 3.10 compare our data with the FRUITY as well as the Torino models. We compare here with stellar models of 1.5 and 2 $M_\odot$ with various metallicities. The Torino models for the *st* case ^{13}C-pocket are shown. We plot every thermal pulse of the AGB star in the data as lines and additionally with symbols whenever the carbon-to-oxygen ratio in a given thermal pulse is larger than unity (carbon-rich). If the carbon-to-oxygen ratio in the envelope after a given thermal pulse is smaller than one, all of the carbon is tied up as stable gas-phase CO and no carbon is left to form SiC. Presolar SiC grains can therefore only form when the envelope has a carbon-to-oxygen ratio > 1. The 1.5 $M_\odot$, $Z_\odot$ FRUITY model does not become carbon-rich and is therefore only plotted as a line. The iron isotopic composition measured in presolar SiC grains can be explained by the 1.5 $M_\odot$ Torino model with 0.5 $Z_\odot$, the 2 $M_\odot$ Torino model with $Z_\odot$, as well as by all the plotted FRUITY models except the one noted above that does not become carbon-rich. The 2 $M_\odot$, 0.5 $Z_\odot$ Torino

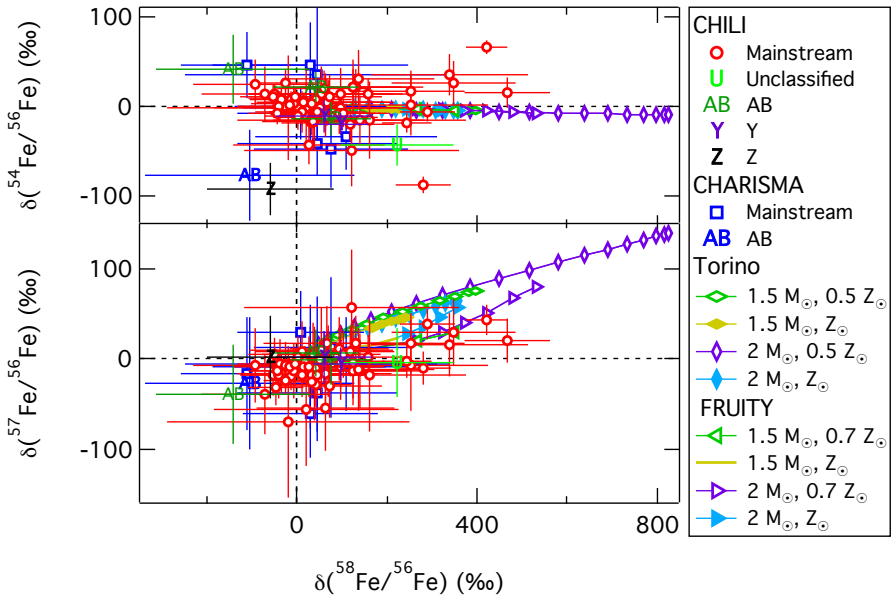

Figure 3.9 Comparison of all iron isotopic measurements with the FRUITY and Torino AGB models. All thermal pulses of the AGB star are plotted, whenever the carbon-to-oxygen ratio in a thermal pulse exceeds unity, we add a symbol at the given pulse.

model overproduces all of the measured iron isotope ratios relative to ^{56}Fe.

The presolar SiC grains from AGB stars show larger anomalies in δ^{64}Ni than in δ^{58}Fe, which is expected from the Torino, but not from the FRUITY models. Figure 3.10 compares our measurements with the models. Here, the picture is quite different from that for the iron isotopic measurements: only the 2 $M_\odot$, 0.5 $Z_\odot$ Torino AGB model predicts high enough anomalies in δ^{64}Ni to agree with our measurements. All other stellar models predict too low δ^{64}Ni. However, this model predicts higher anomalies in δ^{58}Fe than is shown in the data. Contamination with iron, while leaving the nickel content of a presolar SiC grain pristine, could explain the discrepancies between the 2 $M_\odot$, 0.5 $Z_\odot$ Torino AGB model and the iron isotopic measurements, is however unlikely due to the very constant offset between model predictions and measurements.

δ^{58}Fe and δ^{64}Ni as tracers for the ^{22}Ne(α,n)^{25}Mg reaction rate and the ^{13}C-pocket. Figure 3.11 compares our measurements with several special cases of the Torino

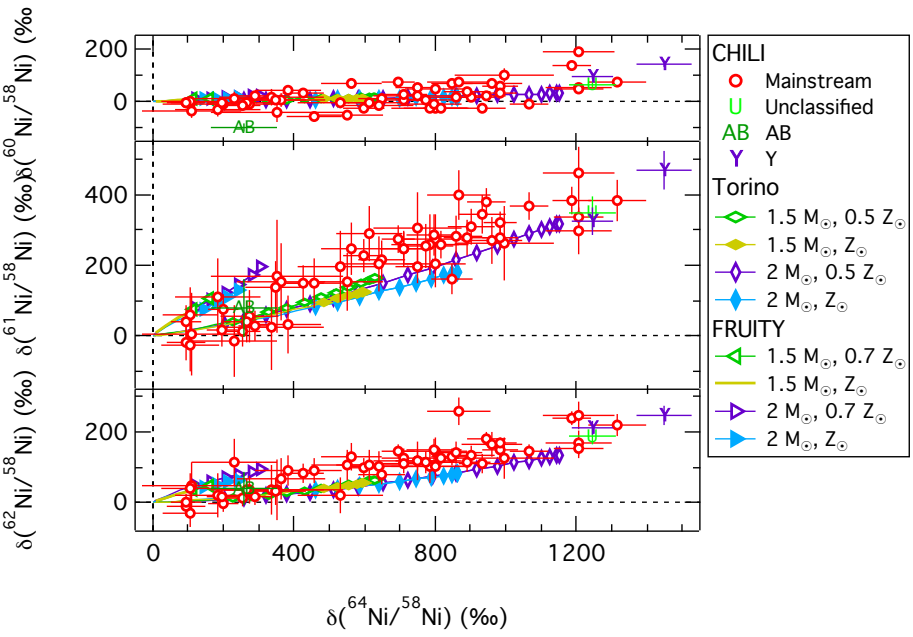

Figure 3.10 Comparison of all nickel isotopic measurements with the FRUITY and Torino AGB models. All thermal pulses of the AGB star are plotted, whenever the carbon-to-oxygen ratio in a thermal pulse exceeds unity, we add a symbol at the given pulse.

model. Here, we focus on δ^{64}Ni versus δ^{58}Fe since these two systems show the largest anomalies in the measurements as well as in the predictions. Figure 3.11a compares our data with the $2\,M_{\odot}$ star for different metallicities and two different cases. The filled symbols show the case in which the ^{22}Ne(α,n)^{25}Mg reaction was divided by a factor of two. The open symbols show the same ^{22}Ne(α,n)^{25}Mg reaction rate, however, in addition the total mass of the ^{13}C pocket has been doubled by a factor of two while leaving the hydrogen distribution in the pocket constant. The pocket size itself in Figure 3.11a is the standard case *st*. The figure clearly shows that δ^{64}Ni is highly sensitive to the ^{13}C mass, however, the predictions for δ^{58}Fe do not depend on it. The model here that best describes the observed isotopic composition is the $2\,M_{\odot}$, $0.5\,Z_{\odot}$ model with half the ^{22}Ne(α,n)^{25}Mg reaction rate. The models with solar metallicity vastly underpredict the δ^{64}Ni values, while the models with $0.3\,Z_{\odot}$ vastly overpredict them.

Figure 3.11b focuses on the $2\,M_{\odot}$, $0.5\,Z_{\odot}$ model, for which the standard ^{22}Ne(α,n)^{25}Mg reaction rate has been divided by a factor of two. Here, we look at different cases with

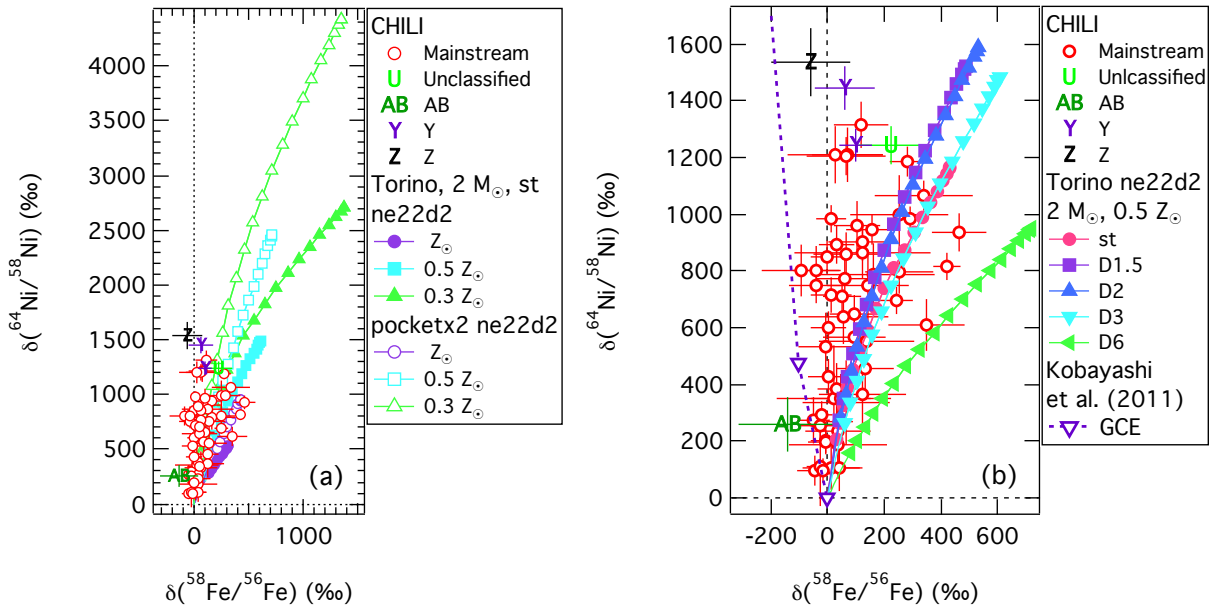

Figure 3.11 Comparison of our measurements with the Torino models for the 2 $M_\odot$ model at different metallicities and various ^{22}Ne(α,n)^{25}Mg reaction rates (a) and the 2 $M_\odot$, 0.5 $Z_\odot$ model with the *ne22d2* model for various ^{13}C pocket cases (b). All thermal pulses of the AGB star are plotted, whenever the carbon-to-oxygen ratio in a thermal pulse exceeds unity, we add a symbol at the given pulse. In the right figure, we added the trend that is expected for GCE (Kobayashi et al., 2011). The plotted symbols here shows the model at a metallicity of [Fe/H] = 0 and −0.5.

variable mass fraction of ^{13}C in the pocket. As shown in the figure, this ^{13}C mass fraction is a good indicator for the nickel isotopic composition. Most presolar grain measurements can be explained by the cases between *st* and *D3*, in fact, these four cases vary only slightly from each other. however, some of the measurements clearly resulted from an AGB star with a lower ^{13}C abundance and can only be explained by invoking the *D6* case. Figure 3.11b also shows the expected GCE trend (Kobayashi et al., 2011). This trend goes into the positive direction for δ^{64}Ni, which is analogous to the AGB models, however, into the negative direction for δ^{58}Fe. Presolar SiC grains that show large anomalies in δ^{64}Ni and only weak anomalies in δ^{58}Fe could therefore either be a mixture between the AGB star contribution and GCE or be contaminated with solar material. Figure 3.2 shows that GCE could explain a shift in δ^{58}Fe of around 200‰ towards the negative. The models that best explain the

observed δ^{58}Fe and δ^{64}Ni isotopic ratios are also the models preferred by Liu et al. (2014, 2015).

Liu et al. (2014) also found that a small fraction of presolar SiC grains had δ^{138}Ba isotopic anomalies < -400‰, which could not be explained in terms of these AGB models. To explain these special grains, they invoked a shallower ^{13}C distribution profile in the ^{13}C-pocket. Such a profile could, for example, be created by stellar rotation. As shown by Piersanti et al. (2013), rotation mixes ^{14}N into the ^{13}C-pocket, which acts as a neutron poison and thus dilutes the ^{13}C-pocket. A comparison with FRUITY models including rotation is discussed below.

Since we cannot exclude contamination of the presolar grain with Solar System material, isotopic anomalies that are closer to the Solar System could be the result of a dilution of the original isotopic composition with the Solar System value. In addition, AGB star models also show a large range of δ^{58}Fe and δ^{64}Ni isotopic composition in the carbon-rich thermal pulses (e.g., Figure 3.11). Most of the measured presolar SiC grains therefore agree well with the chosen models, however, do not constrain them as tightly as the strontium and barium measurements by Liu et al. (2015).

Nickel isotopic anomalies in comparison with the Torino models. The comparison of the measured δ^{64}Ni versus δ^{58}Fe with the Torino models (Figure 3.11) shows that many of the results plot to the side of lower-than-predicted δ^{58}Fe anomaly. If contamination of the measured presolar SiC grains with high iron-to-nickel meteoritic material occurred, such isotope discrepancies are expected. Figure 3.12 therefore compares nickel anomalies with one another. The measurements clearly show an additional enrichment in δ^{61}Ni and δ^{62}Ni compared to the model predictions if we only look at the models down to *D6*, i.e., the models that agree well with δ^{58}Fe and δ^{64}Ni (see Figure 3.11). Contamination with Solar System material can be excluded here, since it would rather pull the isotope ratio towards zero (in δ-units), which is not observed. This shift in the nickel isotopic ratios away from the predicted

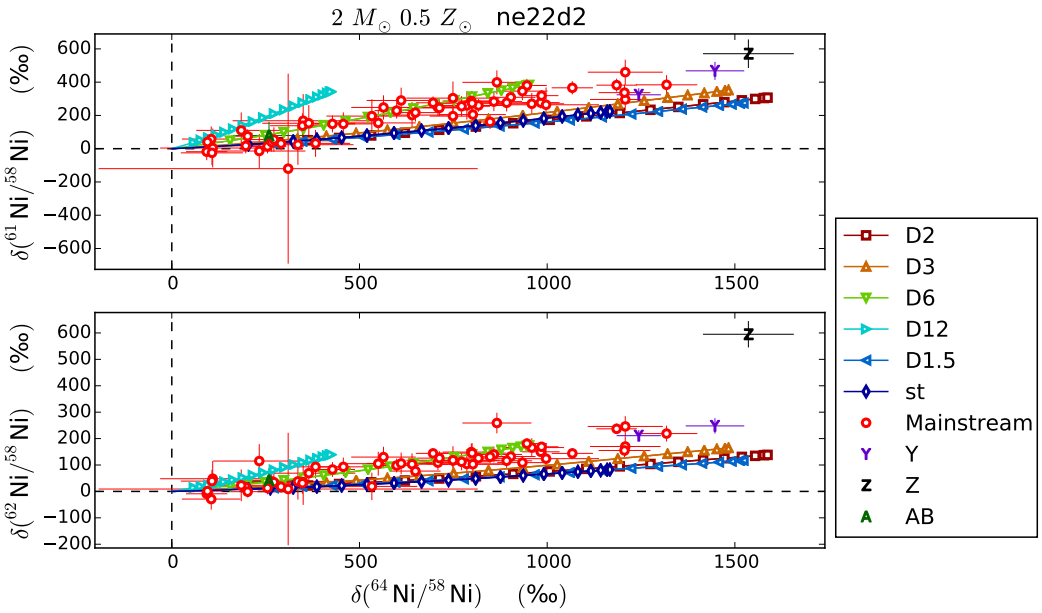

Figure 3.12 Nickel isotope ratios in comparison with the Torino model for the 2 $M_\odot$ star with half solar metallicity in the *ne22d2* case.

anomaly from the AGB star most likely represents GCE. The models by Kobayashi et al. (2011) predict slightly higher shifts in δ^{61}Ni and δ^{62}Ni compared to δ^{64}Ni (see Figure 3.2). In addition, the predicted effects from the shift caused by the AGB star are about a factor of ten higher in δ^{64}Ni than in δ^{61}Ni and δ^{62}Ni. A shift in δ^{64}Ni due to GCE would therefore be negligible in comparison to the shift caused by the AGB star, however, δ^{61}Ni and δ^{62}Ni are clearly GCE-dominated, as seen in Figure 3.12.

In-depth comparison of FRUITY models with measurements. The FRUITY database represents models of a whole grid of stars from 1.3 $M_\odot$ up to 6 $M_\odot$. While the 2 $M_\odot$ star does not reproduce the measured iron and nickel isotopic composition, the only star that reproduces these anomalies is the 6 $M_\odot$ star. Figure 3.13 (left) shows the comparison of the measured data with the 6 $M_\odot$ star at various metallicities. This model predicts isotope anomalies that are in good agreement with the measurements if the AGB star started with an initial metallicities of 0.007, 0.02, and 0.07 $Z_\odot$. It is unlikely that a 6 $M_\odot$ star with such low metallicity contributes most of the measured presolar grains. Gallino et al. (1998)

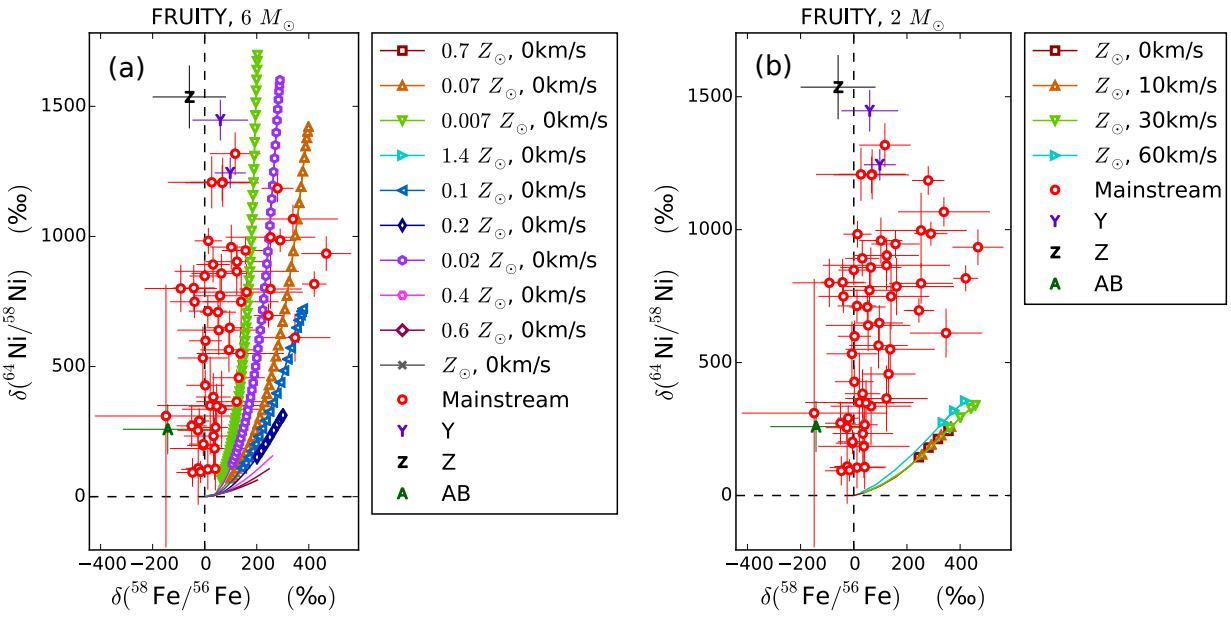

Figure 3.13 (a) Comparison of all measured presolar SiC with the 6 $M_\odot$ FRUITY model for various metallicities. (b) Comparison of the 2 $M_\odot$ model with solar metallicity for various initial rotation velocities included in the model.

showed that the average *s*-process of the Solar System is best reproduced from the output of stars between 1.5 $M_\odot$ and 3 $M_\odot$. In addition, Liu et al. (2014, 2015) showed that their analyzed presolar grains agree fairly well with FRUITY models of 2 $M_\odot$ at 0.5 $Z_\odot$. Also, our measurements agree well with Torino models favored by Liu et al. (2014, 2015). The fact that the FRUITY models for a 6 $M_\odot$ star predicts the isotope anomalies well while the 2 $M_\odot$ models fail in doing so indicates that the input parameters for the ^{13}C-pocket as well as the ^{22}Ne(α,n)^{25}Mg may need to be modified in the FRUITY models. For example, if the temperature at the bottom of the helium intershell is higher than in the FRUITY model, the ^{22}Ne(α,n)^{25}Mg would be more effective and produces higher isotope anomalies. A detailed study is needed to determine which parameters need to be adopted in order to explain the iron and nickel isotope measurements sufficiently.

Figure 3.13b compares the FRUITY model for a 2 $M_\odot$ model with various initial stellar rotation velocities. The rotation mixes ^{14}N into the ^{13}C-pocket and acts as a neutron poison, e.g., diluting the ^{13}C-pocket. The rotation has a slight effect on the predicted anomalies for

δ^{58}Fe as well as for δ^{64}Ni. Rotation improves the situation in both isotopes by about 100‰, however, these models still underpredict the anomalies in δ^{64}Ni. In contrast to the prior findings for barium and strontium isotopic compositions (Liu et al., 2014, 2015), including rotation into the models only shows a minor effect for the isotopic compositions of iron and nickel isotopes.

3.5.3 Origin of the presolar SiC Y, Z, and AB grains

It was argued that presolar SiC Y grains come from low-metallicity stars (Amari et al., 2001b), however, their isotopic composition is in agreement with the presented 0.5 $Z_{\odot}$ models. Presolar AB grains have a more ambiguous origin (Amari et al., 2001b,c), however, their iron and nickel isotopic compositions agree well with the presented AGB star models here.

At the first glance, the presolar SiC Z grain shows iron and nickel isotopic compositions that are in agreement with an origin in an AGB star, however, its δ^{62}Ni anomaly of $+595 \pm 50$‰ is much higher than expected from the AGB star. In addition, the δ^{60}Ni anomaly is $+1145 \pm 28$‰, which cannot be explained by an AGB star either. A lower metallicity star cannot explain the grain either, since the correlated δ^{64}Ni as well as the δ^{58}Fe values would have to be higher. A SN origin of this grain therefore has to be considered, even though the δ^{30}Si is clearly positive.

3.5.4 Origin of the measured presolar SiC X grain

Contrary to observations by Marhas et al. (2008), the measured SiC X grain has normal iron isotopic composition, which makes it difficult to explain all measured isotope ratios using SNe models. Figure 3.14 shows the iron and nickel isotope abundances inside a 15 $M_{\odot}$ SN model (Rauscher et al., 2002), assuming that all the radioactive species have decayed for 4.567 Ga. The green curves show ^{60}Fe and ^{60}Ni 100 a after the model, i.e., around the time when most short-lived radionuclides of interest already decayed, ^{60}Fe however not yet. Certain zones within the SN have more ^{60}Fe than ^{60}Ni at this point and are shaded in green.

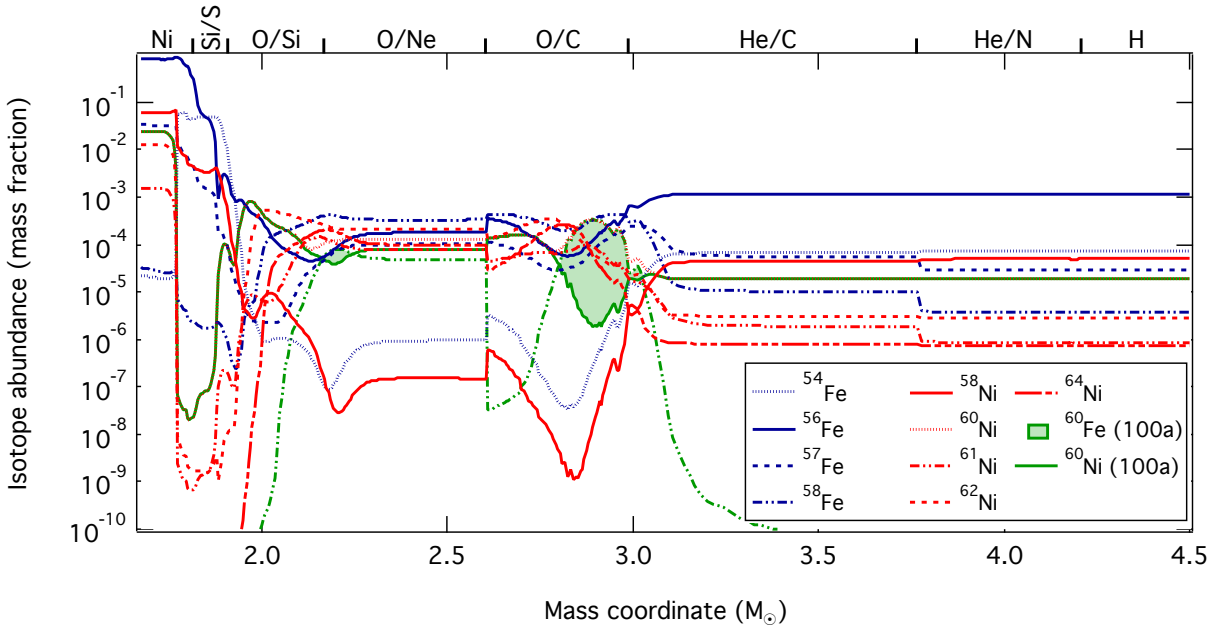

Figure 3.14 Iron and nickel isotope abundances inside the 15 $M_{\odot}$ SN model (Rauscher et al., 2002) assuming that all the radioactive species of interest decayed for 4.567 Ga. The green curves show the ^{60}Fe and ^{60}Ni 100 years after the model ends, i.e., ^{60}Fe has not yet fully decayed and is in certain zones more abundant than ^{60}Ni (green shaded areas).

Also shown are the names of the different zones we used for the following mixing calculation.

Using the 15 $M_{\odot}$ model by Rauscher et al. (2002), we found a mixture that can describe the carbon, silicon, and nickel isotopic composition well, however, does not explain the iron isotopic measurements. Since the iron isotopic composition has no anomalies, contamination of the presolar SiC grain with iron and not with nickel is a likely explanation for the observation. In order to explain the silicon isotopic composition, parts of the Si/S zone must be mixed into the grain. This zone however contains large amounts of ^{54}Fe resulting in a positive δ^{54}Fe anomalies. The measured values along with the predicted values from the SN model are shown in Table 3.2. Also shown is the percentage of the presolar SiC grain that originated in given zone, as well as the carbon-to-oxygen ratio at the time of condensation. The iron isotopic measurements were not used to fit the model to the data. The model predicts well the carbon and silicon isotopic ratios and also shows the correct trends in the nickel isotopic compositions. The result of the SN mixing calculation for δ^{60}Ni is zero, however,

Table 3.2. Presolar SiC X grain (SiC70) in comparison with the 15 $M_\odot$ model by Rauscher et al. (2002). Iron isotopic measurements were not considered when determining the best model mixture to fit the data.

Isotope ratio	Isotope ratio (‰) Measured	SN prediction
Si/S zone		0.22%
O/Ne zone		0.57%
O/C zone		0.1%
He/C zone		62.01%
He/N zone		37.1%
C/O		3.65
$^{12}C/^{13}C$	923 ± 34	901
$\delta^{29}Si$	-359 ± 17	-426
$\delta^{30}Si$	-513 ± 11	-467
$\delta^{54}Fe$	-5 ± 12	*1075*
$\delta^{57}Fe$	5 ± 19	*954*
$\delta^{58}Fe$	0 ± 70	*2953*
$\delta^{60}Ni$	60 ± 18	0
$\delta^{61}Ni$	1411 ± 120	1710
$\delta^{62}Ni$	362 ± 50	576
$\delta^{64}Ni$	1217 ± 120	971

the measurements shows a positive δ^{60}Ni. This could be explained if more iron condenses into the presolar SiC grain compared to the other elements, producing after condensation a positive δ^{60}Ni anomaly due to ^{60}Fe decay. The rest of nickel isotopic measurements fit well with the mixing calculation. The carbon-to-oxygen atom ratio when the grain condensates is 3.65, i.e., it is feasible to condense a SiC grain from such a mixture.

Explaining the measured Z grain qualitatively using the same model is not possible. The silicon isotopic composition with a negative δ^{29}Si and a positive δ^{30}Si are difficult to explain. Explaining the iron and nickel isotopes proves difficult as well. Especially hard to explain in this grain is δ^{54}Fe value of -91 ± 29‰. Adding some material from the Si/S zone to explain the silicon isotopic ratios automatically ends up in predicting positive δ^{54}Fe values. Also the nickel isotopic composition is difficult to explain. We measured > 1000‰ anomalies in

Table 3.3. Presolar SiC Z grain (N94) in comparison with the 15 $M_\odot$ model by Rauscher et al. (2002). For mix 3 and 4, the O/C2 zone is used instead of the whole O/C zone (see text). For all mixtures, the carbon-to-oxygen ratio prior to condensation is 1.0.

Isotope ratio	Measured	Isotope ratio (‰) Mix 1	Mix 2	Mix 3	Mix 4
Si/S zone		0.003%	0%	0.0076%	0%
O/Si zone		0%	0.002%	0%	0.0002%
O/C zone		0.73%	0.58%	0.735%	0.615%
He/C zone		4.687%	3.758%	3.6574%	3.0648%
He/N zone		94.58%	95.66%	95.6%	96.32%
$^{12}C/^{13}C$	46 ± 1.5	58	46	52	44
$\delta^{29}Si$	-71 ± 25	16	30	-5	31
$\delta^{30}Si$	-46 ± 25	50	66	27	61
$\delta^{54}Fe$	-91 ± 29	*4*	-11	*39*	-10
$\delta^{57}Fe$	2 ± 45	*141*	122	*126*	114
$\delta^{58}Fe$	-59 ± 141	*862*	689	*771*	646
$\delta^{60}Ni$	1145 ± 28	60	48	1188	1133
$\delta^{61}Ni$	571 ± 86	590	472	579	493
$\delta^{62}Ni$	595 ± 50	427	339	406	345
$\delta^{64}Ni$	1536 ± 121	964	765	1106	934

δ^{60}Ni and δ^{64}Ni and $\sim +600$‰ anomalies in δ^{61}Ni and δ^{62}Ni. Table 3.3 shows our best mixing calculation for excluding (Mix 1) and including (Mix 2) the iron isotopic constraints from the measurement.

Both mixtures – as the table clearly shows – only poorly fit this Z grain, especially the measured δ^{60}Ni. Figure 3.14 shows that the upper part of the O/C zone has a higher abundance of ^{60}Fe than ^{60}Ni. We split this zone further up into two different zones, trying to better fit the measured δ^{60}Ni, however, this split did not improve the numbers. The only way of producing the observed δ^{60}Ni abundance is by enhancing the iron condensation into the grain with respect to all other elements. Mix 3 and 4 in Table 3.3 show special mixtures, for which we first subdivided the O/C zone into two parts: O/C1 in which the abundance of ^{60}Ni is larger than ^{60}Fe and O/C2 in which the abundance of ^{60}Ni is smaller than ^{60}Fe at

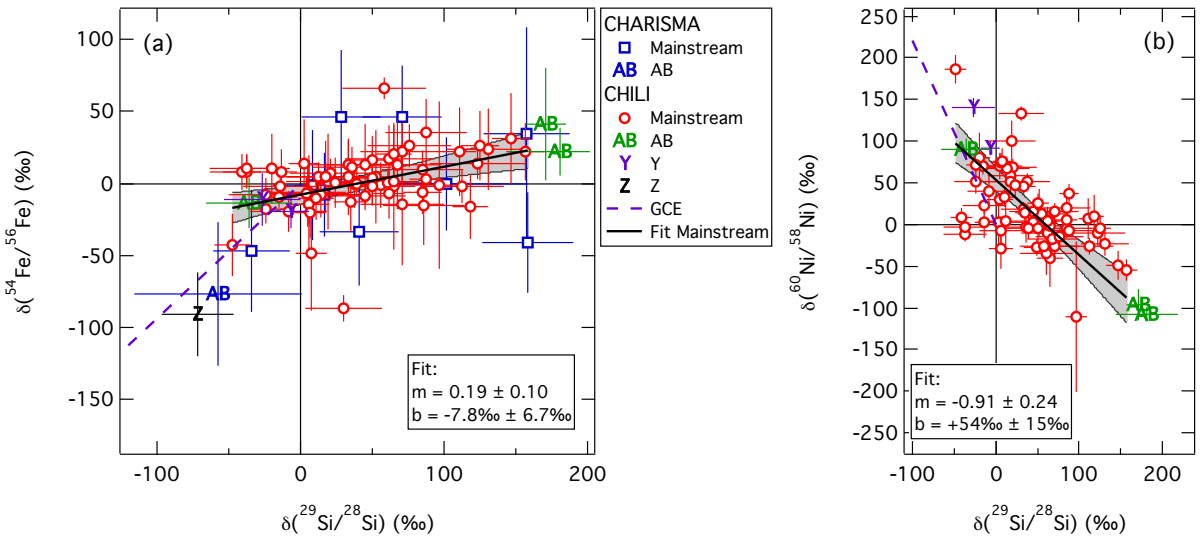

Figure 3.15 Comparison of the GCE-dominated isotope ratios δ^{29}Si with δ^{54}Fe (a) and δ^{60}Ni (b) isotopes with GCE models by Kobayashi et al. (2011). The GCE models are normalized to the Solar System as described in the text. The linear fits are unweighted orthogonal distance regressions of the mainstream grain measurements and the calculated slope is given as m, the y-intercept as b. The gray bands are 95% confidence intervals.

condensation. In addition, we artificially had to enhance the iron condensation by a factor of 25 (Mix 3) and 28 (Mix 4) compared to all other elements in order to optimize the results. This significantly influences the final ^{60}Ni abundance while not influencing any other isotope ratios. These mixtures with an enhanced condensation for iron with respect to nickel show possibilities to explain the composition of the measured Z grain using SNe models. However the negative δ^{54}Fe anomaly is very difficult to explain here.

3.5.5 Implication for GCE of iron and nickel isotopes

Figure 3.15 and 3.16 shows the GCE-dominated isotope ratios δ^{29}Si, δ^{54}Fe, and δ^{60}Ni in correlation with each other as well as in comparison with normalized GCE predictions by Kobayashi et al. (2011). The GCE models shown range in all figures from solar metallicity, which plots at the origin, towards [Fe/H] $= -0.5$ and are for the solar neighborhood. Unweighted linear orthogonal distance regressions were calculated for all mainstream grains.

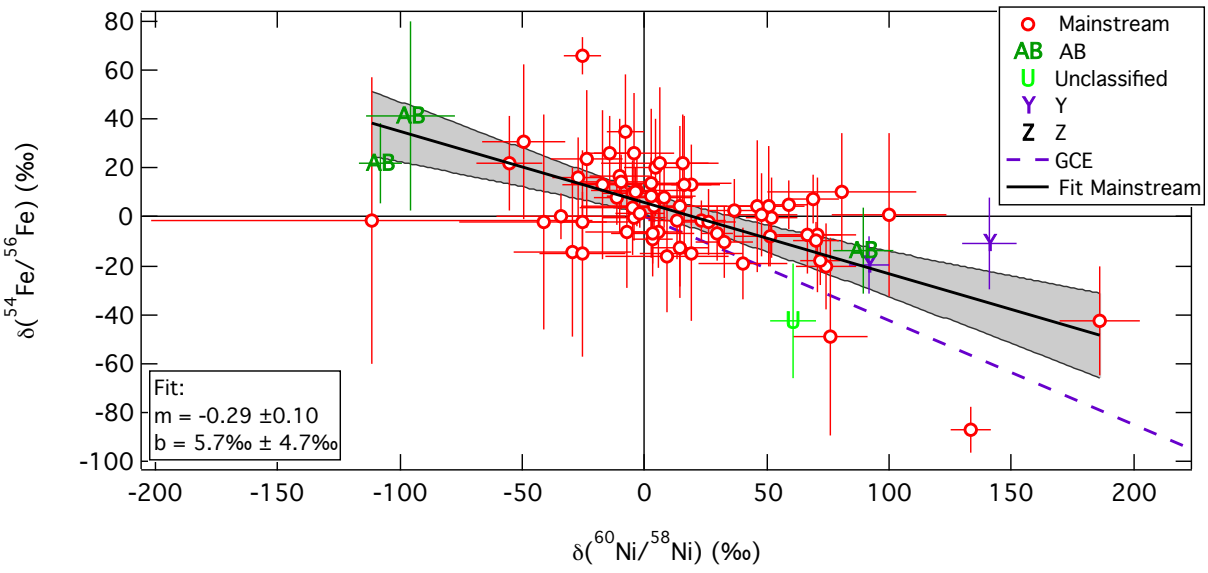

Figure 3.16 Same as Figure 3.15, but for δ^{54}Fe versus δ^{60}Ni.

The measurements show a large scatter, hence the fits show rather trends in the galactic chemical evolution and do not necessarily represent a straight, linear relationship.

The found trends in the measurements are linear, therefore agreeing well with previous findings on GCE for silicon and titanium isotopes (Alexander and Nittler, 1999). While the δ^{54}Fe versus δ^{29}Si correlation has a positive slope (Figure 3.15), the correlations δ^{64}Ni versus δ^{29}Si and δ^{54}Fe versus δ^{64}Ni have negative slopes. This is expected from the GCE models (Kobayashi et al., 2011). While the abundance of neutron-rich isotopes increase in silicon and iron with increasing metallicity, the neutron-rich isotopes of nickel decrease. The data clearly support this finding.

The modeled GCE trends as shown in Figure 3.15 and 3.16 show some differences in δ^{29}Si, however, agree rather well for δ^{54}Fe and δ^{60}Ni. The comparisons show that the trend in δ^{29}Si is too shallow, i.e., that not enough ^{29}Si with regard to ^{28}Si is produced in the SN models used by Kobayashi et al. (2011). The underproduction of ^{29}Si in SN II models is a well known problem. Timmes and Clayton (1996) proposed that the ^{29}Si production should be enhanced by a factor of ~ 1.5. The same enhancement was used in the models by Lugaro et al. (1999) and Nittler (2005) to evaluate heterogeneous GCE in order to explain

the silicon isotopic composition in presolar SiC grains using the SN II models by Woosley and Weaver (1995). If we compare the δ^{29}Si between a 15 $M_{\odot}$, $Z_{\odot}$ SN II model by Woosley and Weaver (1995) with the equivalent model by Kobayashi et al. (2011), we find that their δ-values are -351‰ and -244‰, respectively. The proposed enhancement of a factor of 1.5 in the ^{29}Si production on top of the Woosley and Weaver (1995) models would however result in a δ^{29}Si value of +87‰. This shows that the Kobayashi et al. (2011) SN II models also underproduce ^{29}Si, which explains the mismatch in the trends we see in Figure 3.15.

The orthogonal distance regressions through the presolar SiC mainstream grain data in Figure 3.15 and 3.16 do not go through the Solar System average, however, the plotted data also still include the AGB star contribution to the isotope abundance. Our favored model as described above predicts isotope anomalies of ^{54}Fe = -7‰ and ^{60}Ni = +26‰. In the silicon isotopes, the AGB star models include a nonsolar initial composition. If corrected for this, the total enhancement in δ^{29}Si from the AGB star is +5‰. These enhancements are model-specific, however, they are clearly in the right area to show that our measured GCE trend line does go through the Solar System average composition within uncertainty. This shows that the Solar System is not a special case with regard to its iron and nickel isotopic composition.

One possible scenario to explain the observed silicon isotopic composition was brought forward by Clayton (2003) in form of a galactic merger model. The model assumes that a galaxy colliding with the solar neighborhood triggered the formation of the parent stars that later formed the presolar grains we measure today. This merging galaxy and the solar neighborhood had different metallicities, thus the stars forming from the merged material started with an initial composition that is a mixture between the two. The silicon isotopic composition observed in presolar grains can therefore be explained as being on a mixing line between the solar neighborhood prior to the merger and the merging galaxy. Using our new data, we can test this galactic merger model. First, we need to determine the necessary end member compositions that can explain the measured δ^{29}Si isotopic composition. Let us assume, that

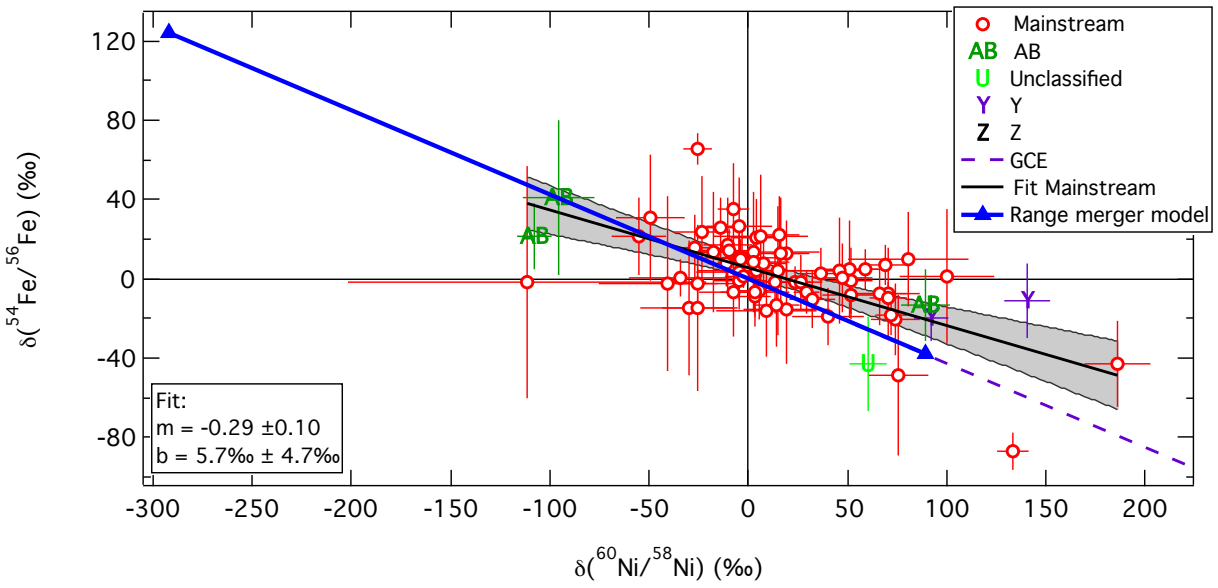

Figure 3.17 Same as Figure 3.16, however, including the predictions from a galactic merger if the range of measured δ^{29}Si isotope ratios is reproduced.

GCE goes along the trend that is predicted by Kobayashi et al. (2011). We already determined, that ^{29}Si is underproduced. In order to fit the trend to the SiC mainstream line, the ^{29}Si production needs to be enhanced by a factor of about 1.2. Furthermore we assume, that the galaxy that collided with the solar neighborhood followed the same GCE trend as the solar neighborhood. We assume this evolution to be linear and that the normalized values from Kobayashi et al. (2011) between [Fe/H] $= -0.5$ and [Fe/H] $= 0$ describe this evolution. Using the minimum and maximum value of δ^{29}Si in all of the measured presolar SiC mainstream grains, we can determine the two mixing end members in terms of metallicity. At the time of the collision, one end member will have contributed material [Fe/H] $= -0.066$ and the other material with [Fe/H] $= +0.22$. Looking at the δ^{54}Fe and δ^{60}Ni isotopes, we can now predict the isotopic range of possible mixtures from such a collision. Figure 3.17 shows the results of this simple mixing calculations. The blue triangles, connected with the blue line, show the possible mixing calculations for such a galactic merger model. All measured presolar SiC mainstream grains should lay in between those two data points and fill out the whole space if the isotopic composition could simply be explained by mixing two galaxies at

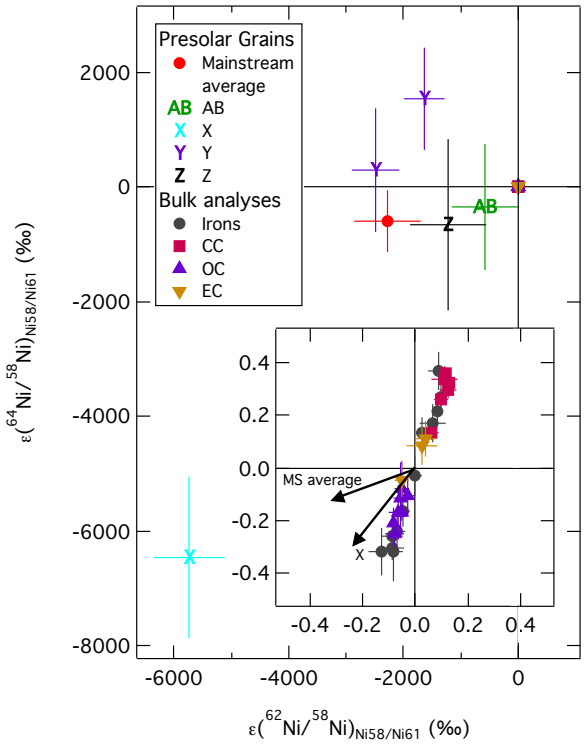

Figure 3.18 Comparison of nickel isotope anomalies in bulk meteorites (Steele et al., 2011, 2012) with the measured presolar grain values.

different stages of their evolution together. As Figure 3.17 clearly shows, the galactic merger model by Clayton (2003) cannot explain the observed data and therefore has to be rejected.

3.5.6 Origin of nickel isotopic anomalies in the Solar System

Steele et al. (2011, 2012) measured nickel isotopic anomalies in bulk iron meteorites and bulk chondrites, respectively. To remove mass dependent fraction from the dataset, these authors normalized the reported isotopic ratios internally to ^{58}Ni and ^{61}Ni. In addition, they give the isotope ratios as ϵ-values, which are parts per 10000 deviations from a given standard, i.e., the numbers are ten times larger than for δ-values, see equation (2.3). Steele et al. (2011, 2012) found that the $\epsilon(^{64}\mathrm{Ni}/^{58}\mathrm{Ni})_{\mathrm{Ni58/Ni61}}$ and $\epsilon(^{62}\mathrm{Ni}/^{58}\mathrm{Ni})_{\mathrm{Ni58/Ni61}}$ isotopic values correlate very well with each other across all meteoritic samples. Figure 3.18 shows these bulk measurements in comparison with the measured presolar grains. Since the anomalies on

the meteoritic bulk scale are heavily diluted, they are shown in the inset of the figure. While Steele et al. (2011) concluded that the isotopic anomalies in iron meteorites are consistent with an origin in type Ia SNe, Steele et al. (2012) concluded that type Ia SNe are not a likely source of the measured nickel anomalies. They explained the isotopic anomalies by type II SNe with contributions from the Si/S zone. Indeed, the observed trend goes from the Solar System composition towards the measured presolar X grain. Furthermore, the presolar X grain that we measured agrees well with an origin in a $15\,M_{\odot}$ SN (Rauscher et al., 2002) and has a 0.22% contribution from the Si/S zone in order to explain the silicon isotopes. Our work therefore agrees with the argument, that the nickel isotopic anomalies of $\epsilon(^{64}\mathrm{Ni}/^{58}\mathrm{Ni})_{\mathrm{Ni58/Ni61}}$ and $\epsilon(^{62}\mathrm{Ni}/^{58}\mathrm{Ni})_{\mathrm{Ni58/Ni61}}$ observed in bulk meteorites (Steele et al., 2011, 2012) are in agreement with a SN origin.

3.6 Conclusions

We measured 74 presolar SiC grains for their firstiron and nickel isotopic composition simultaneously using CHILI at the University of Chicago. In addition, we report the results of a preliminary study (Trappitsch et al., 2012) that measured 13 presolar SiC grains for their iron isotopic composition using the CHARISMA instrument at Argonne National Laboratory. The high selectivity of these RIMS instruments allows us to measure all isotopes simultaneously. By delaying the nickel ionization with respect to the iron ionization, we were able to measure ^{58}Fe and ^{58}Ni simultaneously with no isobaric overlap. Presolar SiC grains were classified by measuring their carbon and silicon isotopic composition with the NanoSIMS at Washington University in St. Louis. Three grains from the study with CHARISMA did not have enough residual material for classification and one grain measured subsequently with CHILI was missed during the NanoSIMS analysis.

The iron and nickel isotope measurements done with CHILI have uncertainties that are about a factor of two smaller than the ones measured with CHARISMA and about a factor of four smaller than previous analysis done with the CAMECA NanoSIMS 50 (Marhas et al.,

2008). This shows the high sensitivity of this new instrument since uncertainties are mostly limited by counting statistics.

We measured iron-to-nickel ratios that are about an order of magnitude higher than those measured by Marhas et al. (2008). It is unlikely that these differences result from contamination with Solar System material as pointed out above. Our isotopic studies, especially for presolar grains in which iron and nickel were measured, can be used to constrain the composition and size of the parent star by looking at the neutron-rich isotopes. The isotopic composition of the measured presolar SiC mainstream, Y, and AB grains for δ^{58}Fe as well as δ^{64}Ni agree best if explained using the Torino model for a star with 2 $M_{\odot}$ star, half solar metallicity, and by dividing the standard ^{22}Ne(α,n)^{25}Mg reaction rate by a factor of two. This is in agreement with the preferred models by Liu et al. (2014, 2015). The neutron-poor isotopes are dominated by GCE and therefore offer valuable proxies to study the trends of GCE in the solar neighborhood. We showed that the GCE models by Kobayashi et al. (2011) agree well with the measured trends for δ^{54}Fe and δ^{60}Ni, however, the measured δ^{29}Si trend does not agree with the model. We suspect that the ^{29}Si is underproduced in the SN models used by Kobayashi et al. (2011). The same was previously reported by Timmes and Clayton (1996) for the SN models by Woosley and Weaver (1995). The found GCE trends agree well with the average Solar System composition showing that the Solar System is not special in iron and nickel. This however means, that the GCE does not evolve linearly with time, i.e., a linear age-metallicity relation cannot be invoked to explain the isotopic composition. In addition, we showed that the measured correlations do not agree with a galactic merger model. Our measurements however are in agreement with the idea of heterogenous GCE (Lugaro et al., 1999; Nittler, 2005).

CHAPTER 4

COSMOGENIC NUCLIDES IN PRESOLAR SIC GRAINS

This chapter is based on: Trappitsch and Leya (2016) Production and recoil loss of cosmogenic nuclides in presolar grains. The Astrophysical Journal 823, 12 (11pp).

4.1 Introduction

Isotopic studies of presolar grains provide valuable information on stellar processes. However, an important question that remains is when these stellar processes happened, i.e., what was the time between condensation of presolar grains and their incorporation into the early Solar System. Conventional radiometric dating is difficult, if not impossible, not only due to the small grain size but predominantly due to the large isotopic abundance anomalies in almost all elements (e.g., Meyer and Zinner, 2006), which makes a reliable determination of initial parent and daughter nuclide abundances impossible. As an alternative, Tang and Anders (1988a,b) proposed to study cosmic ray exposure (CRE) ages of the grains, i.e., the time the grains traveled through the ISM before their incorporation into the early Solar System.

The destruction of dust grains in the ISM is assumed to be be due to interactions with supernova shock waves (e.g., Jones et al., 1994, 1997) with calculated lifetimes of ∼600 Ma for graphite grains and ∼400 Ma for silicate grains (e.g., Jones et al., 1997). The expected lifetimes for SiC are up to ∼1.5 Ga (Bernatowicz et al., 2003). Though the lifetimes are relatively long, they are significantly shorter than the timescale on which stellar dust is replenished. It is therefore possible that some of the grains found in meteorites have their origin in a late stellar event, i.e., a stellar event that occurred shortly before Solar System formation. It has also been speculated that a supernova (e.g., Cameron and Truran, 1977) or AGB star (Foster and Boss, 1996, 1997), might have triggered the formation of the Solar System. To better understand the history of presolar grains, a proper knowledge of their lifetimes is necessary. This can be achieved by determining their CRE ages.

The first study of CRE ages for presolar SiC grains yielded surprisingly low ages in the range ∼10 to ∼130 Ma, with ages increasing with the average grain size (Lewis et al., 1990, 1994). Later, Ott and Begemann (2000) experimentally demonstrated that presolar grains very often lost essentially all of their spallogenic neon due to recoil. They concluded that, *first*, using spallogenic ^{21}Ne for determining CRE ages for presolar grains is difficult and, *second*, that using spallogenic xenon could be more reliable because of lower recoil losses. In subsequent studies, Mohapatra et al. (2001) and Ott et al. (2001), among others, experimentally determined that recoil losses for xenon isotopes are indeed ∼10 times lower than for neon isotopes. They also argued that the production of xenon is less dependent on the galactic cosmic ray (GCR) spectrum, which is also an advantage because the GCR particle spectrum in the ISM is not well known. Based on these studies and by using the xenon data from Lewis et al. (1994), Ott et al. (2005) determined surprisingly low CRE ages of a few tens of Ma for most of the grain size separates, i.e., again considerably shorter lifetimes than expected. Some of the ages were as high as 175 Ma. However the preferred interpretation by Ott et al. (2005) was that ages were short, probably less than 20 Ma. However, interpretation of the data was made difficult due to poorly kown production rates and due to a trapped xenon component. Note that the assumed isotopic composition of the trapped component had a large influence on the determined ages.

Another approach that avoids problems caused by trapped components, which compromises CRE age studies based on noble gases, was used by Gyngard et al. (2009a,b) in their study of the lithium isotopic composition in presolar SiC grains larger than 5 μm. Since indigenous lithium concentrations in SiC are low, a cosmogenic lithium signal in the form of ^{6}Li excesses is detectable in some grains. Note, however, that the noncosmogenic lithium concentration of a typical presolar SiC grain is still about two orders of magnitude higher than the noncosmogenic neon concentration. In contrast to neon, the production rates for lithium isotopes are only a factor of about two higher. However, the advantage of using lithium over the noble gases is that the star itself is unlikely to add any lithium to the

presolar grain. Hence, the isotopic composition of the background lithium can be assumed to be solar. Since ^{6}Li and ^{7}Li are light isotopes, recoil effects are again significant and must be corrected for. Doing so, Gyngard et al. (2009a,b) obtained exposure ages in the range of ∼40 Ma to ∼1 Ga, i.e., more in accordance with theoretical expectations of interstellar grain lifetimes. By using spallogenic helium and neon, and by focusing on large presolar SiC grains, i.e., grains larger than 2 μm in diameter with mostly moderate recoil effects, Heck et al. (2008, 2009) determined CRE ages ranging from less than 3 to 1100 Ma; the majority of the grains had CRE in the range of a few tens of Ma up to 200 Ma. Using the same dataset but improving the correction for recoil losses, Ott et al. (2009) obtained ages that ranged from 0 to ∼850 Ma; the majority of the grains had ages less than ∼200 Ma.

To summarize, CRE age studies of presolar grains are compromised by a number of problems. *First*, by studying spallogenic neon, the excess ^{21}Ne needs to be distinguished from the background neon, which is inherited from the helium shell of the AGB star. As the neon composition of the helium shell in AGB stars ∼5 Ga ago can be modeled but is somewhat parameter-dependent, the CRE ages for presolar grains are also model-dependent and should therefore be considered as *model ages*. Similarly, the helium and lithium concentrations must also be corrected for a trapped component, which is again dependent on the model used. CRE ages determined in this way are thus also *model ages*. *Second*, the flux and spectral density of GCRs in the ISM ∼5 Ga ago are not known and must be assumed. *Third*, and most importantly, since presolar grains are small, recoil of cosmogenic nuclides is important and must be corrected for. Here we focus on the last two points. Considering the second problem, we improve the modeling for the production rates and the recoil calculations by using a GCR particle spectrum for the current ISM that is fully consistent with recent Voyager data (Stone et al., 2013). Considering the recoil loss calculations, all studies so far corrected for recoil losses in a relatively crude way by either using experimentally determined (constant) recoil ranges from irradiation experiments, and/or the recoil losses were calculated using simplified nuclear modeling. For example, Heck et al. (2008, 2009) used a fixed recoil range of 2.5 μm

for ^{21}Ne in SiC. As mentioned above, Ott et al. (2009) improved the interpretation of the same data by using calculated ^{21}Ne recoil distributions. For modeling, however, they only considered ^{21}Ne production from silicon at a projectile energy of 200 MeV, and the recoil ranges for ^{3}He were roughly estimated from measured momentum distributions. In SiC grains, however, cosmogenic nuclides are produced and recoil is induced by a full spectrum of projectiles. Consequently, the recoil correction itself depends on the particle spectrum in the ISM, and – to be fully consistent – the production rates must be calculated using the same GCR spectrum that is used for calculating recoil ranges.

4.2 Cosmogenic Production Rates

4.2.1 Galactic cosmic ray spectrum

Presolar grains in the ISM are irradiated by GCR particles and cosmogenic nuclides are produced. The production rates can be calculated if the GCR particle spectrum and the excitation functions for all relevant projectile types are known. For the GCR particle, one can use the spectral shape given by Castagnoli and Lal (1980):

$$J_{\mathrm{GCR}}(E, M, c_p) = \frac{c_p E(E + 2m_p c^2)(E + x + M)^{-2.65}}{(E + M)(E + 2m_p c^2 + M)} \tag{4.1}$$

The following discussion is focused on GCR protons because (*i*) they represent the major particle type, (*ii*) most production rates are dominated by proton-induced reactions, and (*iii*) the discussion can easily be adapted to other projectile types if the energy is taken in terms of energy per nucleon. In equation (4.1), J_{GCR} is the flux density of protons of energy E as a function of M and c_p. The total particle flux is c_p, the rest mass of the proton is m_p, c is the speed of light, and x is a factor defined as $x = 780 \times \exp(-2.5 \times E \times 10^{-4})$. The parameter M is the solar modulation parameter of the GCR spectrum, which is essentially the lowest energy a GCR particle must have to travel all the way from the ISM towards the

Sun. An often used average for the last few million years is $M = 550\,\mathrm{MeV}$ (e.g., Leya and Masarik, 2009). The best estimate for the integral number of GCR particles in the asteroid belt in the last few million years is $4.47\,\mathrm{cm^{-2}\,s^{-1}}$ (at $M = 550\,\mathrm{MeV}$; Leya and Masarik, 2009).

Presolar grains, however, were irradiated by a GCR spectrum that was (most likely) not modulated by stellar magnetic fields and therefore had a different spectral shape and a higher integral particle flux. Recent Voyager data show that the shape of the current GCR spectrum in the interstellar medium, i.e., outside the influence of the solar magnetic field, can be described by equation (4.1) when choosing $M = 0\,\mathrm{MeV}$. While Overholt and Melott (2013) suggest a very low modulation, the spectral form given by Stone et al. (2013) is best described by a modulation $M = 0\,\mathrm{MeV}$. Integrating the measured GCR spectrum outside the Solar System (Stone et al., 2013) gives a total particle flux of $17.3\,\mathrm{cm^{-2}\,s^{-1}}$ and a composition of 93% protons and 7% α particles. These data are consistent with the best estimate for the asteroid belt, i.e., for the spectrum within the Solar System. For example, a value of $4.47\,\mathrm{cm^{-2}\,s^{-1}}$ for $M = 550\,\mathrm{MeV}$ corresponds to $\sim 20.8\,\mathrm{cm^{-2}\,s^{-1}}$ for $M = 0\,\mathrm{MeV}$, i.e., for outside the Solar System. The GCR composition within the Solar System is 87% protons, 12% α particles, and 1% heavier nuclei (Simpson, 1983). We can conclude that the integral flux of the current GCR spectrum outside the Solar System (Stone et al., 2013) is in very good agreement with the few million year average of the integral GCR flux inside the Solar System.

4.2.2 Cosmogenic production rates

All production rate and recoil losses were calculated using the GCR spectrum given by equation (4.1) and using $M = 0\,\mathrm{MeV}$. For modeling, we used $J_p = 16.1\,\mathrm{cm^{-2}\,s^{-1}}$ (=17.3×0.93) and an α particle fluence of $J_\alpha = 1.2\,\mathrm{cm^{-2}\,s^{-1}}$ (=17.3×0.07), i.e., consistent with the data given by Stone et al. (2013). The production rate P_j of a cosmogenic nuclide j is calculated

via:

$$P_j(M) = \sum_{i=1}^{N} c_i \frac{N_A}{A_i} \sum_k \int_0^\infty \sigma_{j,i,k}(E) J_k(E, M, c_k) dE \tag{4.2}$$

Here c_i is the concentration for one out of N target elements from which the cosmogenic nuclide j can be produced, A_i is the molar mass of target element i, and N_A is Avogadro's number. As reaction particle types (denoted by k), we consider protons and α particles. The excitation function for the production of product j from target element i induced by projectile type k is given by $\sigma_{j,i,k}$. Since presolar grains have typically sizes smaller than $1\,\mu$m and even the large (atypical) grains we are interested in here have sizes in the range of few tens of μm, we assume homogenous production of cosmogenic nuclides in the grain, i.e., stopping and absorption of projectiles is not included in the calculations. In addition, we assume that all secondary particles leave the grain before inducing further nuclear reactions.

Here we report production rates for proton- and α-induced reactions. For most of the proton-induced reactions we can rely on experimental data. Note, most of the proton-induced cross sections have been used before to calculate cosmogenic production rates in various types of meteorites and micrometeorites, see, e.g., Ammon et al. (2009), Leya and Masarik (2009), and Trappitsch and Leya (2013). The cross section database for α-induced reactions is rather scarce. Here we use the database recently compiled by Trappitsch and Leya (2013), which has been calculated using the nuclear model codes TALYS-1.2 (Koning et al., 2008) for projectile energies up to 240 MeV and INCL4.5/ABLA07 (Boudard et al., 2002) for higher projectile energies. The TALYS-1.2 code (Koning et al., 2008) is based on the optical model to describe nuclear physics and is currently one of the best codes available for incident particle energies up to 240 MeV (Broeders et al., 2006). For higher energies, Monte Carlo codes like INCL4.5/ABLA07 (Boudard et al., 2002) can be used. INCL4.5/ABLA07 is actually part of the MCNP (Briesmeister, 1993) code collection, which is used and tested for many applications in cosmochemistry (see, e.g., Masarik and Reedy, 1994). Here, we used these codes to extend the cross section database for the proton-induced production of ^{3}He from $^{\mathrm{nat}}$C, ^{6,7}Li from $^{\mathrm{nat}}$C and $^{\mathrm{nat}}$Si, and to the α-induced production of ^{6,7}Li from

^{nat}C and ^{nat}Si (see below). Here, ^{nat}X represents the natural (Solar System) abundance of isotope X.

4.2.3 Cross sections for proton-induced reactions

^{nat}C$(p, X)^3$He. We used the TALYS-1.2 code (Koning et al., 2008) to calculate the cross sections up to an incident proton energy of 240 MeV. In addition we used the experimental data from Kruger and Heymann (1973) at 600 MeV and 3 GeV. The TALYS-1.2 calculation shows two local maxima in the ranges 19 – 22 MeV and 46 – 190 MeV. Since such structures, which typically indicate special evaporation channels, are unphysical and most likely due to computational artifacts, these regions were not considered any further. We instead constructed the excitation function by logarithmically interpolating the regions above and below each maximum. In addition, we increased the thus modified TALYS results by a factor of 2.6 to obtain a smooth transition between modeled and measured cross sections (Kruger and Heymann, 1973). Finally, we extended the excitation function to 10 GeV by logarithmic extrapolation; the thus determined cross section at 10 GeV is 43 mb. Note that INCL4.5/ABLA07 (Boudard et al., 2002) is unable to calculate cross sections for this reaction.

^{nat}C$(p, X)^{6,7}$Li. We used the TALYS-1.2 code (Koning et al., 2008) only for calculating threshold energies; the shape of the excitation functions were calculated using INCL4.5/ABLA07 (Boudard et al., 2002). In addition, some experimental cross sections for the production of ^{6,7}Li from ^{12}C exist in the literature (Davids et al., 1970; Raisbeck et al., 1972). We start the discussion with the excitation functions for the production of ^{6,7}Li from ^{12}C.

The threshold energies calculated using TALYS-1.2 for both reactions are in good agreement with experimental data (Davids et al., 1970) and can therefore be used for the compilation. In the energy range 28 – 44 MeV, we rely on the experimental data (Davids et al.,

1970). At higher energies, there are measured cross sections at 150 and 600 MeV (Raisbeck et al., 1972). For the compilation, only the cross section at 150 MeV is used; in the energy range 0.3 – 10 GeV, the excitation function is based on INCL4.5/ABLA07 results. Since the cross sections for both reactions at 600 MeV predicted by the code are lower than the experimental data (Raisbeck et al., 1972), we increased the modeled excitation functions for the production of ^{6}Li and ^{7}Li from ^{12}C by factors of 4.1 and 1.4, respectively, for a smooth transition between measured and modeled cross sections.

No experimental data are available for the production of ^{6,7}Li from ^{13}C. The threshold energies were again calculated using TALYS-1.2, and the shape of the excitation functions were calculated using INCL4.5/ABLA07. To be consistent with the production of ^{6,7}Li from ^{12}C (see above), we also increased the INCL4.5/ABLA07 results for the production of ^{6}Li and ^{7}Li from ^{13}C by factors of 4.1 and 1.4, respectively. The excitation functions for the production of ^{6,7}Li from ^{nat}C were calculated assuming a composition of carbon of 98.93% ^{12}C and 1.07% ^{13}C. Figure 4.1 (left panel) shows the compiled excitation functions together with experimental data.

$^{\mathrm{nat}}$Si$(p, X)^{6,7}$Li. We used INCL4.5/ABLA07 (Boudard et al., 2002) to calculate the excitation functions for the production of ^{6,7}Li from ^{nat}Si. TALYS-1.2 could not be used because it cannot be applied for large mass differences between target and products. Since INCL4.5/ABLA07 is not always reliable for the production of very light product nuclides, we tested the predictions on the very similar reaction ^{nat}Si(p,X)^{7}Be. Based on the experimental data at 1.2 GeV (Michel et al., 1995) and 1.6 GeV (Michel et al., 1995; Leya, 1997), it can be concluded that the model predictions must be downscaled by an average factor of 1.5 to match the data. Because of the similar reaction mechanism, we adjusted the modeled cross sections for the production of ^{6,7}Li from ^{nat}Si by the same factor of 1.5.

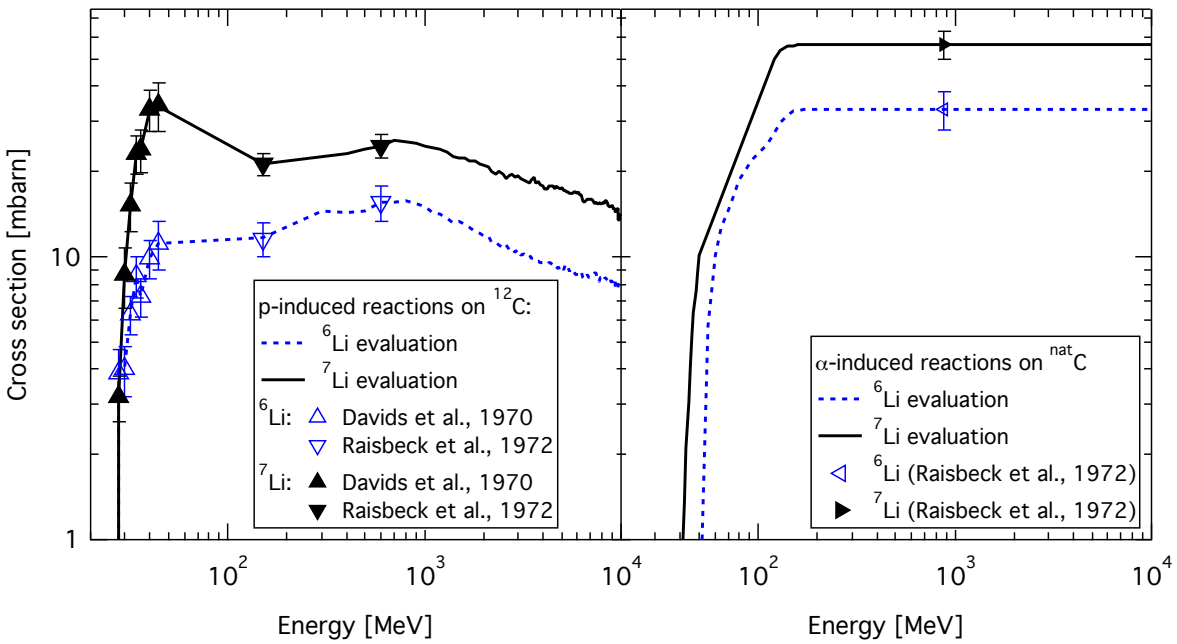

Figure 4.1 Evaluated excitation functions for the reactions ^{nat}C(p,X)^{6,7}Li (left panel) and ^{nat}C(α,X)^{6,7}Li. Also shown are experimental data. Proton-induced cross sections can be calculated up to 10 GeV (left panel), which is however not the case for α-induced cross sections. These are therefore assumed to be constant from 240 MeV to 10 GeV, i.e., the region in which calculations are not possible, going through the measured data points by Raisbeck et al. (1972).

4.2.4 Cross sections for α-induced reactions

In contrast to the proton-induced reactions, few α-induced reaction rates have been measured, which limits checks on the quality of the calculated cross sections. For the production of helium and neon from carbon and silicon, we used the same approach as Trappitsch and Leya (2013), i.e., we calculated cross sections up to 240 MeV using the TALYS-1.2 code and assumed constant cross sections up to 10 GeV. The calculated proton-induced reaction rates decrease by a factor of two to three between $\sim$ 1 GeV up to 10 GeV. Since these energies cannot be calculated for α-induced reactions, it is unclear if this happens as well. However, the GCR fluxes at these energies are significantly smaller, such that these differences have only a minor effect on the total production of a given cosmogenic nuclide. Furthermore, α-induced production rates are in general of less importance, due to the low abundance of

α-particles in the GCR spectrum.

$^{\mathrm{nat}}$C$(\alpha, X)^{6,7}$Li. As mentioned above, INCL4.5/ABLA07 cannot be used to calculate excitation functions for p- or α-induced reactions on ^{12}C. We therefore used TALYS-1.2 to calculate cross sections up to 240 MeV. However, because the calculated cross sections drop sharply at $E > 170$ MeV, which we consider to be a numerical artifact, those predictions were not considered any further. In addition, the calculated excitation function for the production of ^{7}Li shows a local maximum in the range 55 – 110 MeV, which is not expected from nuclear reaction systematics and which we therefore replaced by a logarithmic interpolation between areas at lower and higher energies. The modeled excitation functions were then extended with experimental data at 880 MeV (Raisbeck et al., 1972) and assuming constant cross sections in the range 880 MeV – 10 GeV (left panel in Figure 4.1) using a simple double logarithmic interpolation.

$^{\mathrm{nat}}$Si$(\alpha, X)^{6,7}$Li. As mentioned above, TALYS-1.2 cannot be applied to reactions with large target-product mass differences. In addition, INCL4.5/ABLA07 predictions for α-induced reactions are unreliable. In order to be able to estimate production rates, we compared the rates for the proton- and α-induced production of ^{6,7}Li from ^{nat}C. The ratios of α- to proton-induced production for ^{6}Li from $^{\mathrm{nat}}$C is 2.56, for ^{7}Li, it is 2.44. Assuming the same α-to-proton-induced production ratios also for reactions on ^{nat}Si, we divided the proton-induced production rates for ^{6}Li and ^{7}Li from $^{\mathrm{nat}}$Si by factors of 2.56 and 2.44, respectively.

4.2.5 Uncertainties of cross sections

The excitation functions for the proton-induced production of helium and neon isotopes from silicon are mostly based on measured data that typically have uncertainties in the range of 5-10%. Any results from nuclear modeling were adjusted to experimental data; we therefore also assign uncertainties of 10% to the calculated values. For the production of ^{6,7}Li from

^{nat}C, there are less experimental data, and we therefore assigned an uncertainty of 20% to the excitation functions. For the reactions $^{nat}C(p,X)^{3}He$ and $^{nat}C(p,X)^{6,7}Li$, we assume that the uncertainties are about 50%, because even fewer experimental data are available, and we have to rely more on nuclear modeling. For the production of ^{6,7}Li from ^{nat}Si, no experimental cross sections are available, and we had to significantly scale the excitation function; we therefore assign an uncertainty of a factor of two to these excitation functions.

The database for α-induced reactions is more scarce than the database for proton-induced reactions; for most relevant reactions, no experimental data are available, and we have to rely on calculated cross sections. For the production of ^{6,7}Li, for which few experimental data are available, we assign an uncertainty of 50% to the excitation functions. For all other α-induced reactions, for which no experimental data are available, we assign an uncertainty of a factor of four to the excitation function, which is the maximum scaling factor used for our compilation (see above). Note that the uncertainties of the excitation functions directly propagate into the uncertainties for the modeled production rates.

4.3 Recoil loss

The model used here is essentially the same as the one used by Trappitsch and Leya (2013). However, for technical reasons, the former model was limited to protons with energies lower than 240 MeV, which was not a limiting factor for cosmogenic production rates in micrometeorites but is a serious limitation for cosmogenic production rates in presolar grains. Below, we briefly describe how the model is extended to higher energies (up to 10 GeV) and to α-particles as projectiles.

Up to an incident proton energy of 240 MeV, the production cross sections and recoil spectra for all relevant target-product combinations were calculated using TALYS-1.2 (Koning et al., 2008). To increase the energy resolution, we interpolated the recoil spectra linearly to a resolution of 0.1 MeV. In addition, we linearly extrapolated the recoil spectra towards zero recoil energy, which is important for very small grains because it accounts for the fact

that some product nuclides have a recoil energy of zero and can therefore remain even in the smallest grains. For each target-product combination, incident proton energy, and recoil energy, we calculated the stopping range using the PRAL algorithm (Biersack, 1981). The electronic and nuclear stopping parameters were calculated using the *srmodule* software of the SRIM package (Ziegler, 2004). Depending on the stopping range, the geometry of the target grain, the production location within the grain, and the momentum vector of the produced cosmogenic nuclide, we calculated whether or not the product nuclide is lost from the grain using the algorithm described in detail by Trappitsch and Leya (2013).

Since being consistent is very important for this type of calculation, we rely entirely on data determined using nuclear model codes. We expect that both models, i.e., TALYS-1.2 and INCL4.5/ABLA, can reliably predict relative values, i.e., cross sections and recoil spectra of one isotope relative to another isotope. This is confirmed by the finding that TALYS-1.2 calculates solar cosmic ray-produced $^{21}Ne/^{22}Ne$ ratios, i.e., relative production rates, very accurately (Meier et al., 2014). In addition, Trappitsch and Leya (2013) used the very same model to calculate recoil losses for the production of ^{21}Ne from silicon at 200 MeV incident proton energy and found that the calculations describe existing experimental values (Ott and Begemann, 2000) very accurately.

4.3.1 Recoil spectra for proton-induced reactions

For incident energies up to 240 MeV, we use the model given by Trappitsch and Leya (2013) (see above). At higher energies, the cross sections and recoil spectra were calculated using INCL4.5/ABLA07 (Boudard et al., 2002), which is a Monte Carlo code for the simulation of nuclear reactions in the energy range 200 MeV – 10 GeV. The INCL4.5/ABLA07 results are formatted to match the TALYS format. Figure 4.2 depicts relative recoil losses for the proton-induced production of ^{3}He, ^{6}Li, and ^{21}Ne in a 5 μm SiC grain as a function of incident proton energy. In this plot, a value of one indicates complete loss. Note that the data have been calculated using TALYS-1.2 below 240 MeV (solid symbols) and using

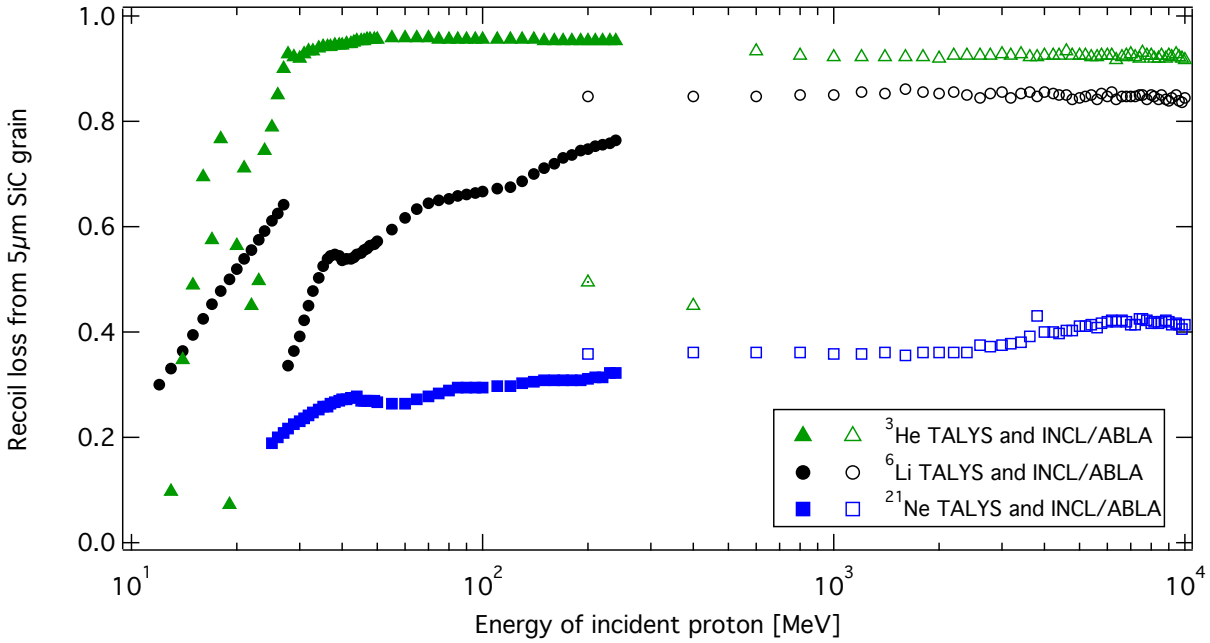

Figure 4.2 Recoil losses of ^{3}He, ^{6}Li, and ^{21}Ne for a 5 μm SiC grain as a function of incident proton energy. Below 200 MeV the results are based on TALYS-1.2 predictions (solid symbols). At higher energies the recoil losses are based on INCL4.5/ABLA07 results (open symbols).

INCL4.5/ABLA07 in the energy range 0.2 – 10 GeV (open symbols). For all three nuclides, there is a reasonable match between TALYS-1.2 and INCL4.5/ABLA07 results. For example, the recoil ranges in the overlapping energy range at 200 MeV differ by less than 10% and 5% for ^{6}Li and ^{21}Ne, respectively. For ^{3}He, the differences between both approaches are slightly larger. However, ignoring the first two datapoints calculated using INCL4.5/ABLA07 at 200 MeV and 400 MeV, the agreement for both nuclear model codes is excellent, i.e., the difference is only about 2%.

Figure 4.2 shows that the recoil losses for ^{3}He and ^{6}Li scatter widely close to the reaction threshold, which we consider computational artifacts, caused by low cross sections. However, these artifacts have only little effect on the calculated recoil losses, which has been checked by calculating ^{3}He and ^{6}Li recoil losses from a 5 μm SiC grain using the entire GCR spectrum. The first set of modeling fully considers the widely varying low energy part of the recoil losses, and, in the second set of modeling, we artificially set all recoil losses below 22 MeV

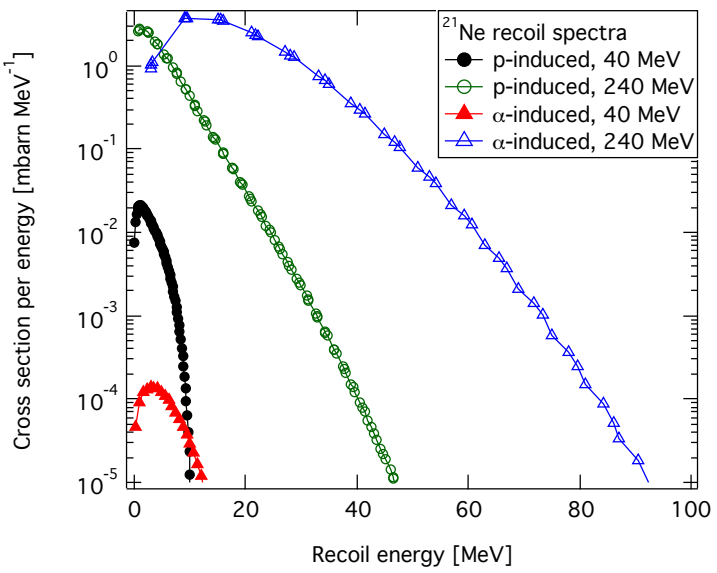

Figure 4.3 Comparison of recoil spectra for the production of ^{21}Ne from silicon at 40 MeV and 240 MeV (calculated using TALYS-1.2).

for ^{3}He and below 28 MeV for ^{6}Li to zero. The differences between both modeling types are 2% for ^{3}He and $< 0.1\%$ for ^{6}Li, clearly demonstrating that the scatter in the low-energy data has only little influence on the final results.

4.3.2 α-induced reactions

As already mentioned, INCL4.5/ABLA07 fails or has difficulties modeling α-induced reactions on carbon and silicon. We were therefore unable to calculate recoil losses for α-induced reactions at high projectile energies. To overcome this problem, we assume that the recoil losses for α-induced reactions are constant above 240 MeV. Although this assumption adds some uncertainties to the modeling, it is justified by the fact that recoil losses for proton-induced reactions are also constant at high energies. Neither TALYS-1.2 nor INCL4.5/ABLA07 can model the production of and/or the recoil losses for ^{6,7}Li from ^{nat}Si. To overcome this limitation, we assume that the recoil losses are the same as for the production of ^{6,7}Li by α-induced reactions on carbon. Although this will add some uncertainties, we expect them to be only very minor, because α-particles contribute only 7% to the GCR.

Figure 4.3 compares recoil spectra for the proton- and α-induced production of ^{21}Ne from ^{nat}Si at 40 MeV and 240 MeV. The general trend is similar for both projectile types; increasing cross sections per energy at very low recoil energies, local maxima in the range of a few MeV, and decreasing values at higher energies. With increasing projectile energy, the distribution becomes broader.

4.4 Results

4.4.1 Cosmogenic production rates

Table 4.1 compiles the α- and proton-induced production rates for ^{3}He and ^{6,7}Li from carbon and ^{3}He, ^{6,7}Li, and ^{21,22}Ne from silicon. The production rates are normalized to proton- and α-particle fluxes of 1 cm^{-2} s^{-1} and are for a GCR spectrum of $M = 0$ MeV. The uncertainties cover only the uncertainties of the excitation functions, uncertainties due to poorly known particle spectra are not included. There is an additional source of uncertainties for the ^{3}He production rates caused by poorly known contributions from the radioactive progenitor ^{3}H. Since ^{3}H has large diffusion rates, we assume that in presolar grains, all ^{3}H is lost to space before radioactive decay to ^{3}He. The production rates given in Table 4.1 are therefore only for the direct production of ^{3}He. If we would, as the other extreme, assume that all ^{3}H decays to ^{3}He in the presolar grain, i.e., that there are no diffusive losses of ^{3}H, the ^{3}He production rates from silicon and carbon would increase by factors of about 2.16 and about 1.76, respectively (Leya et al., 2004). The latter value is calculated based on the systematics for meteoroids given by Leya et al. (2004). We estimate that these factors have uncertainties of about 20%, which includes the fact that the ^{3}H/^{3}He production rate ratio might depend on the shape of the particle spectrum.

One interesting feature is that the ^{6}Li/^{7}Li ratio produced from carbon is about a factor of 2 lower than from silicon. This difference is due to the nuclear cross sections. Figure 4.1 shows the cross sections that we calculated for lithium production from carbon. Here, the

Table 4.1. Elemental production rates for cosmogenic ^{3}He, ^{6}Li, ^{7}Li, ^{21}Ne, and ^{22}Ne. Calculations were done assuming either protons or α particles as projectiles, a GCR spectrum with a modulation of 0 MeV and a flux density of $1\,\mathrm{cm^{-2}\,s^{-1}}$. The given uncertainties result solely from the cross section uncertainties (see text).

Cosmogenic nuclide	Elemental production rates $[10^{-10}\,\mathrm{cm^3\,STP\,g^{-1}\,Ma^{-1}}]$			
	C (p)	C (α)	Si (p)	Si (α)
^{3}He	21.8 ± 2.2	48.7 ± 24.3	9.8 ± 4.9	50.3 ± 201
^{6}Li	7.4 ± 1.5	19.0 ± 9.5	9.7 ± 9.7	24.7 ± 98.9
^{7}Li	13.2 ± 2.7	32.3 ± 16.2	8.1 ± 8.1	19.9 ± 79.3
^{21}Ne	-	-	4.7 ± 0.5	5.4 ± 21.8
^{22}Ne	-	-	5.5 ± 0.6	6.3 ± 25.2

calculations could be scaled to measured values. For silicon however, no measurements were available, such that the calculated production rates had to be used directly. The uncertainty associated with the lithium production from silicon is is so large that it agrees with the production rate ratio of the lithium isotopes from carbon.

4.4.2 Recoil loss

Figure 4.4 depicts retention fractions for ^{3}He, ^{6,7}Li, and ^{21,22}Ne in SiC grains with radii between 1 μm and 100 μm. The retention fractions for the α- and proton-induced production are shown separately in the upper and lower panel, respectively. For the product nuclides studied here, retention fractions at the same energy are slightly higher for the proton- than for the α-induced production. With the proton abundance a_p, and the α abundance a_α, and by considering the production rates, the total recoil loss fraction can be calculated via:

$$r_{tot} = \frac{a_p P_p r_p + a_\alpha P_\alpha r_\alpha}{a_p P_p + a_\alpha P_\alpha} \tag{4.3}$$

with P_p and P_α being the calculated production rates and r_p and r_α the recoil losses for the proton- and α-induced production, respectively. Figure 4.5 shows the recoil losses calculated

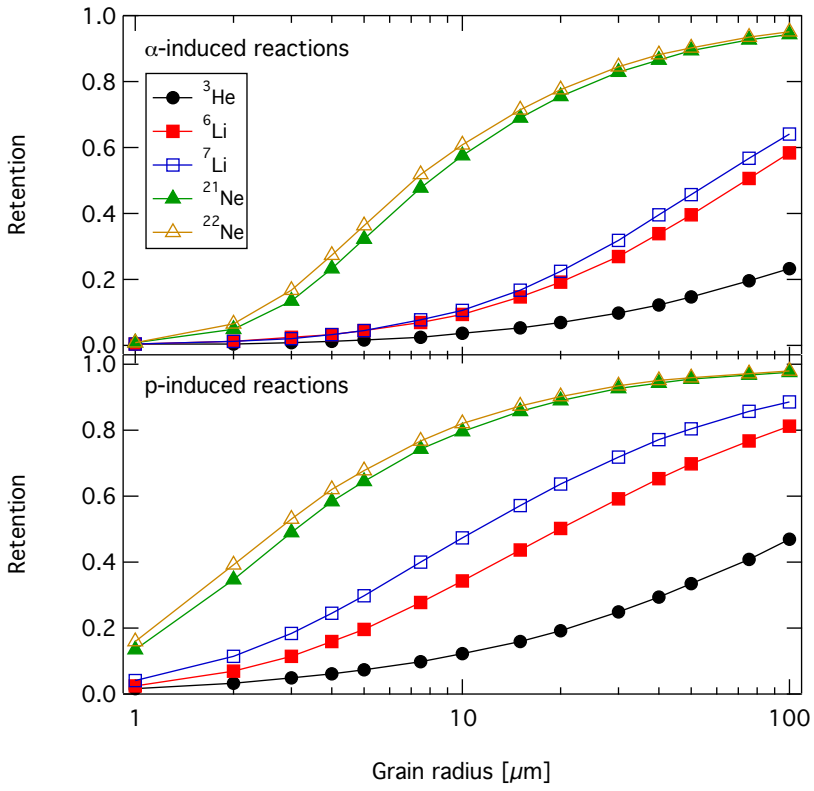

Figure 4.4 Retention of cosmogenic nuclides in SiC grains as a function of grain size. The top panel shows the retention for α-induced production; the lower panel shows the retention for the proton-induced production.

using equation (4.3) and assuming that the GCRs consist of 93% protons and 7% α particles.

Estimating the uncertainties of the recoil losses is difficult because for modeling, we rely entirely on calculated data that cannot be verified using experimental values. We assume an uncertainty of about 50% for the calculated recoil losses (see below). For real applications, however, the major source of uncertainty is probably not in the modeled data but in the assumed shape of the presolar grains. Here, we assume a perfect spherical shape for the grains. Any deviation from the spherical shape, especially considering conglomerates of SiC grains, increases the recoil losses compared to the modeling. Strictly speaking, the recoil losses calculated here should be considered as lower limits.

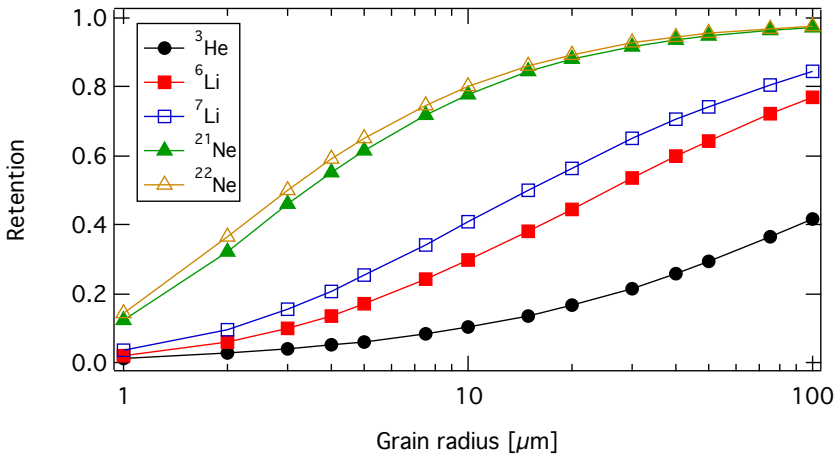

Figure 4.5 Retention of cosmogenic nuclides in SiC grains as a function of grain size for a GCR spectrum of 93% protons and 7% α-particles.

4.5 Comparing the model predictions to literature values

4.5.1 Cosmogenic production rates

The only previous study on cosmogenic production rates in presolar grains, by Reedy (1989), is based on a GCR particle spectrum with a solar modulation parameter $M = 100\,\mathrm{MeV}$ and a GCR particle fluence identical to the current value inside the Solar System. In contrast, our model uses a GCR spectrum with no modulation and flux densities consistent with values measured by Voyager outside the Solar System. A direct comparison is therefore not possible. Just for comparison, using a GCR spectrum with $M = 0\,\mathrm{MeV}$ but using the (wrong) particle fluence from Reedy (1989), we calculate production rates for ^{3}He about 20% lower, for ^{6}Li about 60% higher, for ^{7}Li about 10% higher, for ^{21}Ne about 10% higher, and for ^{22}Ne about 20% lower than the production rates by Reedy (1989). The agreement is reasonable, and the finding that our production rates for ^{6,7}Li are higher is at least partly due to fact that our model also considers production from silicon, a reaction path not considered by Reedy (1989). The remaining (minor) differences are most likely due to the updated cross section database used in our model and a more reliable description of the GCR particle spectrum. We therefore consider the new production rates as superior.

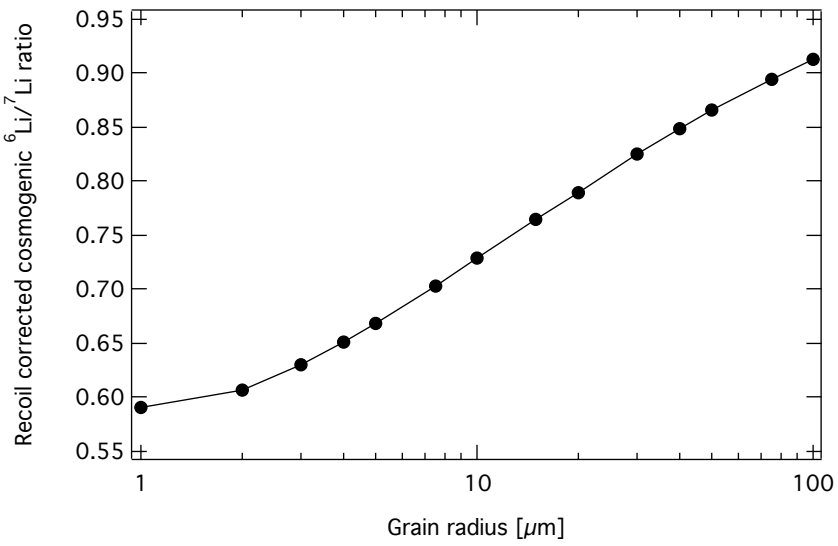

Figure 4.6 Recoil loss corrected cosmogenic ^{6}Li/^{7}Li ratio as a function of grain size for presolar SiC grains.

For calculating cosmogenic exposure ages using lithium isotopes, the spallogenic ^{6}Li/^{7}Li ratio has to be known. Figure 4.6 shows recoil-corrected ^{6}Li/^{7}Li ratios as a function of grain size for presolar SiC.

4.5.2 Recoil model

Validating the results of the recoil model is difficult, because only few experimental data exist. In the energy range 3–300 GeV, Steinberg and Winsberg (1974) studied proton-induced recoil of ^{22}Na and ^{24}Na in aluminum foils with thicknesses $< 7\,\mu$m and found losses in the range of 20%. Using our approach and assuming isotropic recoil momenta for the produced nuclides, we calculate values in the range of 20% to 30% for energies between 240 MeV and 10 GeV. The minor difference between modeled and measured data is most likely due to the relatively crude assumption of isotropic recoil momenta. In addition, Beyer and Herrmann (1978) and Lagarde-Simonoff et al. (1976) experimentally showed that above a projectile energy of 200 MeV, the energy has little influence on the kinetic energy of the recoil product, hence the recoil loss becomes almost constant. Our model reproduces this behavior very

accurately, as can be seen in Figure 4.2.

Previous recoil modeling has been done by Ott and Begemann (2000) and Ott et al. (2005). In their early study, Ott and Begemann (2000) assumed a constant recoil range for ^{21}Ne. Assuming for our approach the same constant recoil range, we are able to reproduce their retention curve. As the next step, we used our model to reproduce the average recoil range used by these authors. Doing so, we averaged the modeled recoil spectra by weighting all energies with their individual cross section per energy, which then gives the most likely recoil energy. Using these average energies, we then calculated average recoil ranges for each isotope. Based on experimental data for ^{21}Ne recoil at 1.6 GeV, Ott and Begemann (2000) calculated a recoil range for ^{21}Ne in SiC of 2.5 μm. Later, Ott et al. (2005) measured recoil ranges of 2 μm for the proton-induced production of ^{22}Na from silicon and aluminum at 66 MeV. Using the model, we calculate recoil ranges for the production of ^{22}Na from silicon and aluminum of 2.51 μm and 2.39 μm, respectively. For the target element barium, Ott et al. (2005) measured recoil ranges for ^{127}Xe at 66 MeV of $< 1.7\,\mu$m and for ^{126}Xe at 267 MeV of 0.21 μm. The modeled recoil range for ^{127}Xe at 66 MeV is 0.32 μm, and for ^{126}Xe at 240 MeV, it is 0.47 μm, i.e., both values are reasonably close to the measured data. At a proton energy of 1.2 GeV, Ott et al. (2005) reported a recoil range for ^{126}Xe produced from barium of 0.16 μm. Unfortunately, our model does not include INCL4.5/ABLA07 predictions for the target element barium, making a direct comparison impossible. However, considering that recoil energies are almost constant at higher projectile energies (see above), the measured value at 1.2 GeV (Ott et al., 2005) agrees reasonably well with our modeled value at 240 MeV.

There are three points that need to be emphasized. First, Ott and Begemann (2000) explored the possibility that the produced cosmogenic nuclides have no recoil energy; a fact that could not be quantified in their approach of constant recoil ranges but that is a natural outcome in our model and that is needed to explain why there is no complete recoil loss even in very small grains. Second, Lagarde-Simonoff et al. (1976) demonstrated that the recoil

range of a given nuclide at a given incident proton energy is linearly correlated with dA/A, with A the mass of the target nuclide and dA the mass difference between target and product. Ott et al. (2005) confirmed this linear relationship for barium isotopes. The same type of linear correlation can also be reproduced using our model. Note that Lagarde-Simonoff et al. (1976) analyzed recoil products that are heavier than the ones studied here. It is therefore difficult to directly compare their results to ours, but it is worth mentioning that according to the model, the light recoil corrections we are interested in follow the same type of correlation. Third, the recoil calculations by Gyngard et al. (2009b) for lithium isotopes are based on data for lithium production from carbon and oxygen from Greiner et al. (1975). However, their recoil spectrum has the maximum at much lower energies than we determined using the more reliable TALYS-1.2 and/or INCL4.5/ABLA07 codes. In addition, the data by Greiner et al. (1975) yield a poor agreement with the linear correlation given by Lagarde-Simonoff et al. (1976) that is confirmed by our model. Using the linear correlation, we expect that the recoil ranges used by Gyngard et al. (2009b) are too small, which is indeed what we confirmed using the model calculations (see above).

4.6 Cosmic ray exposure ages of presolar grains

We calculated cosmogenic production rates in presolar SiC grains using a GCR particle fluence in the ISM of $17.3\,\mathrm{cm}^{-2}\,\mathrm{s}^{-1}$, a solar modulation parameter M=0 MeV, and a GCR composition of 93% protons and 7% α particles (Table 4.2, see also above). Using the new production rates and considering recoil losses, we reevaluated the data published by Gyngard et al. (2009b,a) and Heck et al. (2008, 2009) to determine improved cosmic ray exposure ages for the first time fully considering the uncertainties of the production rates. Note that all of these measurements were performed on a selected subset of presolar SiC grains, i.e., large grains that are not necessarily representative of the majority of the presolar grain collection. However, small grains are more difficult to study due to their much lower abundance of cosmogenic nuclides and due to the fact that recoil corrections in small grains are large and

Table 4.2. Production rates of cosmogenic nuclides in SiC grains using the elemental production rates from Table 4.1, assuming a GCR composition of 93% protons and 7% α particles, and an integral particle flux of $17.3\,\mathrm{cm^{-2}\,s^{-1}}$ (Stone et al., 2013).

Cosmogenic nuclide	Production rate $[10^{-10}\,\mathrm{cm^3\,STP\,g^{-1}\,Ma^{-1}}]$
^{3}He	317 ± 135
^{6}Li	165 ± 101
^{7}Li	205 ± 86
^{21}Ne	41 ± 14
^{22}Ne	51 ± 17

thus more uncertain. For example, even cosmogenic neon isotopes, which have the lowest recoil losses of the cosmogenic nuclides studied, have a retention fraction of less than 20% in grains smaller than $1\,\mu$m radius.

4.6.1 Cosmic ray exposure ages based on lithium isotope data

The CRE ages determined from the lithium data by Gyngard et al. (2009b,a) are shown in Figure 4.7. The newly calculated CRE ages and retention fractions are given in Table 4.3. Unfortunately, Gyngard et al. (2009b,a) did not report uncertainties for the ages. The error bars reported by Gyngard et al. (2009b,a) only include the reported uncertainties for the measurements, they do not include any uncertainties from the production rates and the recoil correction. In contrast, the uncertainties shown for the reevaluated ages fully include uncertainties from the production rates and the recoil loss corrections, making them significantly larger.

The reevaluated CRE ages are within the (sometimes large) uncertainties identical to the ages originally given by Gyngard et al. (2009b,a). However, this is just by coincidence. Since the new production rates for ^{6,7}Li are larger but the new retention fractions are smaller, the net change is only very minor. For small grains, however, the differences are more pronounced

Table 4.3. Reevaluated retention fractions and grain ages for the presolar SiC grains measured by Gyngard et al. (2009b).

Grain label	Grain radius [μm]	Retention of ^{6}Li	Retention of ^{7}Li	T_6 [Ma]
a3-3	18.5	0.429	0.548	757 ± 478
a4-2	4.00	0.136	0.208	1572 ± 991
a4-4	11.5	0.326	0.440	40 ± 26
a4-5	21.5	0.462	0.580	39 ± 27
a5-1	2.50	0.078	0.127	1487 ± 931
b3-2	9.00	0.276	0.384	344 ± 226
b3-1	10.0	0.297	0.408	178 ± 110
b3-4	4.00	0.136	0.208	687 ± 501

because their age is dominated by the retention fraction, which is smaller using our model, making the ages higher. For larger grains, the new ages are lower than the original ones due to the higher production rates modeled by us compared to the ones used by Gyngard et al. (2009b,a). For those grains, recoil losses are only minor, and the differences in the retention fractions have only a minor effect on the ages.

Figure 4.7 shows that the CRE ages fall in a wide range from a few tens of Ma to more than 1 Ga. The two oldest grains have ages slightly higher than 1 Ga, four grains have CRE ages between 100 Ma and 1 Ga, and the two youngest grains have CRE ages <100 Ma. The three oldest grains are all $\leq 5\,\mu$m, and the recoil correction was significant, which makes the ages relatively uncertain. However, within uncertainty, all ages except for one are consistent with the grain survival theory, e.g., Jones et al. (1994, 1997).

4.6.2 Cosmic ray exposure ages based on ^{3}He and ^{21}Ne

In Figure 4.8, we compare the data originally measured by Heck et al. (2009) and reevaluated by Ott et al. (2009) (red triangles) with the reevaluated CRE ages determined using our model (black dots). The newly calculated CRE ages and retention fractions are given in

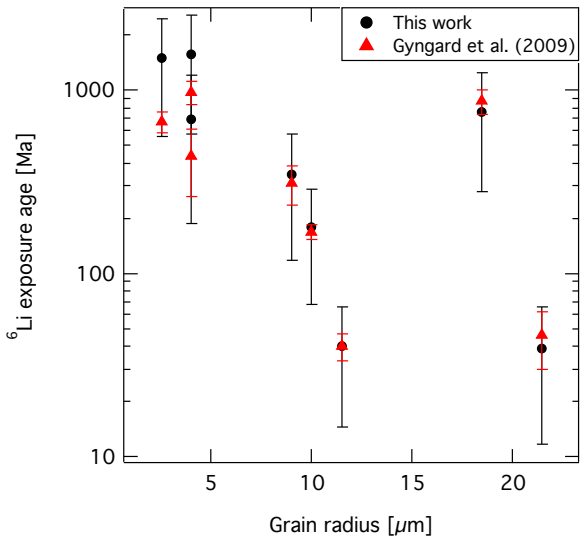

Figure 4.7 CRE ages based on the lithium isotope data measured by Gyngard et al. (2009b,a) as a function of grain size. The original ages are shown by red triangles; the reevaluated ages are shown by black dots. Error bars show 1σ uncertainties.

Table 4.4. In total, Heck et al. (2009) measured 22 presolar SiC grains and found measurable helium and neon concentrations in 11 of them. One of the grains had no detectable cosmogenic ^{3}He or ^{21}Ne and is therefore not evaluated here. The values originally published by Heck et al. (2009) were reevaluated by Ott et al. (2009) using a slightly improved method for recoil correction and including the production and loss of tritium for ^{3}He production. Even after the improved recoil correction, the CRE ages based on ^{3}He (T_3) were higher then the CRE ages based on ^{21}Ne (T_{21}) for five out of the 22 studied grains. Since we model even smaller retention fractions for spallogenic ^{3}He, we obtain even higher T_3 ages, therefore increasing the apparent discrepancy between T_3 and T_{21}. However, the disagreement between the T_3 and T_{21} ages is smaller than previously determined by Heck et al. (2008, 2009). Since we give, for the first time, uncertainties for the production rates and the recoil losses, which are relatively large for ^{3}He, we can conclude that, except for one grain, T_3 and T_{21} CRE ages agree within their 2σ uncertainties. The one discrepant grain has a higher T_{21} than T_3 age, which is most likely due to helium loss. For grains where one or both cosmogenic isotopes are given as upper limits, one grain has a ^{21}Ne record of zero, and T_3 and T_{21} obviously

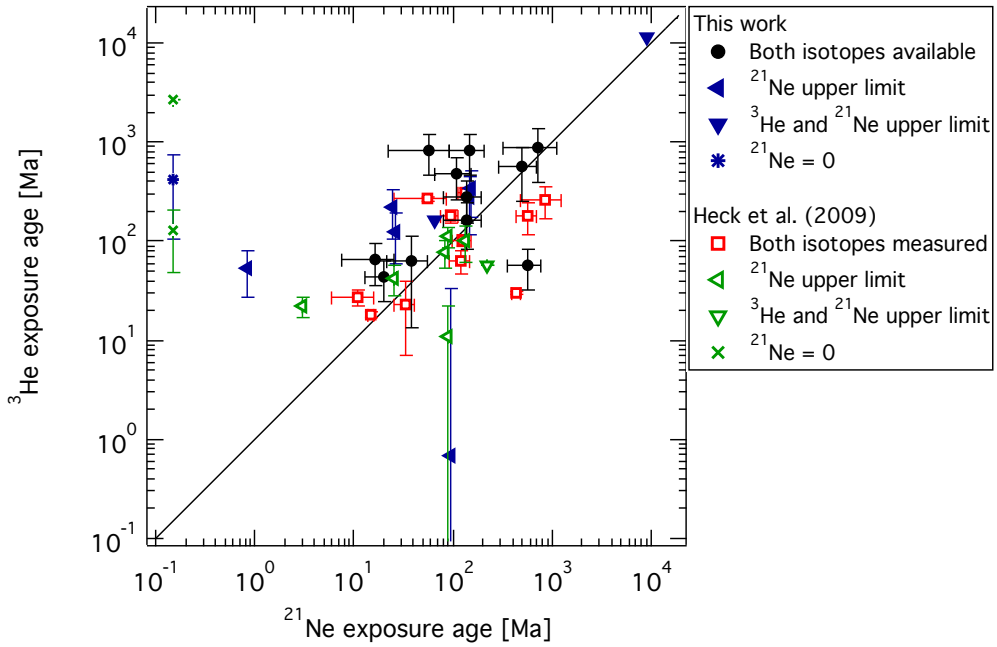

Figure 4.8 T_3 and T_{21} CRE ages. The cosmogenic ^{3}He and ^{21}Ne concentrations were measured by Heck et al. (2008, 2009) . The straight line with slope 1 indicates identical T_3 and T_{21} ages. Evaluations with a CRE age determined via cosmogenic ^{21}Ne of zero are shown arbitrarily at 0.15 Ma and marked with special symbols as described in the legend. Error bars show 1σ uncertainties.

Table 4.4 Reevaluated retention fractions and grain ages for the presolar SiC grains measured by Heck et al. (2009).

Grain label	Grain radius [μm]	Retention of ^{3}He	T_3 [Ma]	Retention of ^{21}Ne	T_{21} [Ma]
L2-01	7.3	0.081	809 ± 348	0.713	57 ± 35
L2-03	35.6	0.240	57 ± 25	0.929	574 ± 211
L2-04	9.2	0.096	$< 164 \pm 70$	0.762	$< 64 \pm 90$
L2-05	5.7	0.067	412 ± 311	0.652	~ 0
L2-06	17.3	0.150	43 ± 19	0.862	20 ± 7
L2-07	8.8	0.093	1 ± 32	0.753	$< 94 \pm 33$
L2-08	18	0.154	53 ± 26	0.867	$< 1 \pm 2$
L2-09	10.3	0.104	64 ± 50	0.783	38 ± 16
L2-10	9	0.094	217 ± 112	0.757	$< 24 \pm 34$
L2-11	11.8	0.115	164 ± 81	0.807	138 ± 58
L2-12	11	0.109	828 ± 364	0.795	149 ± 56
L2-13	7.8	0.082	337 ± 165	0.719	$< 153 \pm 54$
L2-14	11	0.109	473 ± 213	0.795	108 ± 43
L2-15	9.6	0.099	280 ± 164	0.770	$< 146 \pm 51$
L2-16	8.1	0.087	72 ± 31	0.736	97 ± 96
L2-17	8.4	0.090	123 ± 65	0.743	$< 26 \pm 9$
L2-18	15.6	0.140	66 ± 31	0.849	16 ± 9
L2-19	9.3	0.097	284 ± 127	0.764	137 ± 56
L2-25	4.9	0.059	888 ± 486	0.611	722 ± 401
L2-27	2	0.027	$< 11592 \pm 4950$	0.320	$< 8944 \pm 5917$
L2-57	5.8	0.067	575 ± 317	0.656	504 ± 210

disagree. One grain has too little ^{3}He, which can be explained by diffusion loss. For the other grains, T_3 and T_{21} agree within their 2σ uncertainty. These agreements are mostly due to the fact that the T_3 has a large uncertainty due to the poorly constrained production rates. Note that for all of these grains, the cosmogenic ^{21}Ne is an upper limit with no uncertainty. The uncertainties given here for these grains are only from the production rate model. One grain has an extremely high CRE age of several billion years. Both, T_3 and T_{21}, ages are upper limits. The T_{21} age was previously not calculated by Heck et al. (2009) since no recoil correction could be applied to such a small grain. Using the new recoil model, we calculated the retention fraction for this grain with 1 μm radius and determined an upper limit for the T_{21} age as well.

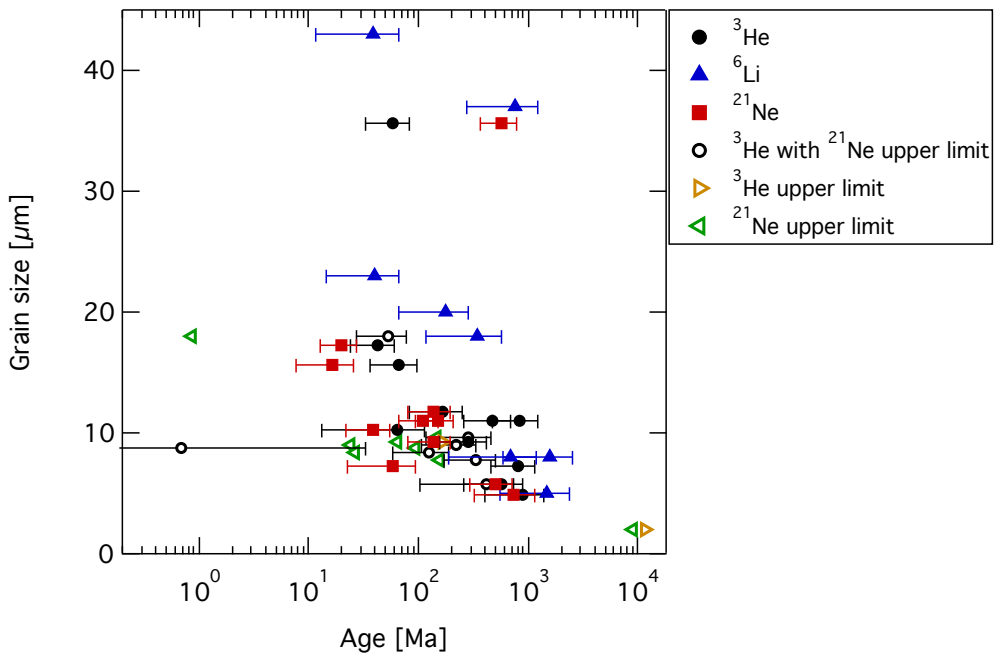

Figure 4.9 Reevaluated T_3, T_6, and T_{21} CRE ages as a function of grain size. Open symbols show T_3 and T_{21} ages with upper limits in either one or both isotopes. All grains agree within uncertainty with the theoretical grain survival time of ~ 600 Ma (Jones et al., 1994, 1997). Error bars show 1σ uncertainties.

Figure 4.9 shows the reevaluated CRE ages as a function of grain size. Two important conclusions can be drawn. First, there is no correlation between CRE ages and grain size. Second, the reevaluated CRE ages roughly agree with the calculated survival times, i.e., they are all smaller than the maximum survival times.

4.6.3 Additional comments

For studies of cosmogenic nuclides in presolar grains, several questions must be asked. *First*, can implantation of galactic ^{3}He affect the cosmogenic ^{3}He budget in the grain? Ott et al. (2009) proposed that implantation of low energetic helium particles from GCRs might (at least partly) explain why in some grains T_3 was higher than T_{21}. For the reevaluated data, however, T_3 and T_{21} agree within the (relatively large) 2σ uncertainties, therefore relaxing the requirement to explain apparent excess ^{3}He. Though, ^{3}He implantation cannot

be excluded, and further studies are recommended.

Second, is the cosmogenic record in the grains affected by nuclide production in the meteorite? All presolar grains considered here are from the Murchison meteorite. Herzog et al. (1997) determined a (single stage) CRE age for Murchison of 1.8 ± 0.3 Ma. Based on the cosmogenic production rate model by Leya and Masarik (2009), we can estimate production rates for ^{3}He of 100×10^{-10} cm^3 STP g^{-1} Ma^{-1} and for ^{21}Ne of 30×10^{-10} cm^3 STP g^{-1} Ma^{-1} for SiC grains within the Murchison meteoroid, i.e., about three times and two times lower than the respective production rates in the ISM. With the CRE age for Murchison, we can estimate that even for the grains with the lowest CRE ages, nuclide production during meteorite transit contributes at best a few percent only, which is within the given uncertainties. This agrees well with the findings of Tang and Anders (1988b).

Third, was there any nuclide production in the grains in the forming Solar System? GCR irradiation of presolar grains in the solar nebula prior to their incorporation into the meteoroid parent bodies can be neglected for various reasons. During this stage, GCRs in the disk are suppressed by several orders of magnitude due to an enhanced magnetic field of the protosun (e.g., Cleeves et al., 2013), and the midplane of the disk was shielded from solar cosmic rays (SCRs) by the thick envelope of gaseous hydrogen (e.g., Trappitsch and Ciesla, 2015).

Fourth, what effect does grain erosion in the interstellar medium have? If grain erosion plays a significant role in the presolar grains life, recoil corrections not taking erosion into account predict too much recoil. While the grain gets eroded, cosmogenic nuclides produced in an outer shell can recoil inwards and therefore be preserved even if their producing location gets lost over time. However, we assume this to be a minor effect that we are currently not taking into account. The survival time of a presolar SiC grain is ~ 600 Ma (Jones et al., 1994, 1997). Many of the presolar grain ages are much younger than this estimate, hence, erosion probably plays a minor role.

Fifth, how large is the effect of nearby stellar events on a presolar grain's cosmogenic

record? Here we assume that production of cosmogenic nuclides is solely due to GCRs in the interstellar medium. However, the birth star of the presolar grain might have a significant flux of high-energy particles, which would produce some amount of cosmogenic nuclides if the fluence of high-energy particles is high enough. Very little is known on the detailed transport of presolar grains from their production event to the early Solar System. While nearby stellar events and / or the parent star itself can influence the cosmogenic record, we currently do not have a real possibility to test and correct for this. One possible way in the future to check for such influences are correlated studies in individual presolar grains. The different cosmogenic nuclides have different excitation functions, therefore, are produced in different ratios depending on the high-energy particle spectrum. Correlated studies might be useful to distinguish multiple irradiation scenarios from each other in the future, however, presently we can not exclude or estimate the magnitude of this effect.

4.7 Conclusions

We presented a physical model to calculate CRE ages of presolar SiC grains. The cosmogenic production rates are calculated using a state-of-the-art nuclear cross section database and a GCR spectrum in the ISM consistent with recent Voyager data (Stone et al., 2013). The recoil model, which is fully consistent with the production rate model, is based on TALYS-1.2 and INCL4.5/ABLA07 predictions and takes all incident energies for protons and α particles into account. The results for the recoil model compare well to experimental data.

Using the model, we reevaluated the presolar grain data for ^{3}He and ^{21}Ne from Heck et al. (2008, 2009) and the lithium data from Gyngard et al. (2009b,a). Unfortunately, the two studies were not performed on the same set of grains. There are two important findings. *First*, most CRE ages based on ^{3}He and ^{21}Ne agree within the (sometimes large) 2σ uncertainties. Second, the CRE ages for most presolar grains are smaller than the predicted survival times. The results obtained are relatively robust because interferences from implanted low-energy GCRs into the presolar SiC grains and/or from cosmogenic production

within the meteoroid can be neglected.

Correlated studies of helium, lithium, and neon isotopes in individual presolar grains would allow to better constrain their CRE ages because such combined studies would allow to better understand and quantify possible problems due to, e.g., contamination, implantation, and/or diffusion. Recently, Gyngard et al. (2014) reported preliminary results on lithium in presolar SiC grains. The same grains were subsequently analyzed for cosmogenic helium and neon and the preliminary evaluation for all cosmogenic nuclides was reported by Heck et al. (2015). Such combined studies could help to a better understand transport and survival processes of presolar grains in the ISM before their incorporation into the forming Solar System.

CHAPTER 5

CONCLUSIONS AND OUTLOOK

In this work we described topics of presolar grain research, namely measurements of iron and nickel isotopic compositions and a new production and loss model for cosmogenic nuclides in presolar SiC grains. Here we want to advance the two topics and – in a more speculative way – discuss ideas for follow-up studies that will elucidate further our knowledge of GCE.

5.1 Galactic chemical evolution

Prior to this study, the most important elements used as proxies for studying GCE were silicon and titanium isotopes. Here, we presented iron and nickel isotopic measurements of presolar SiC grains and showed their suitability as GCE proxies. In contrast to a previous study by Marhas et al. (2008), the use of RIMS allowed us to measure all isotopes without isobaric interferences. In addition, our uncertainties are about a factor of four smaller thanks to the higher sensitivity of CHILI. Measuring the neutron-rich, minor isotopes in iron and nickel allows us to constrain the properties of the parent star of the measured presolar grains. Iron and nickel are however not the ideal systems to study stellar nucleosynthesis that took place in the presolar grain's parent AGB star since anomalies are still small compared to those of, e.g., barium and strontium isotopes (see, e.g., Liu et al., 2014, 2015).

We found the expected correlations between the GCE-dominated isotopes in silicon, iron, and nickel. We showed that the abundance of GCE-dominated silicon and iron isotopes increase with higher metallicity. However, the opposite is the case for nickel, i.e., δ^{60}Ni decreases with increasing metallicity, as expected in the models by Kobayashi et al. (2011). While the trends of GCE are reproduced well in the GCE model, the modeled trends for δ^{29}Si do not agree with the measurements and are too steep. This is in agreement with an underproduction of ^{29}Si in the SN models as was proposed previously (Timmes and Clayton, 1996). One of the most interesting observations in our study however is that we

found GCE trends to go through the solar value, i.e., the Solar System is not a special case in terms of GCE. This finding objects to the possibility that GCE has a straight age-metallicity dependance, which would make most of the measured presolar grains with, e.g., positive δ^{29}Si values younger than the Solar System in a GCE sense. If the age-metallicity relationship would hold up, the Solar System would have to be an outlier in the dataset, however, silicon, titanium, iron, and nickel GCE trends go through solar values rendering this explanation unlikely.

One possible solution to this problem was proposed by Clayton (2003) in form of the galactic merger model. Here, a dwarf-galaxy supposedly collided with the Milky Way and triggered a star formation burst of stars with various compositions. These stars, according to the merger model, produced the presolar grains that we see today, and started out with an initial composition that was a mixture of the low-metallicity dwarf galaxy and the Milky way. This would neatly explain the observed isotope ratios and trends of GCE dominated elements in presolar grains. The composition of the Sun in the model is simply one possible mixture of these two components and lies according to silicon and titanium on the metal-poor side of the mixing line. However, for iron and nickel, we find that the Solar System lies in the middle of the GCE trends for iron and nickel isotopes, which is not in agreement with such a mixture. The galactic merger model by Clayton (2003) therefore has to be rejected, since such a two component mixing process cannot explain the discussed measurement results.

An alternative explanation for the silicon isotopes has been proposed by Lugaro et al. (1999) in the form of a heterogeneous GCE model. The idea behind the model is that a limited amount of element producing events contributed to the composition of a given presolar grain parent star. The model uses a silicon isotopic composition of $^{29}\text{Si} = -100‰$ and $^{30}\text{Si} = -100‰$ as one endpoint of a mixing line. The second point of the mixing line is defined by the SNe yields. These yields are split between 80% type II, 16% type Ia, and 4% type Ia sub-Chandrasekhar SNe. For type II SNe, a whole range of masses are available. The average yields are here determined by weighing the individual yields with their

probability of occurrence according to a given initial mass function. The production of ^{29}Si was enhanced by approximately a factor of 1.5, such that this averaged composition yielded a second point on the mixing line that goes through the silicon isotope measurement results of presolar grains. From the starting composition with negative δ^{29}Si and δ^{30}Si, a given number of stellar yields that are randomly picked according to their occurrence probability are added to the initial composition. If only a limited number of stars is mixed with the initial composition, the final mixture will have a composition that lies in the area between the end members of the mixing line. This process is then repeated many times to evaluate which parameters are needed to reproduce the given spread in silicon isotope compositions. The same approach was used later by Nittler (2005) and includes silicon as well as titanium isotopes in combination with newer measurements. While parameters could be found to explain the distribution of silicon isotope ratios, the model did not reproduce the measured correlations between silicon and titanium. Lugaro et al. (1999) as well as Nittler (2005) used the type II SNe yields by Woosley and Weaver (1995). Since newer and more complete sets of type II supernova models are available, we wanted to compare results of the heterogeneous GCE model using various model grids (Trappitsch et al., 2013). We compared the models by Woosley and Weaver (1995), Woosley and Heger (2007), and Pignatari et al. (2016). Figure 5.1 shows the yields of the individual models weighted by an initial mass function. In addition, all presolar SiC mainstream grains that are in the presolar grain database and have uncertainties smaller than 10‰ are plotted along with the models. Enhancements in the ^{29}Si production are not included. If the ^{29}Si production in the models by Woosley and Heger (2007) is enhanced by a factor of ~ 1.5, the averaged supernova models lie perfectly on a mixing line starting at $^{29}\text{Si} = -100‰$, $^{30}\text{Si} = -100‰$, and going through the presolar SiC mainstream grain data. These conditions were used by Lugaro et al. (1999) as well as by Nittler (2005) to find the optimal parameters for explaining the presolar grain data. The type II SNe models by Woosley and Heger (2007) have a much finer grid for stellar masses compared to the Woosley and Weaver (1995) models, however, these models underproduce

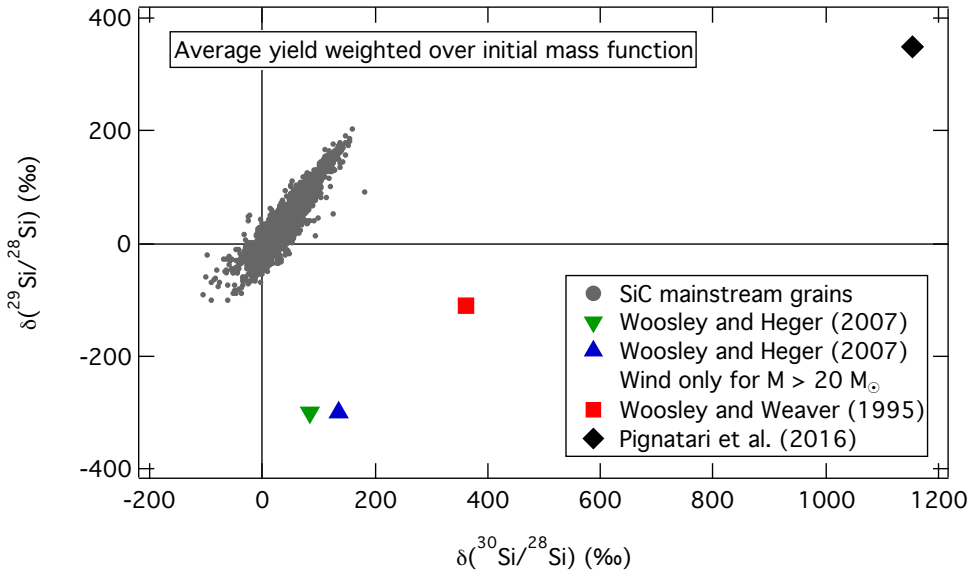

Figure 5.1 Presolar SiC mainstream grains in comparison with various supernovae model yields weighted over a Kroupa initial mass function (Kroupa, 2008). The presolar SiC mainstream grain data are taken from the presolar grain database (Hynes and Gyngard, 2009). Only grains with uncertainties in either axis that are $< 10‰$ are plotted.

^{29}Si and ^{30}Si, or overproduce ^{28}Si, and thus cannot explain the data. A simple enhancement in ^{29}Si puts the values in the middle of the measurement data, hence, these models cannot be an end member of the assumed mixing line. Considering nucleosynthesis yields from the supernova explosions only for stars $< 20\,M_{\odot}$ and only taking the stellar winds for heavier stars slightly improves the situation, however, does not solve the discrepancy either. The NuGrid models on the other side (Pignatari et al., 2016) produce on average much more ^{29}Si and ^{30}Si, or less ^{28}Si than the models by Woosley and Weaver (1995). An enhancement in ^{29}Si is still necessary in order to be on a mixing line with the presolar grain data. The comparison between the various SNe models shown in Figure 5.1 shows the huge variations in the silicon isotopic compositions that come out of the different type II SNe models. It is therefore not surprising that correlations between silicon and titanium isotopes could not be found by Nittler (2005) in the model frame of heterogeneous GCE. However, this model approach should not be rejected yet. A better understanding of supernova models and their uncertainties is needed to resolve these discrepancies.

In summary, GCE dominated isotopic compositions of silicon, titanium, iron, and nickel have been measured in presolar SiC grains. Here we presented the first study that measured all iron and nickel isotopes in presolar SiC grains. An age-metallicity relationship to explain GCE can be rejected at this point. A galactic merger explanation (Clayton, 2003) also seems unlikely considering the results presented here. The currently favorited model is heterogeneous GCE, however, the SNe models providing the isotopic yields can currently not be used directly to compare them to presolar grain data. The most valuable studies to provide further constraints on GCE are multi-element measurements in individual presolar SiC grains. For example, correlated studies of chromium and titanium isotopic compositions of presolar grains would be a logical next step. Chromium isotopic compositions have previously been measured with RIMS by Levine et al. (2009). Titanium isotope measurements with RIMS would further lower the uncertainties and give better constraints on GCE.

5.2 Cosmic ray exposure ages

In Chapter 4 we presented newly calculated production and retention rates for the production of cosmogenic helium, lithium, and neon in presolar SiC grains. These CRE ages are dependent on the used GCR spectrum in the interstellar medium and should therefore be thought of a *model* ages, however, they nevertheless yield valuable information on the transport processes of presolar grains through the interstellar medium. The best constraint CRE ages result from measuring cosmogenic ^{21}Ne since the cross sections for its production are well known, and the recoil corrections that need to be applied are small.

Figure 5.2 shows a probability density plot for the newly evaluated CRE ages for the neon measurements by Heck et al. (2009) and for the lithium measurements by Gyngard et al. (2009b). We do not include the helium data here because they are much less well constrained as discussed above. The blue shaded area in Figure 5.2 is the compilation of all 20 ^{21}Ne CRE ages, including the ones that only show lower limits. The high probability of the ages around 1 Ma is defined by these lower limit ages. The purple area shows the

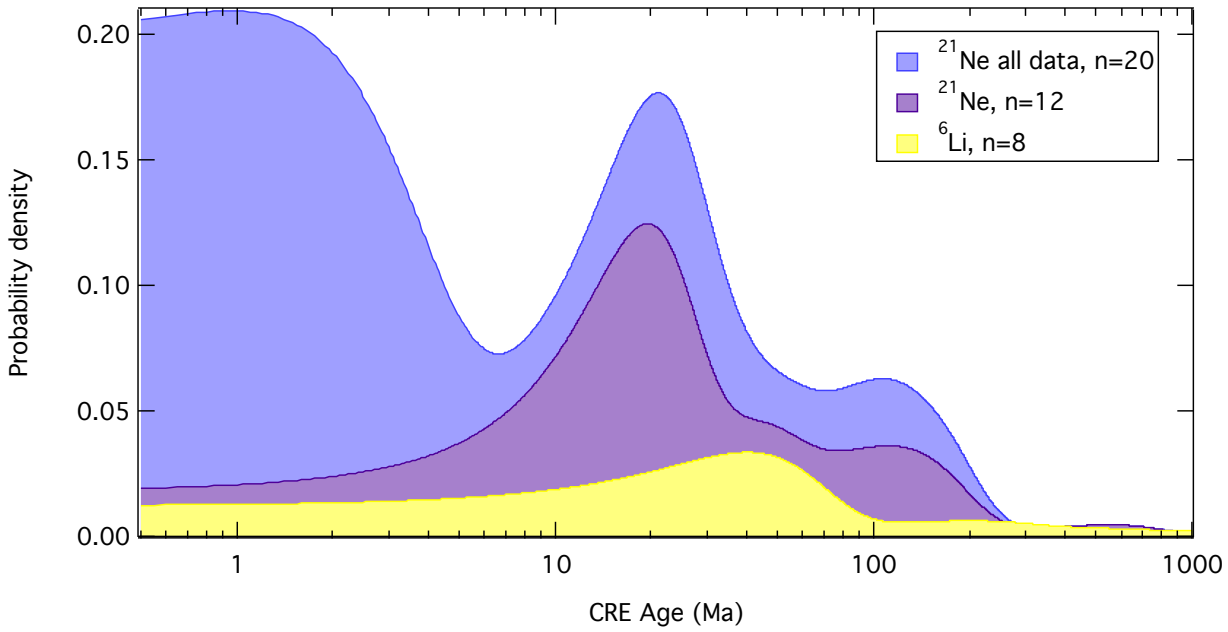

Figure 5.2 Probability density plot of the newly evaluated CRE ages

^{21}Ne CRE ages as well, however, only for the twelve grains that were not limited by the analytical procedures. In yellow we show the ages calculated using the eight presolar SiC grains that were analyzed for their lithium isotopic compositions. Note that lithium and neon measurements were performed on two different sets of presolar SiC grains.

The CRE ages determined via ^{21}Ne clearly show a peak in the distribution at around 20 Ma and a second peak at around 100 Ma. This indicates that at least two stellar events contributed to the analyzed presolar grains. A third possible peak shows in the form of a shoulder at around 50 Ma. The CRE ages determined via ^{6}Li shows one clear peak at around 40-50 Ma. Correlated studies like the one by Gyngard et al. (2014) and Heck et al. (2015), which measured helium, lithium, and neon isotopes in the same presolar SiC grain, will help in the future to better constrain the CRE ages, however, the measurement values from this study have not been published yet. The plotted data in Heck et al. (2015) shows that the calculated CRE ages are higher for lithium than for helium and neon. Our new model is unlikely to improve this discrepancy since the newly calculated recoil corrections for lithium are higher than the previously used ones (see Gyngard et al., 2009b). However,

the CRE ages should still agree with each other within the uncertainties. Since the new production rates include the systematic uncertainties, we can use correlated studies in the future to decide on the validity of the different cosmogenic isotope systems. More correlated helium, lithium, and neon cosmogenic nuclide measurements of presolar grains will however not only help to better understand the production rate uncertainties. Such studies – if performed on presolar grains with different grain sizes – will also help to deconvolute the source of error. Systematic errors in the retention rates for a given isotopes should show up in differences between various CRE ages that are grain size dependant. Finally, more measurements of presolar grain CRE ages will help to understand the distribution of stellar events that contributed to the inventory of grains found in meteorites.

While CRE ages are *model* ages, absolute dating, e.g., using the uranium-lead system, could yield an absolute anchor for these ages. However, this system is also not free of problems. The decay chain from uranium to lead includes several energetic decays that result in recoil of the product nucleus. We previously modeled these recoil effects (Trappitsch and Davis, 2013) and developed correction routines that can be used for correcting measurements. CHILI furthermore has the sensitivity to measure uranium and lead in presolar grains, therefore allowing a real shot at this "Holy Grail" of presolar grain analysis.

REFERENCES

Alexander, C.M.O'D., Nittler, L.R., 1999. The galactic evolution of Si, Ti, and O isotopic ratios. The Astrophysical Journal 519, 222–235.

Amari, S., Gao, X., Nittler, L.R., Zinner, E., José, J., Hernanz, M., Lewis, R.S., 2001a. Presolar grains from novae. The Astrophysical Journal 551, 1065–1072.

Amari, S., Hoppe, P., Zinner, E., Lewis, R.S., 1995. Trace-element concentrations in single circumstellar silicon carbide grains from the murchison meteorite. Meteoritics 30, 679–693.

Amari, S., Nittler, L.R., Zinner, E., Gallino, R., Lugaro, M., Lewis, R.S., 2001b. Presolar SiC grains of type Y: Origin from low-metallicity asymptotic giant branch stars1. The Astrophysical Journal 546, 248–266.

Amari, S., Nittler, L.R., Zinner, E., Lodders, K., Lewis, R.S., 2001c. Presolar SiC grains of type A and B: Their isotopic compositions and stellar origins. The Astrophysical Journal 559, 463–483.

Ammon, K., Masarik, J., Leya, I., 2009. New model calculations for the production rates of cosmogenic nuclides in iron meteorites. Meteoritics & Planetary Science 44, 485–503.

Barzyk, J.G., Savina, M.R., Davis, A.M., Gallino, R., Gyngard, F., Amari, S., Zinner, E., Pellin, M.J., Lewis, R.S., Clayton, R.N., 2007. Constraining the ^{13}C neutron source in AGB stars through isotopic analysis of trace elements in presolar SiC. Meteoritics & Planetary Science 42, 1103–1119.

Barzyk, J.G., Savina, M.R., Davis, A.M., Gallino, R., Pellin, M.J., Lewis, R.S., Amari, S., Clayton, R.N., 2006. Multi-element isotopic analysis of single presolar SiC grains. New Astronomy Reviews 50, 587–590.

Bauer, C.A., 1947. Production of helium in meteorites by cosmic radiation. Physical Review 72, 354–355.

Bell, A.R., 1978. The acceleration of cosmic rays in shock fronts - i. Monthly Notices of the Royal Astronomical Society 182, 147–156.

Bernatowicz, T.J., Messenger, S., Pravdivtseva, O., Swan, P., Walker, R.M., 2003. Pristine presolar silicon carbide. Geochimica et Cosmochimica Acta 67, 4679–4691.

Beyer, G.J., Herrmann, E., 1978. Zur darstellung kurzlebiger radioaktiver nuklide für die kernspektroskopie durch spallation. Habilitation thesis, Technische Universität Dresden, Germany. 75pp.

Biersack, J., 1981. Calculation of projected ranges – analytical solutions and a simple general algorithm. Nuclear Instruments and Methods 182/183, 199–206.

Bisterzo, S., Gallino, R., Straniero, O., Cristallo, S., Käppeler, F., 2010. s-process in low-metallicity stars – I. theoretical predictions. Monthly Notices of the Royal Astronomical Society 404, 1529–1544.

Boudard, A., Cugnon, J., Leray, S., Volant, C., 2002. Intranuclear cascade model for a comprehensive description of spallation reaction data. Physical Review C 66, 044615–1–044615–28.

Briesmeister, J.F., 1993. MCNP – A general Monte Carlo N-particle transport code, version 4A. Technical Report LA-12625-M. Los Alamos National Laboratory.

Broeders, C.H.M., Konobeyev, A.Y., Mercatali, L., 2006. Global comparison of TALYS and ALICE code calculations and evaluated data from ENDF/B, JENDL, FENDL, and JEFF files with measures neutron induced reaction cross-sections at energies above 0.1 mev. Journal of Nuclear and Radiochemical Sciences 7, N1–N4.

Cameron, A.G.W., Truran, J.W., 1977. The supernova trigger for formation of the solar system. Icarus 30, 447–461.

Castagnoli, G., Lal, D., 1980. Solar moldulation effects in terrestrial production of carbon-14. Radiocarbon 22, 133–158.

Clayton, D.D., 2003. A presolar galactic merger spawned the SiC-grain mainstream. The Astrophysical Journal 598, 313–324.

Clayton, D.D., Timmes, F.X., 1997. Implications of presolar grains for galactic chemical evolution. AIP Conference Proceedings 402, 237–264.

Cleeves, L.I., Adams, F.C., Bergin, E.A., 2013. Exclusion of cosmic rays in protoplanetary disks: Stellar and magnetic effects. The Astrophysical Journal 772, 5 (20pp).

Cristallo, S., Piersanti, L., Straniero, O., Gallino, R., Domínguez, I., Abia, C., Di Rico, G., Quintini, M., Bisterzo, S., 2011. Evolution, nucleosynthesis, and yields of low-mass asymptotic giant branch stars at different metallicities. II. the FRUITY database. The Astrophysical Journal Supplement 197, 17 (21pp).

Cristallo, S., Straniero, O., Gallino, R., Piersanti, L., Domínguez, I., Lederer, M.T., 2009. Evolution, nucleosynthesis, and yields of low-mass asymptotic giant branch stars at different metallicities. The Astrophysical Journal 696, 797–820.

Davids, C.N., Laumer, H., Austin, S.M., 1970. Production of the light elements lithium, beryllium, and boron by proton spallation of ^{12}C. Physical Review C 1, 270–275.

Davis, A.M., 2011. Stardust in meteorites. Proceedings of the National Academy of Sciences 108, 19142–19146.

Davis, A.M., Pellin, M.J., Lewis, R.S., Amari, S., Clayton, R.N., 1999. Light and heavy element isotopic compositions of mainstream SiC grains. Lunar and Planetary Science Conference 30, abstract #1976.

Fairbank, Jr., W.M., Spaar, M.T., Parks, J.E., Hutchinson, J.M.R., 1989. Anomalous odd- to even-mass isotope ratios in resonance ionization with broad-band lasers. Physical Review A 40, 2195–2198.

Foster, P.N., Boss, A.P., 1996. Triggering star formation with stellar ejecta. The Astrophysical Journal 468, 784–796.

Foster, P.N., Boss, A.P., 1997. Injection of radioactive nuclides from the stellar source that triggered the collapse of the presolar nebula. The Astrophysical Journal 489, 346–357.

Gallino, R., Arlandini, C., Busso, M., Lugaro, M., Travaglio, C., Straniero, O., Chieffi, A., Limongi, M., 1998. Evolution and nucleosynthesis in low-mass asymptotic giant branch stars. II. neutron capture and the s-process. The Astrophysical Journal 497, 388–403.

Gnaser, H., 1999. Low-Energy Ion Irradiation of Solid Surfaces. volume 146 of *Springer Tracts in Modern Physics*. Springer-Verlag, Berlin Heidelberg, 293pp.

Gnaser, H., Hutcheon, I.D., 1987. Velocity-dependent isotope fractionation in secondary-ion emission. Phys. Rev. B 35, 877–879.

Greiner, D.E., Lindstrom, P.J., Heckman, H.H., Cork, B., Bieser, F.S., 1975. Momentum distributions of isotopes produced by fragmentation of relativistic ^{12}C and ^{16}O projectiles. Physical Review Letters 35, 152–155.

Gyngard, F., Amari, S., Zinner, E., Ott, U., 2009a. Cosmic-ray exposure ages of large presolar SiC grains. Publications of the Astronomical Society of Australia 26, 278–283.

Gyngard, F., Amari, S., Zinner, E., Ott, U., 2009b. Interstellar exposure ages of large presolar SiC grains from the murchison meteorite. The Astrophysical Journal 694, 359–366.

Gyngard, F., Avila, J.N., Ireland, T.R., Zinner, E., 2014. More interstellar exposure ages of large presolar SiC grains from the murchison meteorite. Lunar and Planetary Science Conference 45, abstract #2348.

Heck, P.R., Gyngard, F., Maden, C., Busemann, H., Wieler, R., Avila, J.N., 2015. New interstellar helium and neon exposure ages of presolar jumbo SiC grains from murchison. Lunar and Planetary Science Conference 46, abstract #1748.

Heck, P.R., Gyngard, F., Meier, M.M.M., Avila, J.N., Amari, S., Zinner, E., Lewis, R.S., Baur, H., Wieler, R., 2008. Presolar neon and helium exposure ages of jumbo presolar SiC grains (LS+LU) from murchison. Lunar and Planetary Science Conference 39, abstract #1239.

Heck, P.R., Gyngard, F., Ott, U., Meier, M.M.M.M., Ávila, J.N., Amari, S., Zinner, E.K., Lewis, R.S., Baur, H., Wieler, R., 2009. Interstellar residence times of presolar sic dust grains from the murchison carbonaceous meteorite. The Astrophysical Journal 698, 1155–1164.

Herwig, F., 2013. Evolution of Solar and Intermediate-Mass Stars. In *Planets, Stars, and Stellar Systems Vol. 4* (eds. T. D. Oswalt and M. A. Barstow). Springer Reference, Dordrecht. pp. 397–445.

Herzog, G.F., Vogt, S., Albrecht, A., Xue, S., Fink, D., Klein, J., Middleton, R., Weber, H.W., Schultz, L., 1997. Complex exposure histories for meteorites with "short" exposure ages. Meteoritics & Planetary Science 32, 413–422.

Hoppe, P., Cohen, S., Meibom, A., 2013. NanoSIMS: technical aspects and aapplication in cosmochemistry and biological geochemistry. Geostandards and Geoanalytical Research 37, 111–154.

Hurst, G.S., Payne, M.G., Kramer, S.D., Young, J.P., 1979. Resonance ionization spectroscopy and one-atom detection. Reviews of Modern Physics 51, 767–819.

Hynes, K.M., Gyngard, F., 2009. The presolar grain database: http://presolar.wustl.edu/∼pgd. Lunar and Planetary Science Conference 40, abstract #1198.

Jaeger, M., Kunz, R., Mayer, A., Hammer, J.W., Staudt, G., Kratz, K.L., Pfeiffer, B., 2001. ^{22}Ne(α,n)^{25}Mg: The key neutron source in massive stars. Physical Review Letters 87, 202501 (4pp).

Jones, A.P., Tielens, A.G.G.M., Hollenbach, D.J., McKee, C.F., 1994. Grain destruction in shocks in the interstellar medium. The Astrophysical Journal 433, 797–810.

Jones, A.P., Tielens, A.G.G.M., Hollenbach, D.J., McKee, C.F., 1997. The propagation and survival of interstellar grains, in: Bernatowicz, T.J., Zinner, E. (Eds.), American Institute of Physics Conference Series, pp. 595–613.

Käppeler, F., Gallino, R., Bisterzo, S., Aoki, W., 2011. The s process: Nuclear physics, stellar models, and observations. Reviews of Modern Physics 83, 157–194.

Käppeler, F., Wiescher, M., Giesen, U., Goerres, J., Baraffe, I., El Eid, M., Raiteri, C.M., Busso, M., Gallino, R., Limongi, M., Chieffi, A., 1994. Reaction rates for ^{18}O(α, γ)22Ne, ^{22}Ne(α, γ)^{26}Mg, and ^{22}Ne(α,n)^{25}Mg in stellar helium burning and s-process nucleosynthesis in massive stars. The Astrophysical Journal 437, 396–409.

Kashiv, Y., 2004. Trace Element Abundances in Single Presolar SiC Grains by Synchrotron X-Ray Fluorescence. Ph.D. thesis. The University of Chicago.

Kobayashi, C., Karakas, A.I., Umeda, H., 2011. The evolution of isotope ratios in the milky way galaxy. Montly Notices of the Royal Astronomical Society 414, 3231–3250.

Kobayashi, C., Umeda, H., Nomoto, K., Tominaga, N., Ohkubo, T., 2006. Galactic chemical evolution: Carbon through zinc. The Astrophysical Journal 653, 1145–1171.

Koning, A.J., Hilaire, S., Duijvestijn, M.C., 2008. Talys-1.0, in: Bersillon, O., Gunsing, F., Bauge, E., Jacqmin, R., Leray, S. (Eds.), Proceedings of the International Conference on Nuclear Data for Science and Technology, EDP Sciences, Nice. p. 058.

Kroupa, P., 2008. The imf of simple and composite populations, in: Knapen, J.H., Mahoney, T.J., Vazdekis, A. (Eds.), Pathways Through an Eclectic Universe, p. 3.

Kruger, S.T., Heymann, D., 1973. High energy proton production of ^{3}H, ^{3}He, and ^{4}He in light targets. Physical Review C 7, 2179–2187.

Lagarde-Simonoff, M., Regnier, S., Sauvageon, H., Simonoff, G., 1976. Recoil properties of spallation products from bombardment of Z = 13-29 targets with 150,300 and 600 MeV protons. Nuclear Physics A 260, 369–380.

Levine, J., Savina, M.R., Stephan, T., Dauphas, N., Davis, A.M., Knight, K.B., Pellin, M.J., 2009. Resonance ionization mass spectrometry for precise measurements of isotope ratios. International Journal of Mass Spectrometry 288, 36–43.

Lewis, R.S., Amari, S., Anders, E., 1990. Meteoritic silicon carbide - pristine material from carbon stars. Nature 348, 293–298.

Lewis, R.S., Amari, S., Anders, E., 1994. Interstellar grains in meteorites: II. SiC and its noble gases. Geochimica et Cosmochimica Acta 58, 471–494.

Lewis, R.S., Ming, T., Wacker, J.F., Anders, E., Steel, E., 1987. Interstellar diamonds in meteorites. Nature 326, 160–162.

Leya, I., 1997. Modellrechnungen zur Beschreibung der Wechselwirkungen galaktischer kosmischer Teilchenstrahlung mit Stein- und Eisenmeteoroiden Dünntargetbestrahlungen und Dicktargetexperimente. Ph.D. thesis. University of Hannover.

Leya, I., Begemann, F., Weber, H.W., Wieler, R., Michel, R., 2004. Simulation of the interaction of galactic cosmic ray protons with meteoroids: On the production of ^{3}H and light noble gas isotopes in isotropically irradiated thick gabbro and iron targets. Meteoritics & Planetary Science 39, 367–386.

Leya, I., Masarik, J., 2009. Cosmogenic nuclides in stony meteorites revisited. Meteoritics & Planetary Science 44, 1061–1086.

Liu, N., Savina, M.R., Davis, A.M., Gallino, R., Straniero, O., Gyngard, F., Pellin, M.J., Willingham, D.G., Dauphas, N., Pignatari, M., Bisterzo, S., Cristallo, S., Herwig, F., 2014. Barium isotopic composition of mainstream silicon carbides from murchison: Constraints for s-process nucleosynthesis in asymptotic giant branch stars. The Astrophysical Journal 786, 66 (20pp).

Liu, N., Savina, M.R., Gallino, R., Davis, A.M., Bisterzo, S., Gyngard, F., Käppeler, F., Cristallo, S., Dauphas, N., Pellin, M.J., Dillmann, I., 2015. Correlated strontium and barium isotopic compositions of acid-cleaned single mainstream silicon carbides from murchison. The Astrophysical Journal 803, 12 (23pp).

Lodders, K., Palme, H., Gail, H.P., 2009. Abundances of the Elements in the Solar System. In *Landolt- Börnstein, New Series, Vol. VI/4B, Chap. 4.4* (ed. J. E. Trumper). Springer-Verlag, Berlin, Heidelberg, New York. Landolt-Börnstein, New Series, Vol. VI/4B, pp. 560–630.

Longland, R., Iliadis, C., Karakas, A.I., 2012. Reaction rates for the s-process neutron source ^{22}Ne + α. Physical Review C 85, 065809 (20pp).

Lugaro, M., Zinner, E., Gallino, R., Amari, S., 1999. Si isotopic ratios in mainstream presolar SiC grains revisited. The Astrophysical Journal 527, 369–394.

Ma, Z., Thompson, R.N., Lykke, K.R., Pellin, M.J., Davis, A.M., 1995. New instrument for microbeam analysis incorporating submicron imaging and resonance ionization mass spectrometry. Review of Scientific Instruments 66, 3168–3176.

Mamyrin, B.A., Karataev, V.I., Shmikk, D.V., Zagulin, V.A., 1973. The mass-reflectron, a new nonmagnetic time-of-flight mass spectrometer with high resolution. Soviet Journal of Experimental and Theoretical Physics 37, 45–48.

Marhas, K.K., Amari, S., Gyngard, F., Zinner, E., Gallino, R., 2008. Iron and nickel isotopic ratios in presolar SiC grains. The Astrophysical Journal 689, 622–645.

Masarik, J., Reedy, R.C., 1994. Effects of bulk composition on nuclide production processes in meteorites. Geochemica et Cosmochimica Acta 58, 5307–5317.

Meier, M.M.M., Schmitz, B., Alwmark, C., Trappitsch, R., Maden, C., Wieler, R., 2014. He and Ne in individual chromite grains from the regolith breccia Ghubara (L5): Exploring the history of the L chondrite parent body regolith. Meteoritics & Planetary Science 49, 576–594.

Meier, M.M.M., Schmitz, B., Alwmark, C., Trappitsch, R., Maden, C., Wieler, R., 2014. He and Ne in individual chromite grains from the regolith breccia ghubara (L5): Exploring the history of the L chondrite parent body regolith. Meteoritics & Planetary Science 49, 576–594.

Meyer, B.S., Zinner, E., 2006. Nucleosynthesis. In *Meteorites and the Early Solar System II* (eds. D. S. Lauretta and H. Y. McSween). The University of Arizona Press, Tucson, AZ. pp. 69–108.

Michel, R., Gloris, M., Lange, H.J., Leya, I., Lüpke, M., Herpers, U., Dittrich-Hannen, B., Rösel, R., Schiekel, Th., Filges, D., Dragovitsch, P., Suter, M., Hofmann, H.J., Wölfli, W., Kubik, P.W., Baur, H., Wieler, R., 1995. Nuclide production by proton-induced reactions on elements ($6 \leq z \leq 29$) in the energy range from 800 to 2600 MeV. Nuclear Instruments and Methods in Physics Research Section B: Beam Interactions with Materials and Atoms 103, 183 – 222.

Mohapatra, R.K., Merchel, S., Ott, U., Herpers, U., Michel, R., 2001. Recoil of spallation xenon: Hope for dating presolar SiC. Lunar and Planetary Science Conference 32, abstract #1296.

Moore, C.E., 1971. Atomic Energy Levels as Derived from the Analyses of Optical Spectra. volume 2. NIST, Washington DC.

Nicolussi, G., Davis, A., Pellin, M., Lewis, R., Clayton, R., Amari, S., 1997a. s-process zirconium in presolar silicon carbide grains. Science 277, 1281–1283.

Nicolussi, G., Pellin, M., Calaway, W., Lewis, R., Davis, A., Amari, S., Clayton, R., 1997b. Isotopic analysis of Ca from extraterrestrial micrometer-sized SiC by laser desorption and resonant ionization mass spectroscopy. Analytical Chemistry 69, 1140–1146. Cited By 26.

Nicolussi, G., Pellin, M., Lewis, R., Davis, A., Amari, S., Clayton, R., 1998a. Molybdenum isotopic composition of individual presolar silicon carbide grains from the murchison meteorite. Geochimica et Cosmochimica Acta 62, 1093–1104.

Nicolussi, G., Pellin, M., Lewis, R., Davis, A., Clayton, R., Amari, S., 1998b. Strontium isotopic composition in individual circumstellar silicon carbide grains: A record of s-process nucleosynthesis. Physical Review Letters 81, 3583–3586.

Nicolussi, G.K., Pellin, M.J., Lewis, R.S., Davis, A.M., Clayton, R.N., Amari, S., 1998c. Zirconium and molybdenum in individual circumstellar graphite grains: New isotopic data on the nucleosynthesis of heavy elements. The Astrophysical Journal 504, 492–499.

Nittler, L.R., 2005. Constraints on heterogeneous galactic chemical evolution from meteoritic stardust. The Astrophysical Journal 618, 281–296.

Nomoto, K., Kobayashi, C., Tominaga, N., 2013. Nucleosynthesis in stars and the chemical enrichment of galaxies. Annual Review of Astronomy and Astrophysics 51, 457–509.

Ong, W.J., Floss, C., 2015. Iron isotopic measurements in presolar silicate and oxide grains from the Acfer 094 ungrouped carbonaceous chondrite. Meteoritics & Planetary Science 50, 1392–1407.

Ott, U., Altmaier, M., Herpers, U., Kuhnhenn, J., Merchel, S., Michel, R., Mohapatra, R.K., 2001. Update on recoil loss of spallation products from presolar grains. Meteoritics & Planetary Science Supplement 36, A155.

Ott, U., Altmaier, M., Herpers, U., Kuhnhenn, J., Merchel, S., Michel, R., Mohapatra, R.K., 2005. Spallation recoil II: Xenon evidence for young SiC grains. Meteoritics & Planetary Science 40, 1635–1652.

Ott, U., Begemann, F., 2000. Spallation recoil and age of presolar grains in meteorites. Meteoritics & Planetary Science 35, 53–63.

Ott, U., Heck, P.R., Gyngard, F., Wieler, R., Wrobel, F., Amari, S., Zinner, E., 2009. He and Ne ages of large presolar silicon carbide grains: Solving the recoil problem. Publications of the Astronomical Society of Australia 26, 297–302.

Overholt, A.C., Melott, A.L., 2013. Cosmogenic nuclide enhancement via deposition from long-period comets as a test of the younger dryas impact hypothesis. Earth and Planetary Science Letters 377-378, 55–61.

Page, R.H., Gudeman, C.S., 1990. Completing the iron period: double-resonance, fluorescence-dip rydberg spectroscopy and ionization potentials of titanium, vanadium, iron, cobalt, and nickel. Journal of the Optical Society of America B 7, 1761–1771.

Paneth, F.A., 1952. Meteorites and cosmic rays. Nature 170, 729.

Paneth, F.A., Reasbeck, P., Mayne, K.I., 1952. Helium 3 content and age of meteorites. Geochimica et Cosmochimica Acta 2, 300–303.

Pellin, M.J., Davis, A.M., Calaway, W.F., Lewis, R.S., Clayton, R.N., 2000. Zr and Mo isotopic constraints on the origins of unusual types of presolar SiC grains. Lunar and Planetary Science Conference 31, abstract #1934.

Pellin, M.J., Davis, A.M., Lewis, R.S., Amari, S., Clayton, R.N., 1999. Molybdenum isotopic composition of single silicon carbide grains from supernovae. Lunar and Planetary Science Conference 30, abstract #1969.

Pellin, M.J., Savina, M.R., Calaway, W.F., Tripa, C.E., Barzyk, J.G., Davis, A.M., Gyngard, F., Amari, S., Zinner, E., Lewis, R.S., Clayton, R.N., 2006. Heavy metal isotopic anomalies in supernovae presolar grains. Lunar and Planetary Science Conference 37, abstract #2041.

Pellin, M.J., Young, C.E., Calaway, W.F., Gruen, D.M., 1984. Trace surface analysis with pico-coulomb ion fluences: Direct detection of multiphoton ionized iron atoms from iron-doped silicon targets. Surface Science 144, 619–637.

Piersanti, L., Cristallo, S., Straniero, O., 2013. The effects of rotation on *s*-process nucleosynthesis in asymptotic giant branch stars. The Astrophysical Journal 774, 98 (11pp).

Pignatari, M., Herwig, F., Hirschi, R., Bennett, M., Rockefeller, G., Fryer, C., Timmes, F., Heger, A., Jones, S., Battino, U., Ritter, C., Dotter, A., Trappitsch, R., Diehl, S., Frischknecht, U., Hungerford, A., Magkotsios, G., Travaglio, C., Young, P., 2016. NuGrid stellar data set. I. stellar yields from H to Bi for stars with metallicities $z = 0.02$ and $z = 0.01$. The Astrophysical Journal Supplement, in press.

Raisbeck, G.M., Lestringuez, J., Yiou, F., 1972. Cross sections for ^{6}Li and ^{7}Li production from the bombardment of ^{12}C by 150- and 600-MeV protons and 880-MeV alpha particles. Physical Review C 6, 685–690.

Rauscher, T., Heger, A., Hoffman, R.D., Woosley, S.E., 2002. Nucleosynthesis in massive stars with improved nuclear physics. The Astrophysical Journal 576, 323–348.

Reedy, R.C., 1989. Cosmogenic-nuclide production rates in interstellar grains. Lunar and Planetary Science Conference 20, 888–889.

Savina, M.R., Davis, A.M., Tripa, C.E., Pellin, M.J., Clayton, R.N., Lewis, R.S., Amari, S., Gallino, R., Lugaro, M., 2003a. Barium isotopes in individual presolar silicon carbide grains from the murchison meteorite. Geochimica et Cosmochimica Acta 67, 3201–3214.

Savina, M.R., Pellin, M.J., Tripa, C.E., Veryovkin, I.V., Calaway, W.F., Davis, A.M., 2003b. Analyzing individual presolar grains with CHARISMA. Geochimica et Cosmochimica Acta 67, 3215–3225.

Simpson, J.A., 1983. Elemental and isotopic composition of the galactic cosmic rays. Annual Review of Nuclear and Particle Science 33, 323–382.

Stadermann, F.J., Walker, R.M., Zinner, E., 1999. Sub-Micron Isotopic Measurements with the CAMECA NanoSIMS. Lunar and Planetary Science Conference 30, abstract #1407.

Steele, R.C.J., Coath, C.D., Regelous, M., Russell, S., Elliott, T., 2012. Neutron-poor nickel isotope anomalies in meteorites. The Astrophysical Journal 758, 59.

Steele, R.C.J., Elliott, T., Coath, C.D., Regelous, M., 2011. Confirmation of mass-independent Ni isotopic variability in iron meteorites. Geochemica et Cosmochimica Acta 75, 7906–7925.

Steinberg, E.P., Winsberg, L., 1974. Recoil properties of ^{22}Na and ^{24}Na produced in the interaction of ^{27}Al with 3- to 300-GeV protons. Phys. Rev. C 10, 1925–1927.

Stephan, T., Trappitsch, R., Davis, A.M., Pellin, M.J., Rost, D., Savina, M.R., Yokochi, R., Liu, N., 2016. CHILI – the Chicago Instrument for Laser Ionization – a new tool for isotope measurements in cosmochemistry. International Journal of Mass Spectrometry, in press.

Stephan, T., Zehnpfenning, J., Benninghoven, A., 1994. Correction of dead time effects in time-of-flight mass spectrometry. Journal of Vacuum Science & Technology A: Vacuum, Surfaces, and Films 12, 405–410.

Stone, E.C., Cummings, A.C., McDonald, F.B., Heikkila, B.C., Lal, N., Webber, W.R., 2013. Voyager 1 observes low-energy galactic cosmic rays in a region depleted of heliospheric ions. Science 341, 150–153.

Straniero, O., Chieffi, A., Limongi, M., Busso, M., Gallino, R., Arlandini, C., 1997. Evolution and nucleosynthesis in low-mass asymptotic giant branch stars. I. formation of population I carbon stars. The Astrophysical Journal 478, 332–339.

Straniero, O., Cristallo, S., Gallino, R., 2009. The ^{13}c pocket in low-mass AGB stars. Publications of the Astronomical Society of Australia 26, 133–138.

Straniero, O., Domínguez, I., Cristallo, S., Gallino, R., 2003. Low-mass AGB stellar models for 0.003 <= Z <= 0.02: Basic formulae for nucleosynthesis calculations. Publications of the Astronomical Society of Australia 20, 389–392.

Straniero, O., Gallino, R., Cristallo, S., 2006. s process in low-mass asymptotic giant branch stars. Nuclear Physics A 777, 311–339.

Straniero, O., Gallino, R., Cristallo, S., 2008. s process in low-mass asymptotic giant branch stars. Nuclear Physics A 777, 311–339.

Straniero, O., Limongi, M., Chieffi, A., Dominguez, I., Busso, M., Gallino, R., 2000. Thermally pulsing AGB models of intermediate mass stars. Memorie della Società Astronomia Italiana 71, 719–727.

Tang, M., Anders, E., 1988a. Isotopic anomalies of Ne, Xe, and C in meteorites. III. local and exotic noble gas components and their interrelations. Geochimica et Cosmochimica Acta 52, 1245–1254.

Tang, M., Anders, E., 1988b. Interstellar silicon carbide - how much older than the solar system? The Astrophysical Journal Letters 335, L31–L34.

Timmes, F.X., Clayton, D.D., 1996. Galactic evolution of silicon isotopes: Application to presolar SiC grains from meteorites. The Astrophysical Journal 472, 723–741.

Trappitsch, R., Ciesla, F.J., 2015. Solar cosmic-ray interaction with protoplanetary disks: Production of short-lived radionuclides and amorphization of crystalline material. The Astrophysical Journal 805, 5 (11pp).

Trappitsch, R., Davis, A.M., 2013. Retention model for radiogenic lead isotopes in presolar grains. Lunar and Planetary Science Conference 44, abstract #2666.

Trappitsch, R., Leya, I., 2013. Cosmogenic production rates and recoil loss effects in micrometeorites and interplanetary dust particles. Meteoritics & Planetary Science 48, 195–210.

Trappitsch, R., Leya, I., 2016. Production and recoil loss of cosmogenic nuclides in presolar grains. The Astrophysical Journal 823, 12 (11pp).

Trappitsch, R., Nittler, L.R., Savina, M.R., Davis, A.M., 2013. Modeling heterogeneous galactic chemical evolution for presolar grain comparison. Meteoritics & Planetary Science Supplement 76, A5351.

Trappitsch, R., Savina, M.R., Willingham, D.G., Liu, N., Pellin, M.J., Dauphas, N., Davis, A.M., 2012. Iron isotopic abundances in presolar grains. Lunar and Planetary Science Conference 43, abstract #2497.

Wieler, R., 2002. Cosmic-ray-produced noble gases in meteorites, in: Porcelli, D., Ballentine, C.J., Wieler, R. (Eds.), Noble Gases in Geochemistry and Cosmochemistry. The MIneralogical Society of America, Washington, DC. volume 47 of *Reviews in Mineralogy & Geochemistry*. chapter 5, pp. 123–170.

Woosley, S.E., Heger, A., 2007. Nucleosynthesis and remnants in massive stars of solar metallicity. Physics Reports 442, 269–283.

Woosley, S.E., Weaver, T.A., 1995. The evolution and explosion of massive stars. II. explosive hydrodynamics and nucleosynthesis. The Astrophysical Journal Supplement Series 101, 181–235.

Worden, E.F., Comaskey, B., Densberger, J., Christensen, J., McAfee, T.M., Paisner, T.A., Conway, J.G., 1984. The ionization potential of neutral iron, Fe I, by multistep laser spectroscopy. Journal of the Optical Society of America B 1, 314–316.

Wunderlich, R.K., Wasserburg, G.J., Hutcheon, I.D., Blake, G.A., 1992. Systematics of the odd-even effect in the resonance ionization of Os and Ti. Institute of Physics Conference Series 128, 127–130.

Ziegler, J.F., 2004. SRIM-2003. Nuclear Instruments and Methods in Physics Research B 219-220, 1027–1036.

Zinner, E., 2014. 1.4 - presolar grains, in: Turekian, K.K., Holland, H.D. (Eds.), Treatise on Geochemistry (Second Edition). Oxford, UK: Elsevier, Oxford, pp. 181–213.

Zinner, E., Nittler, L.R., Gallino, R., Karakas, A.I., Lugaro, M., Straniero, O., Lattanzio, J.C., 2006. Silicon and carbon isotopic ratios in AGB stars: SiC grain data, models, and the galactic evolution of the Si isotopes. The Astrophysical Journal 650, 350–373.